UNCLASSIFIED

SECURITY CLASSIFICATION OF THIS PAGE (When Data Entered)

REPORT DOCUMENTATION PAGE		READ INSTRUCTIONS BEFORE COMPLETING FORM
1. REPORT NUMBER	2. GOVT ACCESSION NO.	3. RECIPIENT'S CATALOG NUMBER
4. TITLE (and Subtitle) FIELD STUDIES OF RUN-UP GENERATED BY WIND WAVES ON DISSIPATIVE BEACHES		5. TYPE OF REPORT & PERIOD COVERED IR&D Final Technical Report February 1980 - March 1984 6. PERFORMING ORG. REPORT NUMBER Final Technical Report
7. AUTHOR(s) Christopher T. Carlson		8. CONTRACT OR GRANT NUMBER(s) SRI IR&D 634D32-BUA
9. PERFORMING ORGANIZATION NAME AND ADDRESS SRI International 333 Ravenswood Avenue Menlo Park, California 94025		10. PROGRAM ELEMENT, PROJECT, TASK AREA & WORK UNIT NUMBERS SRI Project 634D32-BUA
11. CONTROLLING OFFICE NAME AND ADDRESS SRI International (Remote Measurements Lab.) 333 Ravenswood Avenue Menlo Park, California 94025		12. REPORT DATE March 1984 13. NUMBER OF PAGES 194
14. MONITORING AGENCY NAME & ADDRESS (if diff. from Controlling Office)		15. SECURITY CLASS. (of this report) UNCLASSIFIED 15a. DECLASSIFICATION/DOWNGRADING SCHEDULE

16. DISTRIBUTION STATEMENT (of this Report)

Approved for public release; distribution unlimited.

17. DISTRIBUTION STATEMENT (of the abstract entered in Block 20, if different from Report)

18. SUPPLEMENTARY NOTES

19. KEY WORDS (Continue on reverse side if necessary and identify by block number)

Run-up	Coastal erosion	Beaches
Swash	Beach swash	Nearshore processes
Wave run-up	Photogrammetry	Spectral analysis
Run-up spectrum	Swash spectrum	Statistical hypothesis testing

20. ABSTRACT (Continue on reverse side if necessary and identify by block number)

Field measurements of incident waves and the resulting run-up made at two different natural sand beaches along San Francisco Bay show low-frequency energy in the run-up not observed in the corresponding incident-wave spectra. The experiments were conducted in December 1977 at Alameda Beach and in May 1982 at Coyote Point Beach. Both experiments were designed to measure the run-up on dissipative beaches exposed only to high-frequency, narrow-band wind waves at the exclusion of lower frequency swell. Criteria for field-site

DD FORM 1 JAN 73 1473

EDITION OF 1 NOV 65 IS OBSOLETE

UNCLASSIFIED

SECURITY CLASSIFICATION OF THIS PAGE (When Data Entered)

19. KEY WORDS (Continued)

20 ABSTRACT (Continued)

selection included a single breaker zone located near the shoreline with incident wind waves that broke by plunging, thereby minimizing reflection and forming a low-energy dissipative beach system. Elimination of the long-wave components in the incident wave field would suppress reflection at the shoreline, minimizing external nonlinear modulation of the run-up by edge waves and standing waves.

Amplitude time series measurements of offshore incident waves and the run-up on the beach face were made simultaneously at multiple locations on the beach using 16-mm photography. The photographs were subsequently digitized and analyzed using oblique photogrammetric methods. The run-up spectra derived from the field-measured time series show some energy at the incident-wave peak frequency, with the predominant run-up spectral energy concentrated in frequency bands below the incident-wave peak frequency. Observations of the swash time series recorded at both beaches indicate that the low-frequency run-up is generated on the beach face by the resonant interaction of the run-up and backwash in the swash cycle.

Coherence analyses indicate that the offshore incident waves and run-up on the beach are not linearly correlated. Correlation analyses conducted on the run-up at alongshore distances up to 3.5 m indicate that the run-up is coherent in the alongshore direction up to this distance.

The slopes of the log-log run-up spectra computed over the frequency band of the breaking incident waves are all approximately -3. This consistency in slope supports the hypothesized existence of an equilibrium form for the run-up spectrum.

Kolmogorov-Smirnov and chi-square statistical hypothesis tests were conducted comparing the empirical run-up cumulative distribution functions with normal and Rayleigh distribution functions. The run-up measured at Coyote Point was not significantly different from a standard (0,1) normal distribution at the 95% confidence interval.

IR&D Report

March 1984

FIELD STUDIES OF RUN-UP GENERATED BY WIND WAVES ON DISSIPATIVE BEACHES

By: CHRISTOPHER T. CARLSON
Remote Measurements Laboratory

Prepared under SRI IR&D Project 634D32-BUA

SRI International
333 Ravenswood Avenue
Menlo Park, California 94025
(415) 326-6200
Cable: SRI INTL MPK
TWX: 910-373-2046

AN (1) AD-A148 793
FG (2) 080300
CI (3) (U)
CA (5) SRI INTERNATIONAL MENLO PARK CA
TI (6) Field Studies of Run-Up Generated by Wind Waves on Dissipative Beaches.
DN (9) Final technical rept. Feb 80-Mar 84,
AU (10) Carlson,C. T.
RD (11) Mar 1984
PG (12) 191p
RC (20) Unclassified report
DE (23) *Ocean waves, Statistical analysis, San Francisco Bay
DC (24) (U)
ID (25) *Wave runup
IC (26) (U)
AB (27) Field measurements of incident waves and the resulting run-up made at two different natural sand beaches along San Francisco Bay show low-frequency energy in the run-up not observed in the corresponding incident-wave spectra. The experiments were conducted in December 1977 at Alameda Beach and in May 1982 at Coyote Point Beach. Both experiments were designed to measure the run-up on dissipative beaches exposed only to high-frequency, narrow-band wind waves at the exclusion of lower frequency swell. Criteria for field-site selection included a single breaker zone located near the shoreline with incident wind waves that broke by plunging, thereby minimizing reflection and forming a low-energy dissipative beach system. Elimination of the long-wave components in the incident wave field would suppress reflection at the shoreline, minimizing external nonlinear modulation of the run-up by edge waves and standing waves. Amplitude time series measurements of offshore incident waves and the run-up on the beach face were made simultaneously at multiple locations on the beach using 16-mm photography. Coherence analyses indicate that the offshore incident waves and run-up on the beach are not linearly correlated. Correlation analyses conducted on the run-up at alongshore distances up to 3.5 m indicate that the run-up is coherent in the alongshore direction up to this distance.
AC (28) (U)
DL (33) 01
SE (34) F
CC (35) 410281

SRI International

IR&D Report *March 1984*

FIELD STUDIES OF RUN-UP GENERATED BY WIND WAVES ON DISSIPATIVE BEACHES

By: CHRISTOPHER T. CARLSON
Remote Measurements Laboratory

Prepared under SRI IR&D Project 634D32-BUA

Approved by:

LAWRENCE E. SWEENEY, JR., *Director*
Remote Measurements Laboratory

DAVID A. JOHNSON, *Vice President*
System Technology Division

SRI INTERNATIONAL, 333 Ravenswood Avenue, Menlo Park, California 94025
(415) 326-6200, Cable: SRI INTL MPK, TWX: 910-373-2046

SRI International®

CONTENTS

CONTENTS (Continued)

ILLUSTRATIONS

ILLUSTRATIONS (Continued)

ILLUSTRATIONS (Concluded)

TABLES

ACKNOWLEDGMENTS

Many individuals helped to make this study possible. I would like to acknowledge Dr. Joseph W. Maresca, Jr. of SRI and Dr. Erwin Seibel of San Francisco State University for their participation in the field experiments and for their many helpful discussions concerning data analysis and interpretation.

A special thanks to Professor Robert L. Wiegel of the University of California, Berkeley (UCB) for his advice during this project. In addition, the UCB Department of Hydraulic and Coastal Engineering provided generous access to the wave basin it operates.

Field work requires many hands. I would also like to extend my thanks to Mrs. Monique L. Seibel and Mrs. Deborah D. Carlson for enduring the cold winds on San Francisco Bay and helping during the field experiments.

Thanks to my colleagues at SRI for their assistance in designing several of the electronic components used in this research. Messrs. Philip C. Evans and Fred J. Heinzmann were most helpful with the RC filter design, and Mr. Ralph E. Wanner built the electric clock used in the field experiments. Mr. James M. Lomasney procured two very scarce Amphenol connectors for the laboratory electronics, saving much time.

I am most appreciative of the help received from Dr. J. Raul Martinez, Mr. Mark A. Orwoll, and Dr. David G. Falconer of SRI with the statistical analyses of the data.

Thanks to Mrs. Lora F. Laine for typing the manuscript, Ms. Bronwyn G. Brady for editing it, and Mr. Russell H. Griswold, Ms. Laura K. Kuge, and Mr. Brian K. McLean for the final illustrations.

I INTRODUCTION

Beach erosion and damage to coastal structures by waves is a problem of concern to owners, developers, and users of the coastal shorelines. Direct attack on the coastal bluffline by incident waves and wave run-up on the beach can produce severe bluffline recession, frequently resulting in property damage and significant changes in the nearshore and beach topography. Design of coastal structures and offshore artificial islands and effective planning for coastal utilization require both long- and short-term prediction of incident-wave conditions and potential erosion.

The amount of coastal erosion or damage to a coastal structure by waves is directly related to the percentage of the incident-wave energy actually reaching the beach, bluff toe, or structure foundation. When the waves do not directly strike the coastal bluff or structure foundation, it is the wave energy transferred to the run-up that causes the damage. The frequency distribution of that energy can also have a profound effect on the dynamics of the interaction between the incident wave or run-up and the beach or coastal structure, particularly if a resonance condition develops.

The frequency band containing the dominant run-up spectral energy is generally not the same as the frequency band of the predominant incident-wave energy. For this reason, offshore wave statistics may not provide good estimates of the wave energy frequency distribution expected at the shoreline. A shift in the run-up spectral energy to frequencies lower than the predominant incident-wave frequencies has been observed for the run-up generated by a broadband incident-wave field. Field studies of wave run-up reported in the open literature are very limited, and most have been conducted on the open coast where incident-wave fields are usually swell dominated. The incident-wave/beach slope combinations have generally produced reflective systems, and the

low-frequency run-up observed or measured during the experiments has been attributed to modulation of the run-up by standing waves or edge waves present near the shoreline. No measurements have been reported for the run-up generated on a dissipative beach by narrow-band wind waves only. Low-frequency swell and surf-beat components in the run-up spectrum can often obscure other low-frequency contributions to the run-up spectral energy that are developed by the higher frequency wind waves in the incident-wave field. Edge wave and standing wave effects are strongest on reflective beach systems and are generally absent on dissipative beaches exposed to narrow-band, incident wind waves that break by plunging. The so-called red-shift in the run-up spectrum, however, has been observed on both reflective and dissipative beach systems exposed to broadband incident-wave fields composed of both swell and locally generated wind waves.

Field and laboratory studies have suggested that low-frequency run-up spectral energy may also be generated on the beach face by the resonant interaction of the run-up and backwash in the swash cycle (see Section VI). This swash resonance mechanism can produce a red-shift in the frequency distribution of the run-up spectral energy measured on a dissipative beach, as can external modulation of the run-up by standing waves and edge waves on a reflective beach.

The fundamental objective in much coastal engineering research has been to understand the behavior of water waves in the vicinity of the shoreline. Swash dynamics is perhaps one of the least well-understood phases of coastal wave mechanics. In dynamic equilibrium with the waves, the beach provides a porous interface between two dissimilar phases, thus complicating efforts to model or describe swash dynamics theoretically. A more basic and possibly more enlightening approach to the study of swash behavior is to make in situ measurements of run-up and backwash on natural beaches.

A. Objective and Approach

The objective of this study is to measure low-frequency run-up generated on the beach face by the resonant interaction between the

run-up and backwash in the swash cycle, in the absence of external modulation of the run-up by standing waves or edge waves. The experiments described herein were designed to measure run-up on dissipative beaches exposed only to high-frequency, narrow-band wind waves that broke near the shoreline by plunging. These conditions generally minimize or eliminate contamination of the incident-wave field by standing waves, edge waves, or very-low-frequency surf-beat generated by the swell component of an incident-wave field.

A simple rectilinear model was developed that simulated the swash as a series of sliding layers on the beach face (Appendix C). This model showed that low-frequency run-up could be generated solely by the interaction of the run-up and the backwash on the beach face, without low-frequency forcing by the incident-wave field. Field and laboratory experiments were required to demonstrate this phenomenon for real incident-wave/run-up systems.

Next, an attempt was made to generate low-frequency run-up for monochromatic waves under laboratory conditions. Simultaneous time series measurements of incident waves and the resulting swash on the beach were made in a laboratory wave basin for controlled monochromatic incident-wave conditions. The incident-wave time series were measured and recorded electronically, and the swash time series were recorded photographically. Several combinations of incident-wave steepness and beach slope were analyzed, as described in Appendix A.

The effects of a narrow-band spectrum of incident wind waves on the swash resonance phenomenon were subsequently examined in situ. Experiments in which incident waves and resulting run-up were measured simultaneously were conducted at two different natural beaches on San Francisco Bay. The incident waves were measured at staffs in the surf zone, and the run-up on the beach face was measured along transects normal to the shoreline using 16-mm photography. The data were analyzed to produce calibrated time series and spectra of the incident waves and run-up. Coherence analyses and statistical hypothesis tests were conducted to establish the statistical characteristics of the data and to evaluate

the degree of correlation between the measurements made offshore and on the beach.

B. Concepts and Terminology

It is useful here to introduce several concepts and terms that will appear throughout the text. Figure 1 shows a typical beach profile similar to the Coyote Point and Alameda Beach field sites used in this study. The mean still water level (MSWL) is the elevation that the sea surface would assume if no waves were present. This water elevation is affected by fluctuations due to tides, wind set-up, and wave set-up (Appendix B). These fluctuations typically have periods in excess of 30 to 60 s and do not adversely affect the run-up or incident-wave measurements in these field experiments.

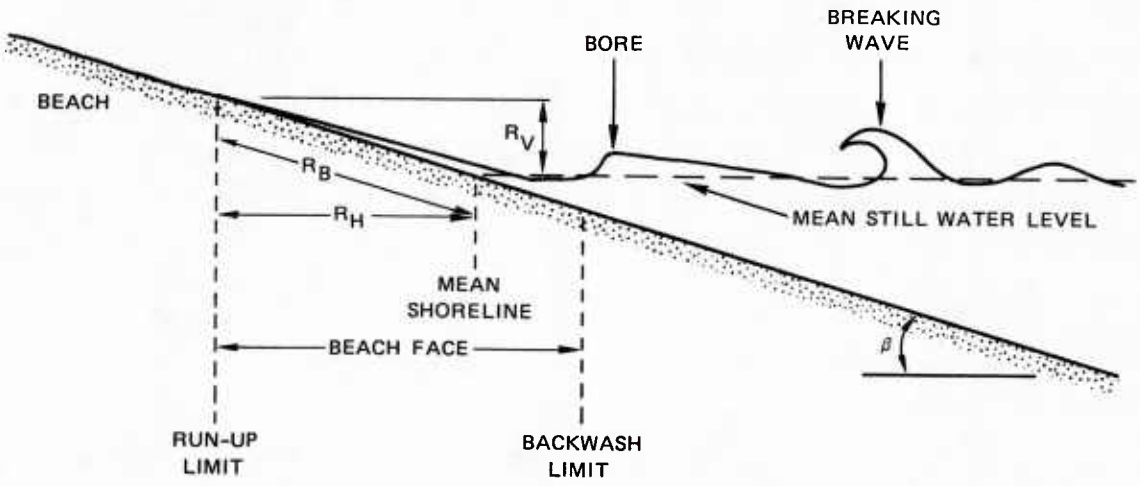

FIGURE 1 BEACH CROSS SECTION SHOWING THE COMPONENTS OF RUN-UP MEASURED VERTICALLY AND IN THE PLANE OF THE BEACH FACE

The swash zone is defined by the run-up and backwash limits. The shoreward limit of the swash zone is determined by the maximum excursion

of the run-up, and the seaward limit is controlled by the maximum backwash. The beach face, coincident with the swash zone, experiences periodic inundation that is controlled by the run-up and backwash in the swash cycle. The position of the swash zone on the beach fluctuates with the MSWL position.

The run-up on the beach face can be measured either as the vertical superelevation of the water surface above the MSWL intersection with the beach face, R_V in Figure 1, or in the plane parallel with the beach face, R_B in Figure 1. R_B was the component of run-up measured in the results reported here, but it can easily be converted to R_V by multiplying by the sine of the beach slope angle. Linear beach slopes were measured at the Alameda and Coyote Point beaches, and the conversion of R_B to R_V would only affect the absolute magnitude of the run-up amplitude time series, not the frequency distribution of the run-up spectral energy. Negative values of R_B indicate backwash measured relative to the position of the mean shoreline.

Since this study focuses on swash resonance generated on the beach face by the interaction of the run-up and backwash, it was necessary to avoid reflective beach conditions in which resultant nonlinear perturbation of the incident-wave field might affect the frequency distribution of the run-up on the beach face. For this reason, both the field and laboratory measurements were conducted for dissipative beach conditions. Beach reflectivity and inshore resonance may be characterized by a reflectively or surf scaling parameter, ε :

$$\varepsilon = \frac{a_i \omega^2}{g \tan^2 \beta}$$

where a_i is the incident-wave amplitude, ω is the radian incident-wave frequency, g is the gravitational acceleration, and β is the beach slope. A short discussion of the parameter ε and the characterization of beach resonance in terms of ε is given in Appendix D.

Dissipative beach conditions are characterized by values of ε greater than about 2.5, and highly dissipative beaches yield ε values greater than 33. The experiments described here are focused on swash activity in the moderately dissipative regime, which is identified by a relatively narrow surf zone, plunging breakers, and strong run-up. Ideal beach reflectivity conditions for these field and laboratory experiments would yield values of ε between 5 and 20. The ε values measured for the field and laboratory data were all within this range.

C. Summary of Results

Incident-wave and run-up time series data were recorded at Alameda and Coyote Point beaches on San Francisco Bay. The incident-wave conditions that prevailed during both experiments produced the desired plunging breakers and dissipative beach conditions, thereby suppressing standing wave and edge wave activity. Short-crested waves were observed during the Coyote Point experiment.

Low-frequency energy was observed in the run-up measured at both locations. Little or no energy was observed in the run-up spectra at frequencies corresponding to the predominant incident-wave frequencies. No low-frequency energy was observed in the incident-wave field. Coherence analyses between offshore incident-wave time series and the swash time series measurements show that no statistically significant linear correlation existed between these respective measurements at either beach during the experiments reported here. Coherence analyses were conducted for the Coyote Point run-up data at distances up to 3.5 m in the alongshore direction. The computed squared coherence and phase indicate that the run-up is correlated at a statistically significant level at distances up to the 3.5-m limit analyzed here.

The spectral slopes were computed over the equilibrium frequency band for the run-up and incident-wave spectra measured at both beaches. All of the run-up spectra displayed a -3 spectral slope on the log-log plots. The incident waves were measured at several locations offshore. The incident-wave spectra showed slopes ranging from -3 to -2. The -3

slopes were computed for the data recorded furthest offshore, seaward of the break point, and the -2 slopes were measured shoreward of the breakpoint.

The cumulative distribution functions (CDFs) were computed for the incident-wave and run-up field data recorded at both beaches. Kolmogorov-Smirnov and chi-square statistical hypothesis tests were used to compare the CDFs computed from the measured empirical data with standard normal and Rayleigh distributions proposed by others as models for describing wave and run-up amplitude distributions. Based on the statistical hypothesis tests, the hypothesis that the Coyote Point run-up was Rayleigh-distributed was rejected at the 95% confidence interval. The hypothesis that the Coyote Point run-up was normally-distributed could not be rejected at the 95% confidence interval. Thus, the tests indicate that a normal distribution provided an acceptable fit to the Coyote Point run-up data and that a Rayleigh distribution did not. Using the same hypothesis tests, the hypotheses that the CDFs for the Coyote Point waves were either normal or Rayleigh were both rejected at the 95% confidence interval. Qualitatively, however, the normal distribution provided a reasonable fit to the incident-wave data.

The same statistical tests were applied to the Alameda incident-wave and run-up time series data. These tests indicated quantitatively that the run-up data were statistically different from both the normal and the Rayleigh distributions, but the incident waves were not statistically different from the normal distribution at the 95% confidence interval.

Three laboratory experiments were conducted in the 1.8- by 4-m (6- by 13-ft) wave basin located at the University of California, Berkeley (UCB) Hydraulic and Coastal Engineering Laboratory. Two of these experiments showed the peak frequency in the run-up spectrum to be the same as the spectral peak frequency of the monochromatic incident waves. One of these experiments, however, showed the predominant run-up spectral energy to be located at the second subharmonic of the incident-wave frequency.

A rectilinear motion model was also used to simulate the frequency distribution of run-up generated by incident waves with characteristics similar to those observed in the laboratory and in the field, as well as for incident-wave conditions derived from data presented by others in the open literature. The run-up model in its current form works best for multiple incident-wave forcing frequencies. When a number of incident-wave frequencies are input to simulate a multi-component, broad-band incident-wave field, the run-up simulated by the model shows low-frequency energy similar to that observed in the measured data.

II PREVIOUS RUN-UP INVESTIGATIONS

Historically, programs for research of wave run-up and swash dynamics have shared the common objective of establishing a proven method for predicting the maximum shoreward excursion of water during the run-up phase of the swash cycle, given - a priori - the incident-wave conditions and the beach slope. Based on specific goals and approaches, run-up research may be grouped into three complementary categories: theoretical, engineering, and field studies. The results of rigorous mathematical analyses may be compared to engineering model studies wherein specific parameters can be manipulated individually to access their relative importance in controlling run-up. Ultimately, however, the results of both theoretical and engineering run-up research and modeling must be tested in comparison with real data obtained from field experiments.

A. Theoretical Studies

Early research concentrated on theoretical solutions of the linear long-wave equations. During the 1940s, the Courant Group formulated an analytical solution to the problem of waves on a sloping beach, using classical long-wave theory as summarized by Meyer and Taylor (1972). Stoker (1947) presented analysis that described breaker formation and bore motion on a sloping beach. Friedrichs (1948) presented an exact solution to the long-wave equations based on their limit as the beach slope approached zero. Friedrichs' standing-wave solution established a connection between shallow-water and deep-water behavior of the same small-amplitude wave train. The small-amplitude linearization of the classical equations, and the subsequent standing-wave solution, contained a mathematical singularity at the shoreline that prevented a description of the ensuing run-up. Thus, while the classical theory with the appropriate small-amplitude linearization can be used successfully to relate wave motion both near and far from shore, it does not furnish a description of the actual wave run-up or motion of the shoreline. Due to the

theoretical restrictions of small incident-wave steepness and perfect reflection at the shoreline, the linearized solutions to the classical long-wave equations cannot be used to predict run-up on a beach slope.

Analytical prediction of wave run-up required a nonlinear model in which the shoreline was allowed to move up and down the beach face. Carrier and Greenspan (1958) used the nonlinear shallow-water equations to formulate an exact solution describing water motion at the shoreline. Although their exact nonlinear result provided an improvement in linear run-up prediction, it was dependent on perfect reflections of the surging waves from the beach, an assumption with limited applicability on a real natural beach.

These earliest analytical solutions to wave behavior at the shoreline assumed small-amplitude, non-breaking surge on a slope. Although of interest on a theoretical plane, these solutions were of little value for beaches fronted by breaking waves and approaching bores. Keller et al. (1960), Ho and Meyer (1962), Ho et al. (1963), Shen and Meyer (1963), and Freeman and LeMehaute (1964) described methods for using a nonlinear model to represent the motion of a fully developed bore moving into water of decreasing depth. The models treat the shoreward-moving bore as a shock wave and predict the subsequent transformation of the bore into a rarefaction wave surging over the dry bed during the run-up phase of the swash cycle. The models of Ho et al. (1963) and Hibberd and Peregrine (1979) also describe the landward-facing bore forming during the backwash phase of the swash cycle.

Miller (1968) conducted laboratory experiments to verify some of the theoretical predictions of run-up produced by moving bores. His observations indicated that the long-wave solutions did not accurately predict the ratio of run-up height to bore strength and that only partial collapse of the bore front occurs as the bore approaches the shoreline. These inconsistencies were attributed to viscous effects not properly accounted for in the various earlier models. LeMehaute (1962) and Freeman and LeMehaute (1964) utilized a bed friction coefficient in their model, which produced better agreement between the model-derived run-up and the empirical observations.

The nonlinear beach equations used with the bore relations described in the aforementioned literature do a reasonable job of modeling the transformation of a single wave into run-up and backwash in a qualitative sense. It is necessary, however, to model multiple waves incident at the shoreline for a realistic simulation of run-up. The net importance of viscous friction in the models and the differences in performance between standing and progressive wave theories for beach run-up mechanics remain to be resolved.

B. Engineering Studies

Design of coastal structures has always required accurate estimation of expected wave run-up amplitudes. The formal theoretical descriptions of wave run-up did not provide the kind of quantitative engineering estimates of run-up behavior required for design purposes. Most early empirical engineering studies of swash on slopes were designed to establish for the first time the relationships between incident-wave parameters (including frequency, height, angle of wave incidence, and location of the wave break point) and the characteristics of the structure (including its slope, porosity, and roughness). Granthem (1953), Saville (1958), Hunt (1959), Savage (1959), and Hudson (1959) each reported results on these aspects of the incident-wave/run-up relationship.

Most of these early engineering studies utilized monochromatic incident-wave trains during the experiments. More recently, engineering analyses of wave run-up have focused on the effects of irregular waves on run-up amplitudes. Several attempts have been made to model run-up as a stochastic process. Saville (1962) used standard wave run-up curves and Bretschneider's wave steepness distribution to develop the first run-up frequency distribution curve. Carstens et al. (1966) used a hydraulically driven wave paddle to generate irregular waves for stability studies of rubble mound breakwaters and analyses of the associated run-up. Van Oorschot and d'Angremond (1968) compared the run-up of irregular waves to run-up derived from experiments with wind-generated and monochromatic waves. They also show run-up distribution curves derived from

their data. Webber and Bullock (1968) showed incident-wave and run-up distributions for measurements made in a wind wave flume equipped with an impermeable beach. They compared their empirical results with theoretical relationships and concluded that run-up height distributions cannot be predicted on the basis of the run-up for each individual wave but are dependent on the run-up due to the previous waves. They also observe in accordance with van Oorschot and d'Angremond (1968) that scale effects modify the statistical properties of the laboratory wind waves and the resulting run-up and that prototype scale investigations are clearly required to assess the effect of these scale differences.

Battjes (1971, 1974) and Ahrens (1977) considered a stochastic formulation for development of a run-up prediction technique. Battjes invoked the hypothesis of equivalency described by Saville (1962) and van Oorschot and d'Angremond (1968) and derived an expression for the run-up distribution of irregular waves based on Hunt's formula (1959). Ahrens (1977) assumed that run-up is Rayleigh-distributed and developed a run-up distribution curve to be used for run-up prediction.

Sutherland et al. (1976) reported laboratory measurements of run-up generated by irregular incident waves in the presence of an offshore bar. Their results show a frequency down-shift between the spectral peak frequency of the run-up relative to the peak frequency of the incident waves. They computed spectral slopes of -5 and -4 for the empirical incident-wave and run-up data, respectively.

These various engineering approaches to prediction of wave run-up amplitudes span the spectrum of parametric relationships between incident-wave characteristics and observed run-up. The greatest insight provided by the engineering studies came from observations of wave steepness and relative water depth relationships to run-up heights. Many of the results conflict, however, and while the basic run-up/incident-wave relationships have been identified, the physics actually controlling the run-up have yet to be modeled fully. Scale effects have adversely affected some of the laboratory empirical data, and the variability in the overall run-up data set has hampered development of a final closed-form run-up model.

C. Field Studies

Although numerous field studies of surf zone phenomena have been conducted, the majority were focused on wave transformation and breaking; few have dealt explicitly with swash dynamics. In recent years, attention has shifted shoreward to the immediate vicinity of the shoreline. The full implications of the interrelationships and feedback mechanisms active between the incident-wave field and the beach are just now being realized.

Emery and Gale (1951) reported some of the first quantitative visual and photographic measurements of incident waves and run-up made simultaneously. They observed that the swash period was greater than the incident-wave period on several natural beaches. They suggested that the difference between the periods was due to the interaction between the run-up and the backwash in the swash cycle.

Edge wave studies have provided much insight into nearshore water circulation and velocity fields. Bowen (1969) and Bowen and Inman (1969, 1971) speculated that edge waves along a beach can modulate the incident-wave and run-up energy, forming cuspate features along the shoreline. They also correlated nearshore circulation cells and rip current spacing with the spacing of edge wave antinodes.

Huntley and Bowen (1975a) suggested that the natural run-up period of a beach is dependent upon surf zone width and breaker height and that subharmonic resonance in the run-up should exist only for certain combinations of incident-wave amplitudes and frequencies. Huntley and Bowen (1975b) observed the regularity in the run-up pattern and nearshore features present on many natural beaches exposed to long, small-amplitude waves and suggested that although numerous edge wave modes are theoretically possible, a single mode is generally present at a given time. They relate visual field observations of alongshore modulation of the run-up amplitude on the beach face when edge waves were present but no shoreline beach cusps had formed.

Observations of wave run-up were often by-products of edge wave field studies, and relatively few researchers made high-resolution run-up measurements specifically. Waddell (1973), however, measured the incident waves at one offshore location, the swash depth at four locations on the beach face, and the ground water fluctuations at six onshore locations. During his investigations, the beach was exposed to incident swell waves, and low-frequency energy observed in the run-up spectra was attributed to standing waves that formed at the shoreline. Suhayda (1974) made simultaneous measurements of nearshore incident waves at one location and run-up along a single transect crossing the beach face. His analyses dealt with low-steepness swell shoaling on a smooth, steep, highly reflective beach, which combined to generate strong standing waves. The dominant standing-wave frequency was observed in the run-up spectrum. Sonu et al. (1974) measured the run-up and swash orbital velocities on a gently sloping beach exposed to an incident-wave field consisting of both swell and locally-generated wind waves. The run-up amplitude spectra measured at four locations showed a shoreward down-shifting of the spectral peak frequency due to a low-pass filtering effect of the beach on the incident waves and resulting swash (see Section VI).

In 1977, Huntley et al. reported a series of field run-up measurements made on four different natural beaches exposed to incident-wave fields consisting of swell combined with wind waves. Based on the similarity of the measured run-up spectra, they proposed the existence of an equilibrium region in the run-up spectrum with a "universal" spectral form. They suggested that an f^{-4} frequency dependence could be defined over a limited frequency band covering the saturated region of the run-up spectrum. Low-frequency run-up spectral energy observed in their swash spectra was attributed to standing wave and edge wave modulation of the run-up.

Wright et al. (1977, 1979) summarized several field measurements of surf and inshore current spectra, inshore circulation patterns, and depositional morphology made at several contrasting beach localities

for different incident-wave energy conditions. Using these data, they proposed categorization of beaches by type, depending on hydrodynamic and morphologic characteristics.

Most recently, Bradshaw (1982) presented results of field investigations designed to study the behavior of bores in the inner surf zone of natural beaches. Bradshaw used a simple model describing bore motion to describe the merger of successive shoreward-moving bores observed in the field. His simulation stops at the shoreline. Photographic measurements of swash show a low-frequency dominance on the flat beaches described in his report.

Guza and Thornton (1982) reported run-up measurements made at the same gently sloping natural beach during two different months for a variety of different incident-wave conditions. Their run-up amplitude spectra showed an f^{-3} frequency dependence over the wind-wave frequency band, and the observed wave-height independence suggests energy saturation at these frequencies. During their experiments, the incident waves comprised a mixture of spilling and plunging-spilling breakers with both swell and wind-wave frequencies represented. Significant energy levels were observed in the run-up spectra at surf-beat frequencies, and the energy in these bands increased approximately linearly with increasing incident-wave energy. Run-up spectral energy appears to be limited by saturation at wind-wave frequencies and thus is independent of offshore wave conditions. The run-up variance continues to increase at surf-beat frequencies, however, as the incident-wave variance increases.

III FIELD EXPERIMENTS

Field experiments were conducted at two different natural sand beaches along San Francisco Bay to measure the incident-wave field and the resulting run-up simultaneously. On 14 December 1977, measurements were made at the R.W. Crown Memorial State Beach on the western shore of Alameda Island; similar measurements were subsequently made along western San Francisco Bay on 14 May 1982 at Coyote Point Beach (Figure 2). Two separate field sites were chosen to provide independent data sets for different beach slopes exposed to different incident wind-wave fields. Both beaches were selected based on their exposure to only narrow-band wind waves that were normally incident to the shoreline and that broke by plunging. The beaches and incident waves formed moderately dissipative systems.

A. Alameda Beach

The Alameda Beach was composed of fine- to medium-grained silica sand with minimal heavy mineral content. The clay component increased offshore, forming a firm and stable nearshore bottom. The beach is openly exposed to westerly and southwesterly winds, as shown in Figure 2. Four trips were made to Alameda Beach, and the incident-wave conditions permitted data collection on two of these days. One data set was lost, however, due to photographic problems, leaving only the 14 December data.

A hand-held anemometer-compass was used to measure the wind speed and direction during the experiment. The desired sea state was created early in the afternoon as wind speeds increased from 3 m/s to over 5 m/s (Table 1). A single breaker zone was located approximately 3 m from the shoreline, and all waves broke by plunging. The 14 December experiment described here was conducted during the peak of the afternoon high tide, which occurred at about 1420 PDT.

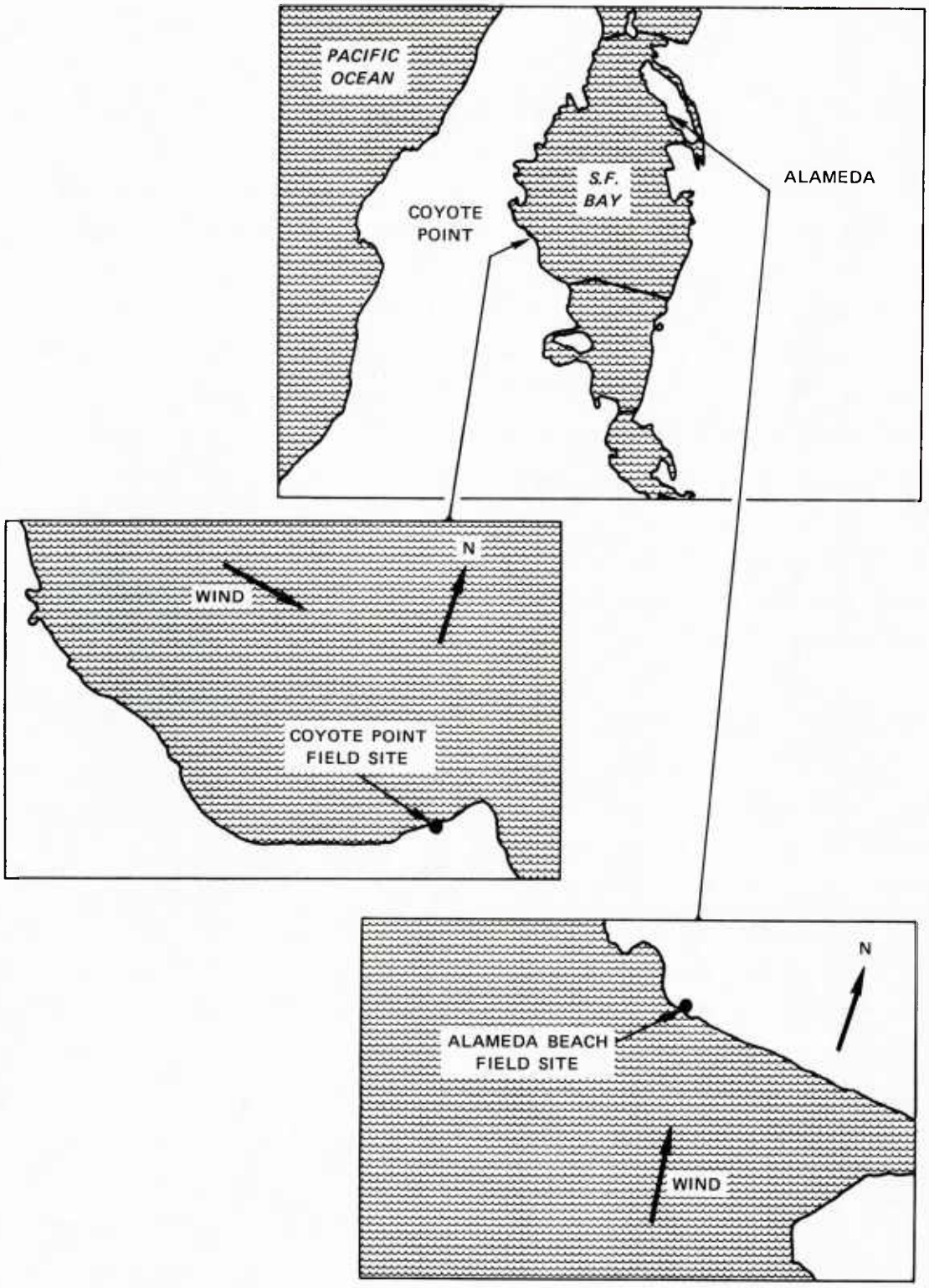

FIGURE 2 MAP SHOWING THE LOCATION OF THE ALAMEDA AND COYOTE POINT FIELD SITES AND THE PREDOMINANT WIND DIRECTIONS THAT PREVAILED DURING EXPERIMENTS

Table 1

WIND SPEED AND DIRECTION DURING
THE ALAMEDA EXPERIMENT

Local Time (PDT)	Speed (m/s)	Direction (deg)
1250	3.1	165
1334	3.1	150
1428	3.3	165
1440	5.2	170
1500	4.4	180

A 16-mm Bolex movie camera was used to simultaneously record time series of the incident waves at offshore wave staffs and the run-up on the beach face along a single line of 24 aluminum reference stakes. The reference stakes were positioned in a linear transect normal to the shoreline extending about 14 m in the offshore direction (Figure 3). The reference stakes were ultimately used to calibrate the time series of the incident waves and run-up in the oblique photographs and for spatial correlation of the incident-wave and run-up measurements. The camera was positioned on a 1-m high bluff just shoreward of the reference stake array. The camera was aimed to record low-oblique photographs, with the lens axis oriented nearly parallel with the reference stake transect.

Transit and level field survey methods were used to establish the position and elevation of the reference stakes relative to a datum stake located on the bluff. The elevation of the movie camera mounted on the tripod was surveyed, and the distance and elevation of the top and bottom of each reference stake were measured relative to the datum stake and the camera. The distances between all stakes and the heights of all stakes were measured independently with a steel tape measure. The elevations were surveyed accurate to 0.3 cm (0.01 ft), as were the horizontal distances. Reference surveys that included offshore profiles were made both before and after the experiment to confirm that no observable change

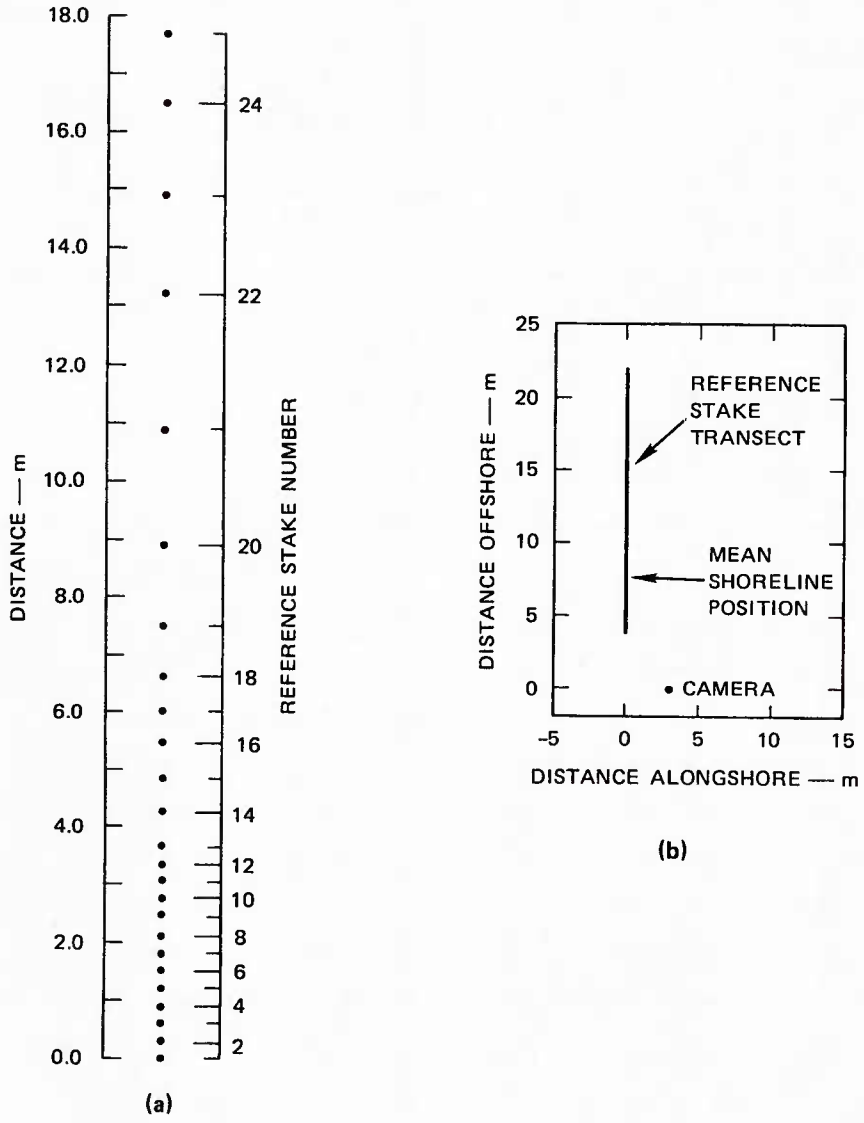

FIGURE 3 PLAN VIEWS OF ALAMEDA BEACH REFERENCE STAKE ARRAY. (a) Reference stake numbers and spacing between stakes. (b) Location of camera relative to reference stake transect and approximate shoreline position.

occurred in the offshore profile during the experiment. The heights of the reference stakes were measured with a steel tape and compared to the elevation survey measurements as a second check. Agreement between the measured and computed heights of the reference stakes was better than 1 cm in all cases. Figure 4 shows the Alameda beach profile computed from the survey measurements. The beach had a slope of approximately 0.11 (6.2°), becoming nearly horizontal about 12 m offshore.

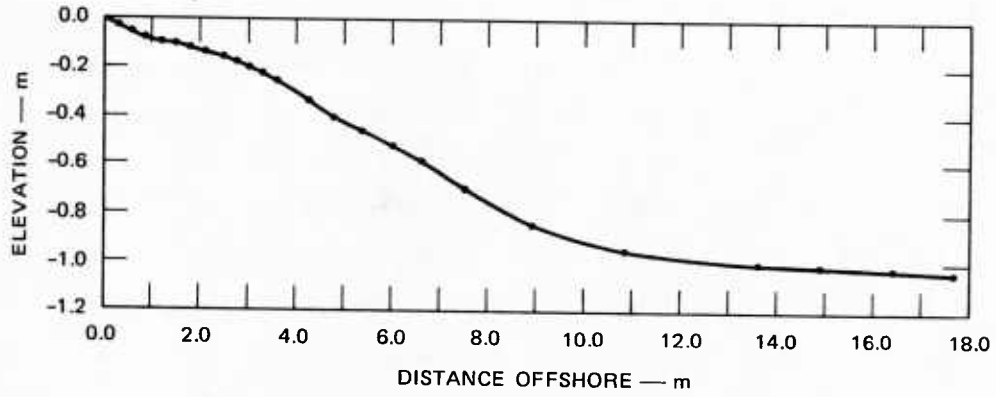

FIGURE 4 ALAMEDA BEACH TOPOGRAPHIC PROFILE

The movie camera was adjusted to record at approximately 10 frames per second. A 30.5-m roll of Kodak Kodachrome 25 color movie film was used to produce a photographic record of just over 5 minutes length. Rain fell throughout the day, but the resulting poor light conditions did not severely diminish the quality of the photographic record. An observer using a stopwatch and arm signals provided the required cross-check on the camera exposure rate during the experiment (because of the rain, the large electric clock intended for this purpose was not used).

B. Coyote Point Beach

The beach at Coyote Point was nearly linear in the alongshore direction in the vicinity of the study area and was openly exposed to northerly and northwesterly wind waves (Figure 2). The beach was composed of very small gravel and coarse sand. The beach slope was nearly constant in both the alongshore and offshore directions and formed a low-energy dissipative system with the incident-wave conditions present during the experiment.

The 16-mm Bolex movie camera used for the Alameda field experiment was also used to record the time series of the incident waves offshore and the run-up on the Coyote Point beach face. A portable battery pack was used to power the motordrive on the camera.

A two-dimensional grid composed of 80 wooden reference stakes provided the datum control for the Coyote Point experiment. The stakes, which were painted fluorescent green and red to aid visual recognition of different grid rows in the color movie frames, were arranged as shown in Figures 5 and 6. Figure 5(a) shows the array of reference stakes, the movie camera on a tripod, and the field survey transit. Level and transit field survey techniques were used to locate the position of each stake relative to the surrounding stakes and the camera as described for the Alameda measurements. It was necessary to measure the elevation of the top and bottom of each of the 80 stakes, the distances between all the stakes, and the relative distances from the camera to key reference stakes. The elevations were surveyed accurate to better than 0.3 cm, as were the horizontal distances. The configuration of the reference stake array is shown to scale in Figure 6. To maximize the number of possible alongshore correlation length combinations, a modified prime number scheme was used to determine stake placement in the alongshore direction. Three long lines of stakes transect the shoreline and extend offshore. The stakes located on the beach face were spaced closer together to increase the available resolution of the run-up measurements. Figure 7 shows the orientation of the reference stake array relative to the camera, which is positioned at the origin of the plot; also shown is a triangular array of three stakes located well seaward of the breaker zone and used for definition of the offshore incident-wave field.

A battery-powered electric clock (Appendix F) was constructed for the experiment and used to calibrate the exposure rate of the movie camera (Figure 5). The single sweep hand on the clock rotated throughout the experiment at a calibrated constant rate, providing a measure of elapsed time in each photographic frame of the movie film. The rate of rotation of the clock's sweep hand was calibrated before, during, and after the experiment; the rotation rate remained constant throughout the experiment.

The time series of the incident waves and run-up were recorded from three different camera locations on the beach. A total of five

FIGURE 5 PHOTOGRAPHS TAKEN BEFORE HIGH TIDE SHOWING COYOTE POINT FIELD SITE AND SURVEYED ARRAY OF REFERENCE STAKES

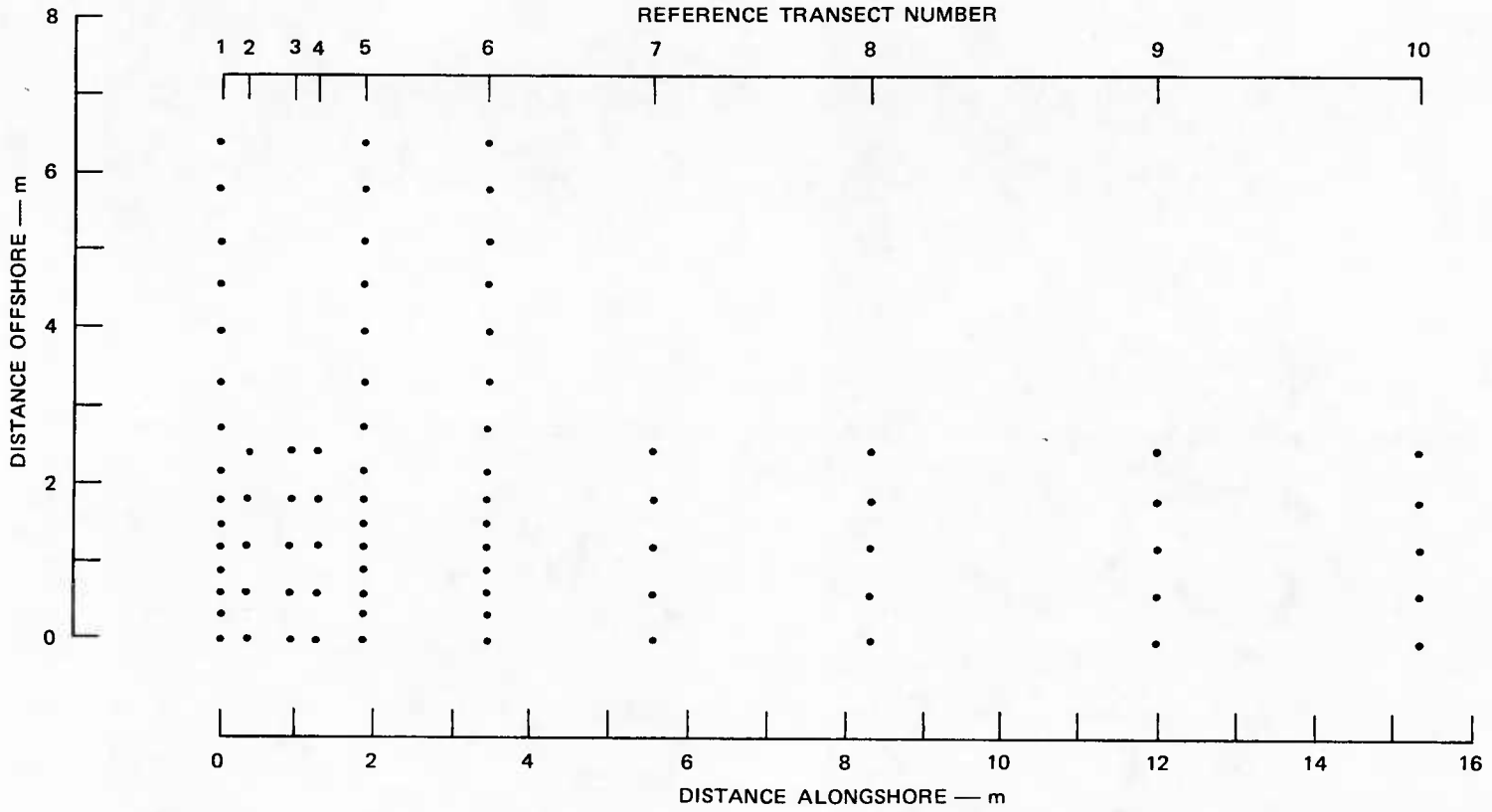

FIGURE 6 PLAN VIEW OF THE TWO-DIMENSIONAL ARRAY OF REFERENCE STAKES USED FOR THE 14 MAY 1982 COYOTE POINT RUN-UP FIELD EXPERIMENT

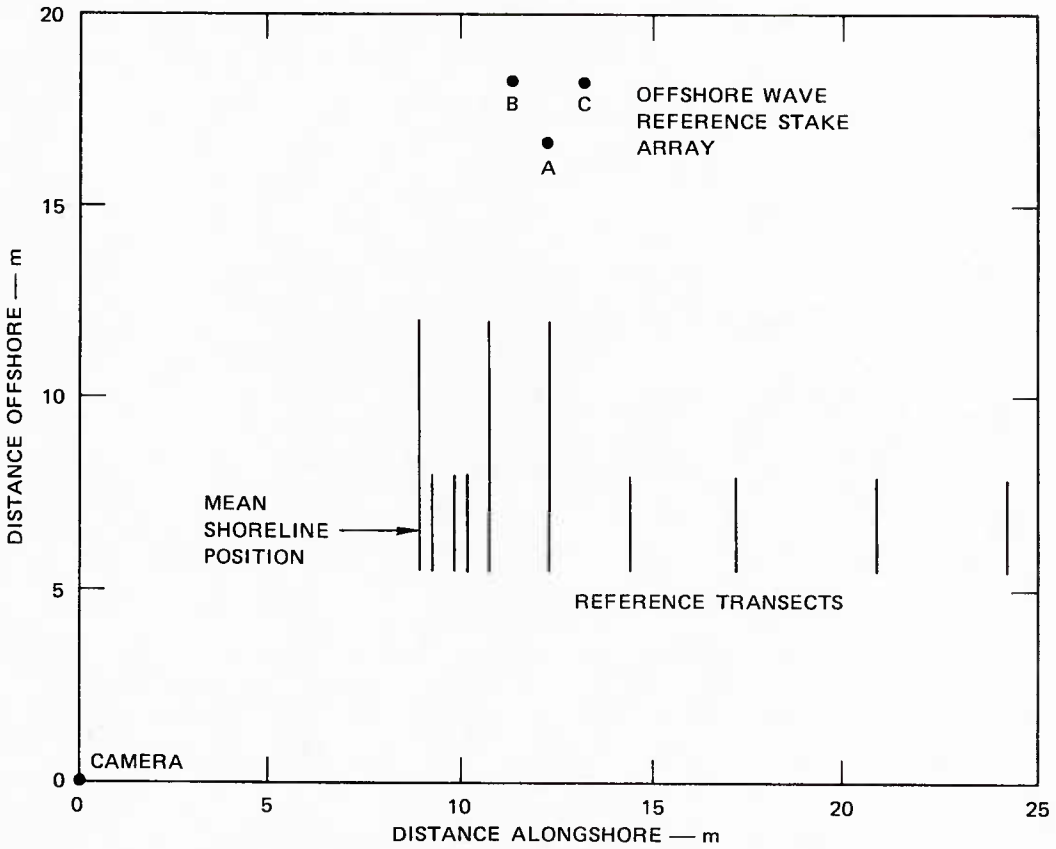

FIGURE 7 PLAN VIEW SHOWING LOCATION OF THE CAMERA RELATIVE TO REFERENCE STAKE TRANSECTS AND OFFSHORE INCIDENT-WAVE REFERENCE STAKE ARRAY

30.5-m rolls of Kodak Kodachrome 16-mm color movie film were used: four rolls of unfiltered ASA 25 daylight film and one roll of filtered ASA 40 tungsten balanced film. The camera was set for an exposure rate of 14 frames per second, and approximately 5.5 minutes of time series data were recorded on each roll of film. Approximately 5 minutes were required to change the film in the camera.

To maintain continuity of the mean water level during the experiment, time series were recorded between about 1810 and 1905 PDT during the peak of the high tide, which occurred about 1822 PDT. Some of this time was required to change the film and to reposition the camera between the three viewing locations.

The low angle of the sun at the time of the experiment and the westerly component of the camera line of sight allowed some sunlight to be reflected into the camera lens. This reflected light slightly degraded the quality of the movie photographs, restricting analysis to correlation distances of up to 5 m.

The wind speed and direction during the experiment was measured using a hand-held anemometer-compass. Table 2 shows that the winds were quite strong and were nearly constant in their direction throughout the experimental period. The winds blew consistently throughout the day, creating a well established wind-wave field by early afternoon. The waves were nearly normal in incidence to the Coyote Point Beach at the location of the reference stake array as shown in Figures 2 and 5. Plunging breakers such as those shown in Figure 5(b) were observed throughout the afternoon and during the data recording period of the experiment.

Table 2

WIND SPEED AND DIRECTION DURING
THE COYOTE POINT EXPERIMENT

Time (PDT)	Speed (m/s)	Direction (deg)
1639	7.2	270
1655	7.2	285
1905	6.7	280
1914	8.1	280

A number of calculations were required prior to actual analysis of the photographic time series of incident waves and run-up. The camera exposure rate was verified by review of the movie frames. The field survey notes were compiled, and the elevations, distances, and angles relating the positions between reference stakes and their positions relative to the camera were computed and subsequently used to compute

the topographic profiles. The beach topography and nearshore profiles were surveyed both before and after the experimental data were recorded. A least-squares linear regression was used to compute a mean nearshore beach slope for each profile transect. Figure 8 shows the full profiles for each of the three long survey transects, numbers 1, 5, and 6. The transects and profiles were numbered from left to right along the beach (Figure 6). Figure 9 shows profiles for all of the transects and data for the first nine reference stakes of transects 1, 5, and 6. The vertical elevation in meters relative to the first stake (furthest onshore) in each transect is plotted with respect to the offshore distance in meters in all the profiles of Figures 8 and 9. The post-experiment survey showed that, during the experiment, little or no change had occurred in beach profile either alongshore or offshore within the surveyed reference grid. Table 3 shows the beach slope computed for each profile using least-squares linear regression of the elevation versus offshore distance. In all cases, the correlation coefficient of each fit was better than 0.98. The mean beach slope across all survey transects was 4.62° $\pm$0.35°.

Table 3

COYOTE POINT BEACH SLOPES

Transect	Slope (deg)
1	4.8
2	4.9
3	4.8
4	5.0
5	4.5
6	4.1
7	4.4
8	4.3
9	4.2
10	5.2

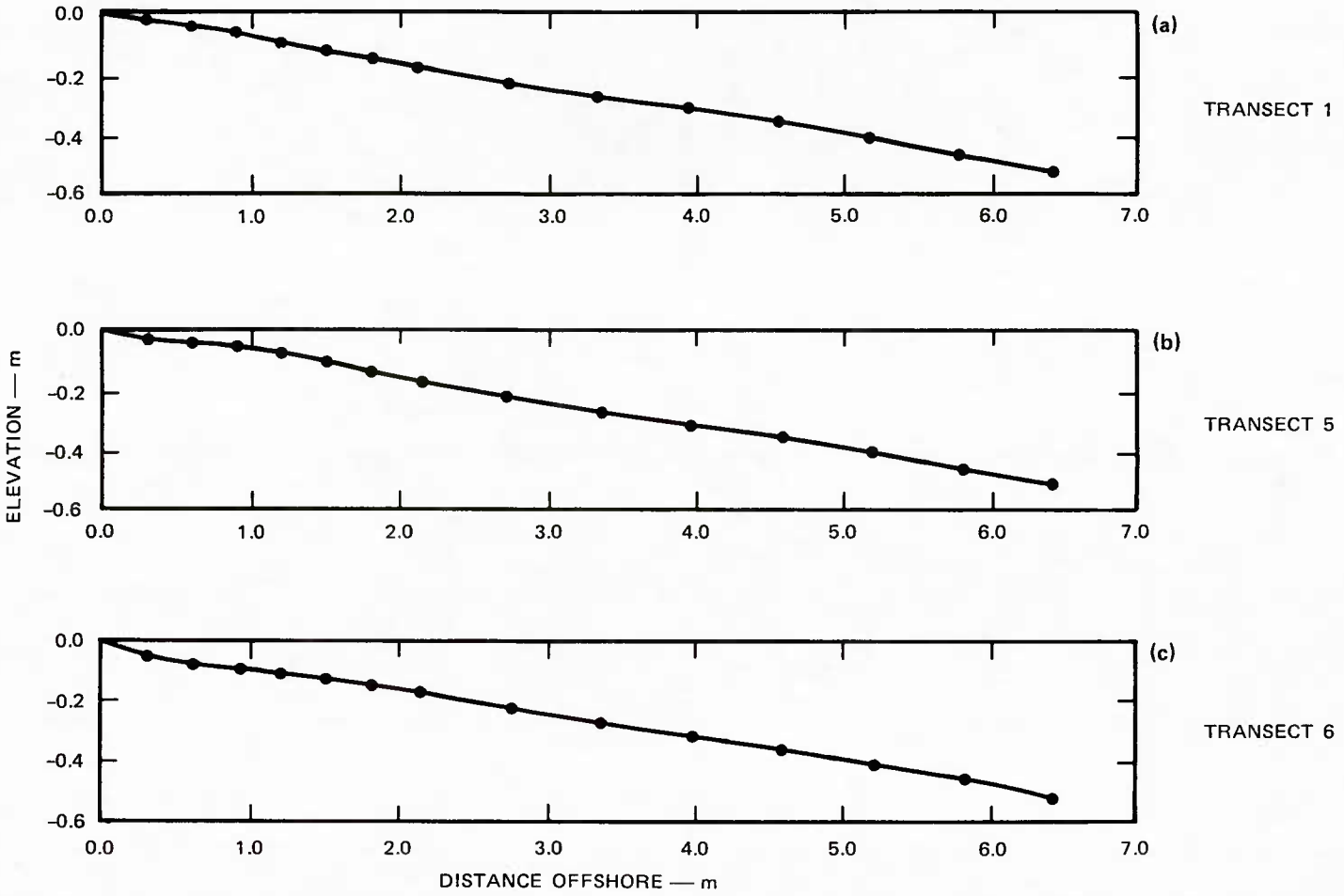

FIGURE 8 BEACH PROFILES FOR COYOTE POINT TRANSECTS 1, 5, AND 6

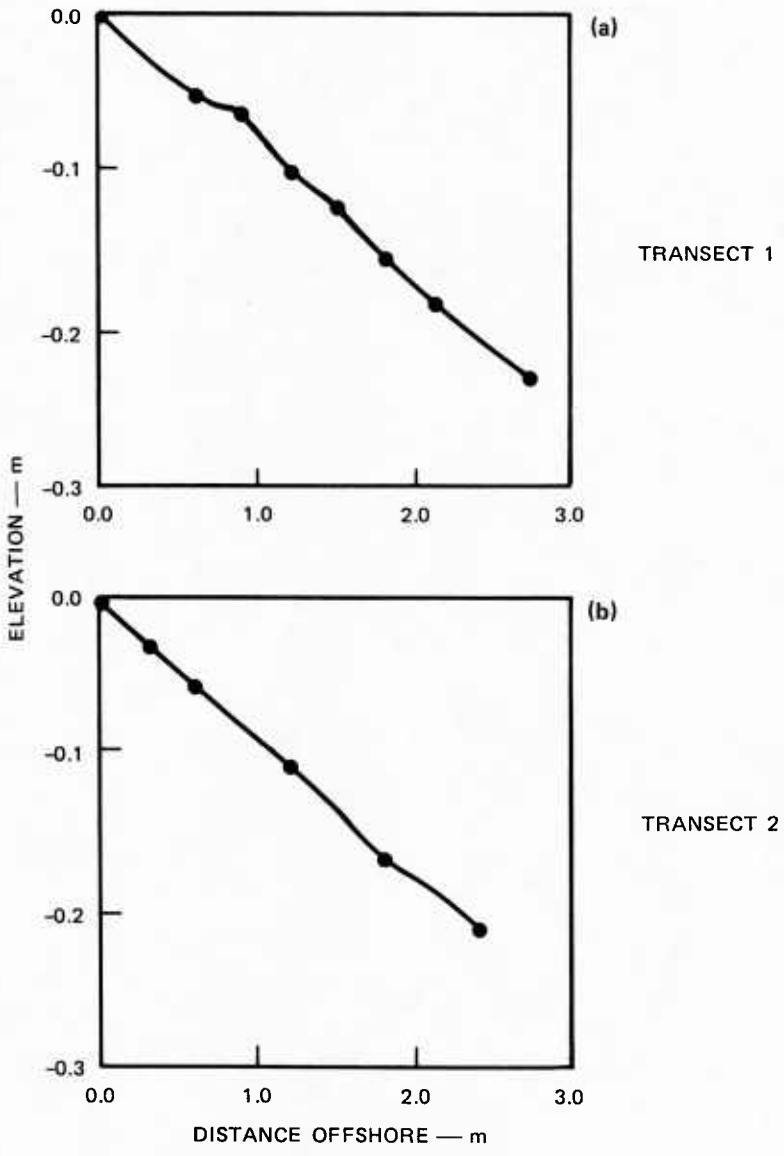

FIGURE 9 BEACH PROFILES FOR COYOTE POINT TRANSECTS 1-10

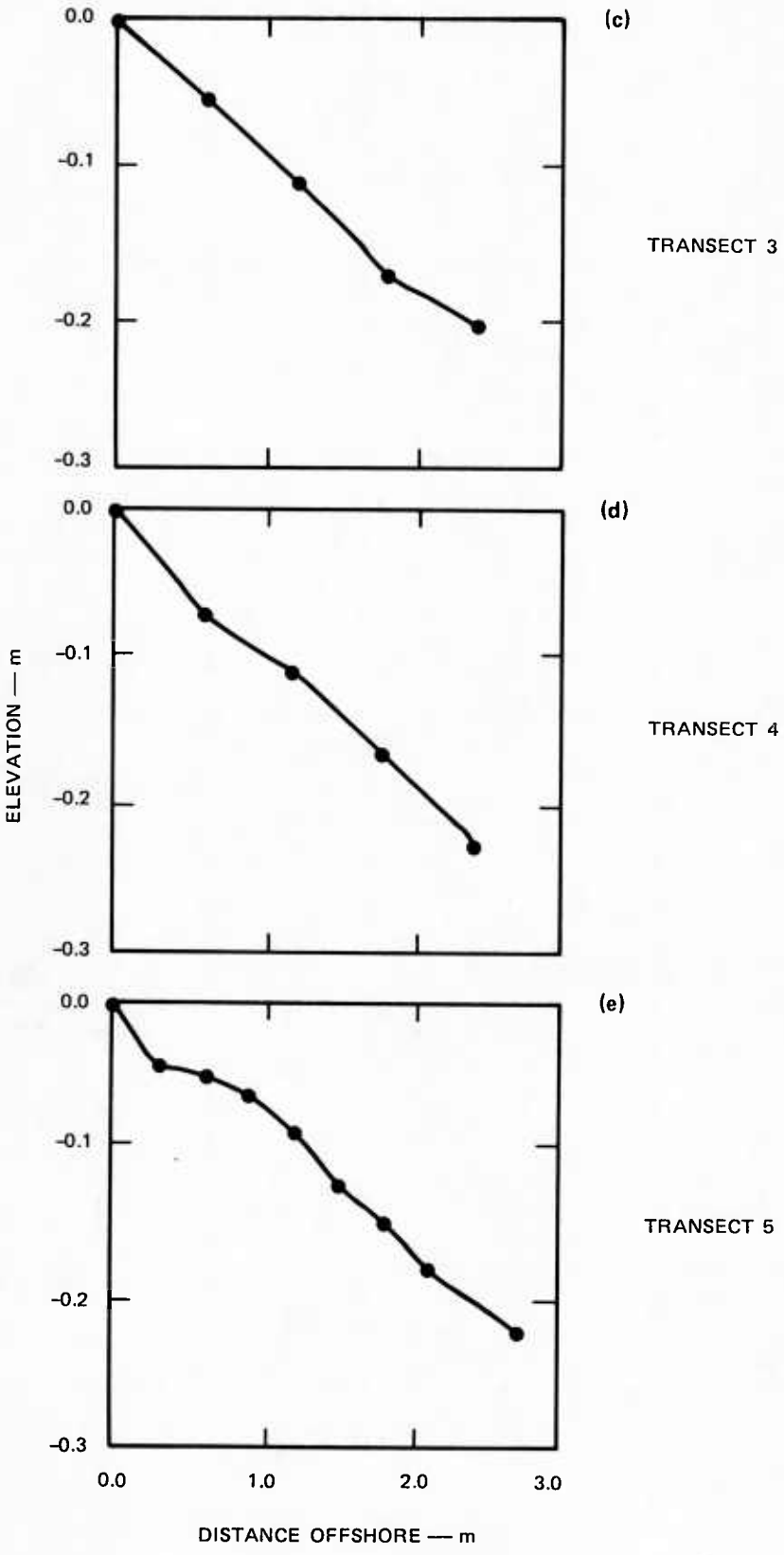

FIGURE 9 (Continued)

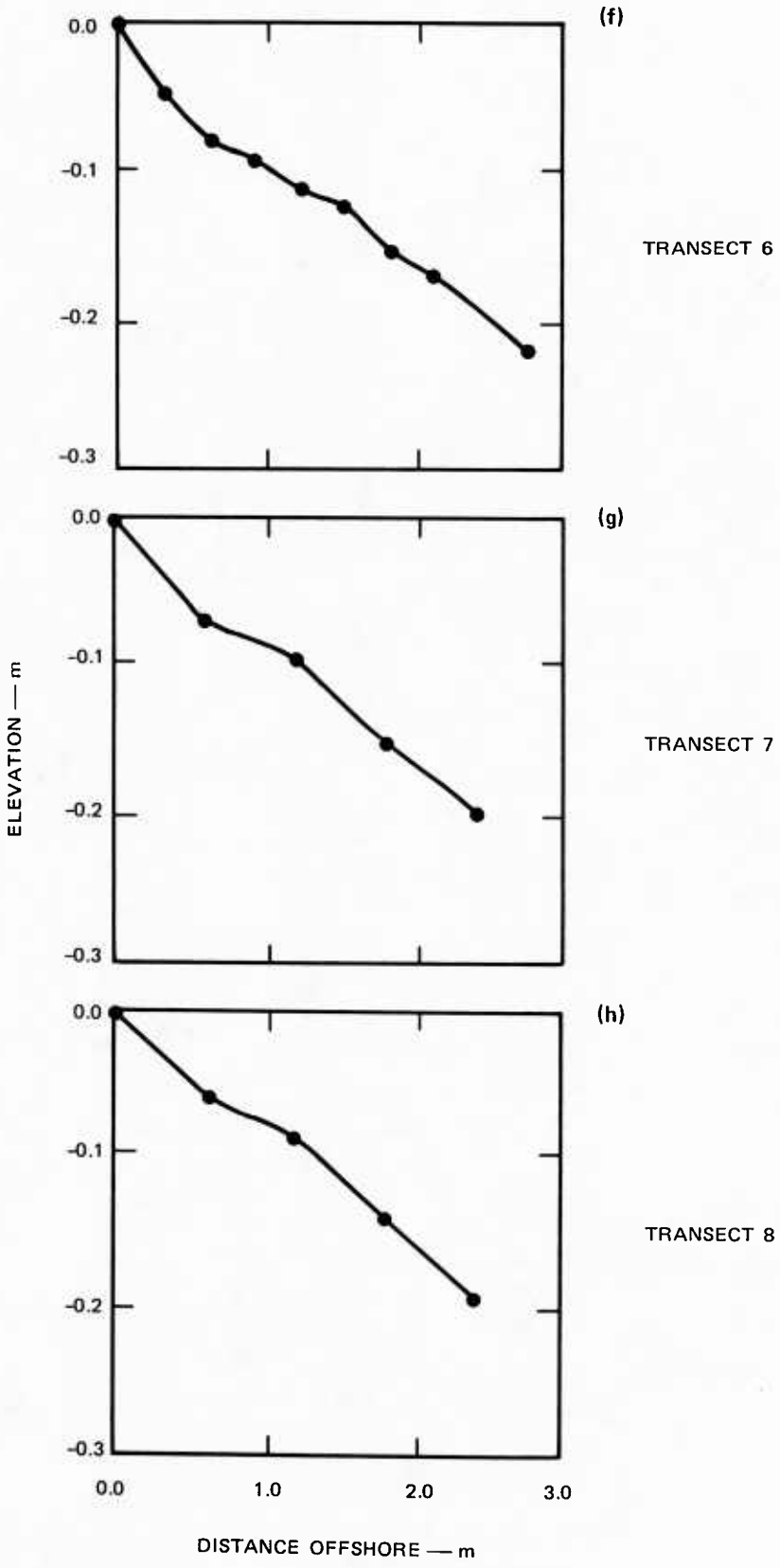

FIGURE 9 (Continued)

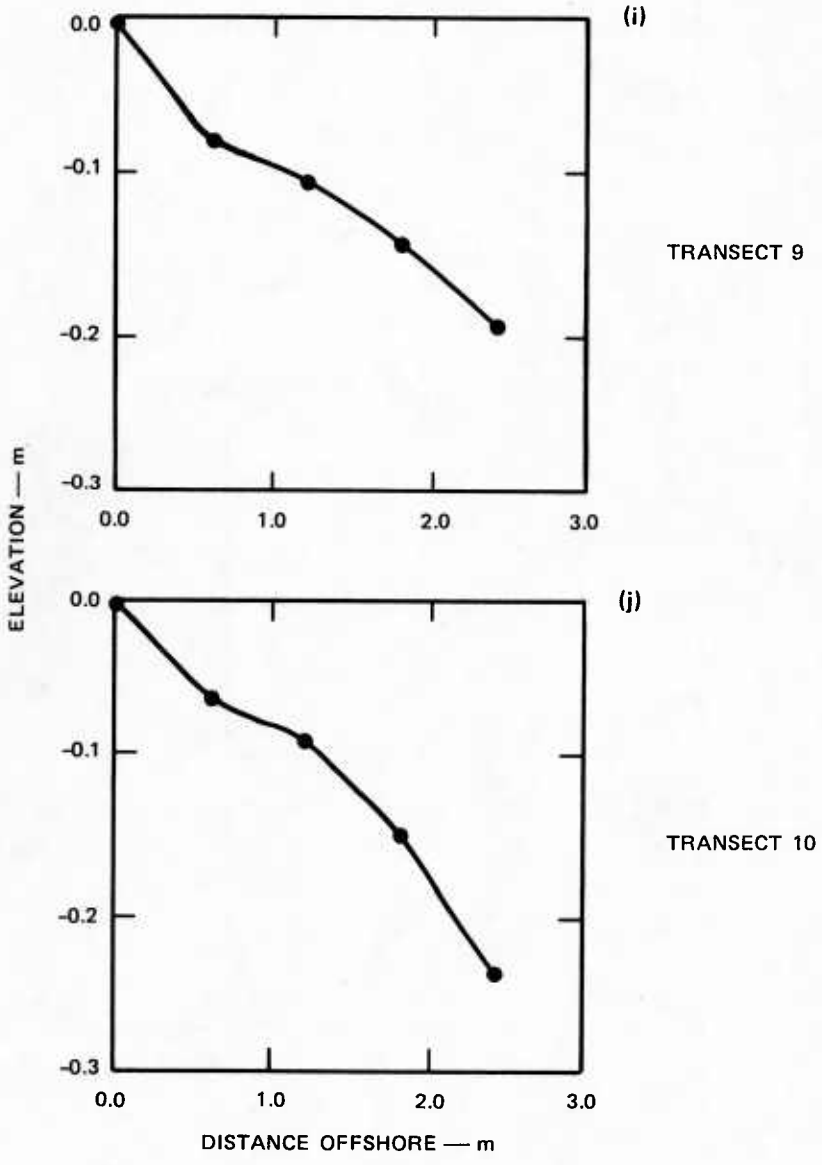

FIGURE 9 (Concluded)

The beach slopes and incident-wave heights present on the day of the experiment produced the requisite dissipative beach system with a representative ε value of approximately 19 (Appendix D). The presence of plunging breakers (Figure 5b) also supports the identification of the beach as a dissipative and not a reflective system. No visible signs of edge wave activity, such as beach cusps or regular alongshore spatial modulation of the run-up, were observed at any time during the experiment. Only one breaker zone was present, and the surf zone was narrow.

IV DATA ANALYSIS

A. Digitizing the Photographic Record

Time series of the incident waves were derived from the 16-mm photographic record by digitizing the amplitude fluctuations of the waves as they passed the offshore reference stakes. Similarly, the run-up time series were developed from the movie record by digitizing the position of the leading edge of the run-up on the beach face. The sequence of processing steps required to prepare a calibrated incident wave or run-up time series from the photographic record is shown schematically in Figure 10.

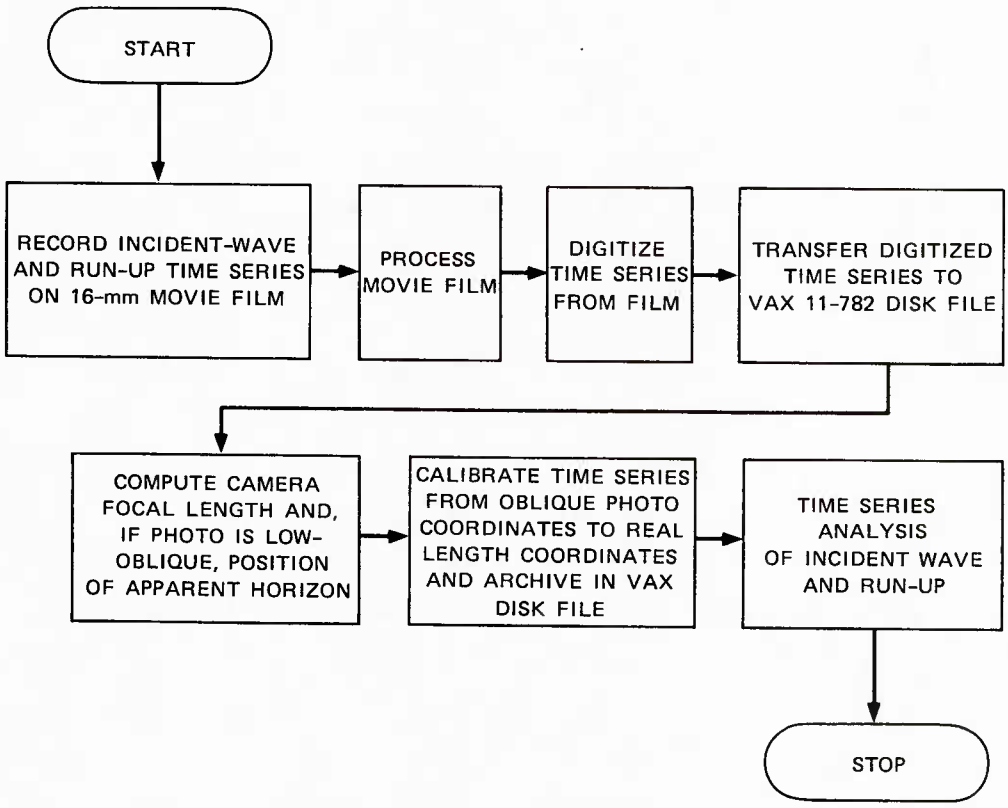

FIGURE 10 DATA PROCESSING FLOWCHART FOR RUN-UP TIME SERIES CALIBRATION FROM THE PHOTOGRAPHIC RECORD

Points of interest appearing in the processed 16-mm movie frames were digitized manually using a photodigitizer at SRI International (SRI). The oblique photographic image was projected onto a Tektronix 4956 Graphics Tablet connected to a Tektronix 4052 terminal; an electronic pad with crosshairs was then used to digitize the points of interest appearing in the photograph. The resolution of the graphics tablet is approximately 0.025 cm (0.01 in.). The digitized points were stored on cassette tape and subsequently transferred from the Tektronix terminal to a disk file on the DEC VAX 11-782 computer.

The leading edge of the run-up on the beach face was digitized in the photographs along the reference stake transect selected for analysis. It was relatively easy to identify the position of the leading edge of the run-up in the photographs due to the presence of seafoam on the beach. The seafoam provided an effective tracer of run-up in the photographs since it rode the leading edge of the shoreward rushing water up the beach during the run-up phase of the swash cycle and followed the seaward-moving water surface during backwash. In addition, the flow patterns around the other inundated reference stakes were readily observable and proved helpful in verifying the continuity of the swash layer on the beach face.

The incident-wave amplitude time series was developed at the selected reference stakes by digitizing the intersection of the fluctuating water surface with the stake. As with the digitized run-up time series, the product of digitizing was a digital time series of oblique photo coordinates in arbitrary digitizer units. The next step was to calibrate these time series to physical length units of centimeters. Photogrammetric analysis techniques were used to compute the transfer function for the coordinate transformation required to properly calibrate the time series.

B. Photogrammetric Analysis

The digitizing process described above was identical for both field photographic data sets. The subsequent processing of the digitized oblique photo coordinates was more complicated for the incident-wave

data than for the run-up data. It was not possible to calibrate the field-measured incident-wave amplitude time series directly from the photographs, as was done for the run-up, and photogrammetric analysis methods were required. The analysis techniques used for the calibration are summarized below.

1. Analysis of Single-Image Oblique Photographs

Both single-image and stereoscopic-image oblique photographs have been used to make quantitative distance and height measurements in the nearshore zone and on the beach. Aircraft, helicopters, and balloons have been used to study shoreline changes (Stafford et al., 1973), directional ocean-wave spectra (Cote et al., 1960), and longshore currents (Sonu, 1969). Winter ice-ridge formation and break-up along the Lake Michigan coastline (Seibel et al., 1975, 1976), longshore currents (Pincus, 1959), and storm-related beach changes (Maresca, 1975) have been monitored and quantitatively studied by using terrestrial oblique photography.

Several of these studies have used a 35-mm single-lens reflex camera with a normal 50-mm lens to record the data photographically. The laboratory and field data reported here were recorded using a 16 mm-movie camera. Since the movie film consists of a series of single-image photographs, the analysis techniques are the same for both types of photography. No special or unusual photographic equipment is required to make the measurements described herein.

The photographic method of measurement has several distinct advantages over other methods providing virtually the same information:

- The photographic method is inexpensive, simple to install, reliable, and accurate.
- Photographs provide a permanent data record available for subsequent visual review.
- Field calibration of the photographic system requires little time.
- The photographic method may be used to provide data where in-situ conditions disallow the use of other methods that provide similar data.

There are, however, several disadvantages to using a photographic data acquisition system:

- Inclement weather and adverse light conditions may degrade the quality of the photographs.
- Assurance of a clear and complete photographic record is postponed until film processing is complete.
- Valuable data may be lost due to mishandling of the film during processing.
- Analysis of the photographs may be tedious and time-consuming.
- The visual resolution of the photographs, and consequently the accuracy of data recorded in the photographs, decreases with increasing distance from the camera.

2. Geometry of Oblique Photographs

Vertical photographs are taken from an exposure station located directly above the subject of interest with the camera axis pointed vertically downward. Oblique photographs are taken with the camera axis inclined at an angle to the vertical. If the angle of inclination is large enough that the horizon appears in the photograph, a high-oblique photo is recorded. If the camera axis is inclined relative to vertical, and the horizon is not visible in the photograph, the photograph is termed low-oblique. In either case, it is possible to extract real ground distances and elevations from vertical and oblique photographs if the required datum controls are provided.

High-oblique surf zone measurements can be made at virtually any location, providing the camera is elevated sufficiently above the mean water level and the horizon is visible in the photograph. Heights and real ground coordinates relative to the camera location can be computed for objects appearing in the high-oblique photographs without additional ground control. Analysis of low-oblique and stereoscopic photographs requires that reference stakes or other datum controls be visible in the photograph. The data for the Coyote Point field experiment were recorded using high-oblique photography, and the Alameda field data were recorded using low-oblique photography. The following discussion will highlight analysis of both high- and low-oblique photographic images.

Oblique and stereoscopic image processing is described in greater detail in several references (American Society of Photogrammetry, 1966; Wolf, 1974; Maresca and Seibel, 1976).

Several methods for computing heights and ground coordinates from oblique photographic images are described in the open literature. The Equivalent Vertical Photograph Method was used in the analysis of both the high- and low-oblique photographs taken in the experiments reported here. An equivalent vertical photograph is the imaginary, truly vertical photograph taken with the same camera from the same exposure station as the tilted (oblique) photograph. Figure 11 shows schematically an example of a typical field geometry that might be used for terrestrial photographic measurements of the surf zone. The figure shows a reference stake on the beach, and a breaking wave located at an offshore reference stake. During the Alameda and Coyote Point field experiments, many surveyed reference stakes were used both offshore and on the beach face to provide photo datum control and time series calibration points.

To facilitate digitizing of points appearing in the picture, the oblique image on the film transparency must be enlarged, which may be done using either a standard film or slide projector or more sophisticated projection equipment. The movie frames used in the laboratory and field measurements reported here were enlarged and projected onto a viewing table on a photodigitizer. The objects of interest in the enlarged oblique photograph were located and marked as shown in Figure 12. The figure shows the Cartesian photo coordinate system for both high- and low-oblique photographs. The Cartesian photo coordinates of these points marked on the oblique image are positioned relative to an origin at the center, or principal point, of the projected enlarged photograph. The Equivalent Vertical Photograph Method of oblique photo analysis permits transformation of these oblique photo coordinates into the coordinates of the equivalent vertical photograph. The coordinates of the equivalent vertical photograph are then used to compute the real ground coordinates of the specified points of interest in the photo.

The geometry of the high-oblique image required for computation of the real spatial coordinates may be derived from the principal plane

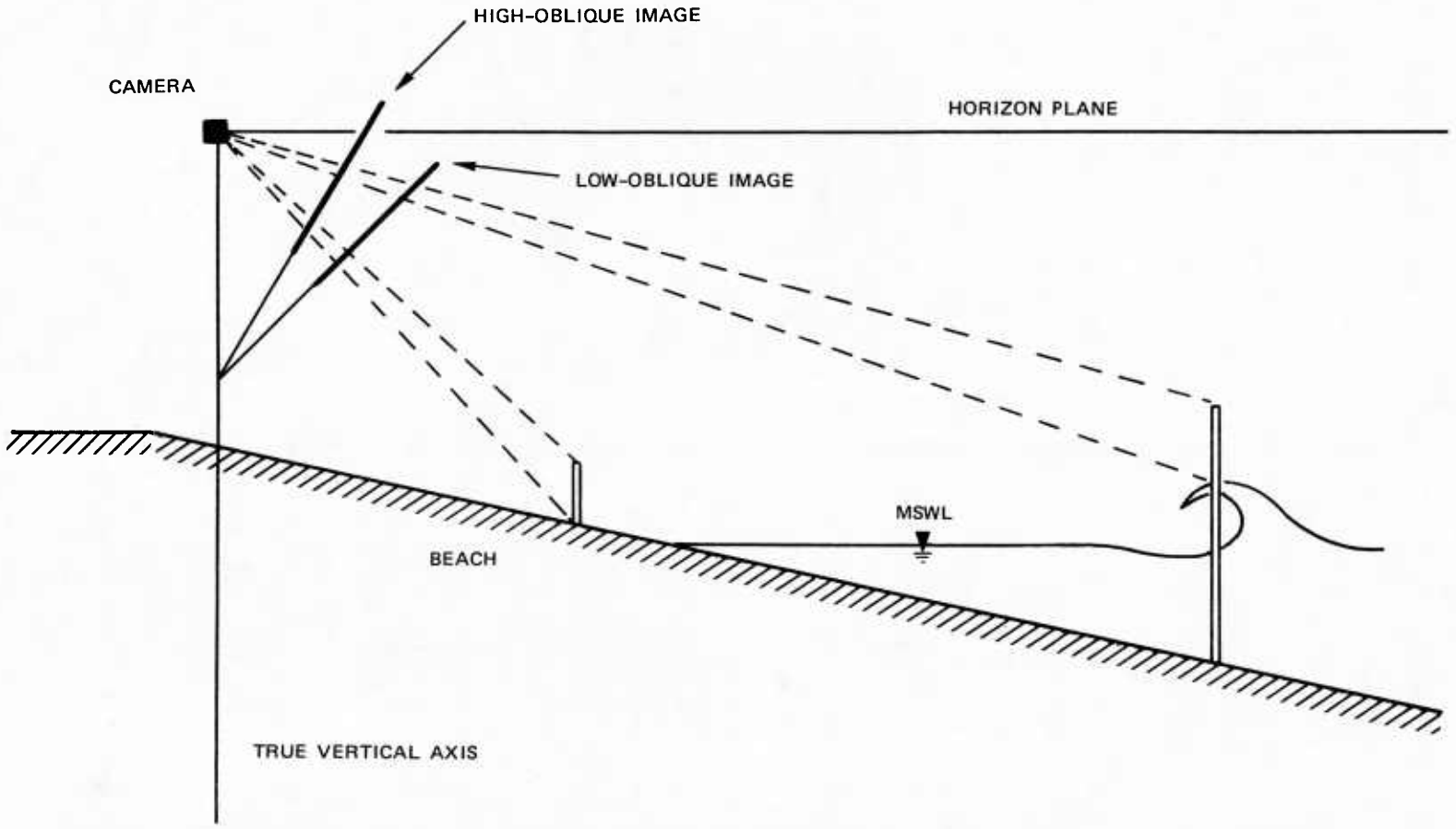

FIGURE 11 SCHEMATIC SHOWING TYPICAL GEOMETRY FOR TERRESTRIAL-PHOTOGRAPHIC MEASUREMENTS OF INCIDENT WAVES AND RUN-UP ON THE BEACH. Both high- and low-oblique image planes are shown, as are two typical reference stakes for photo calibration.

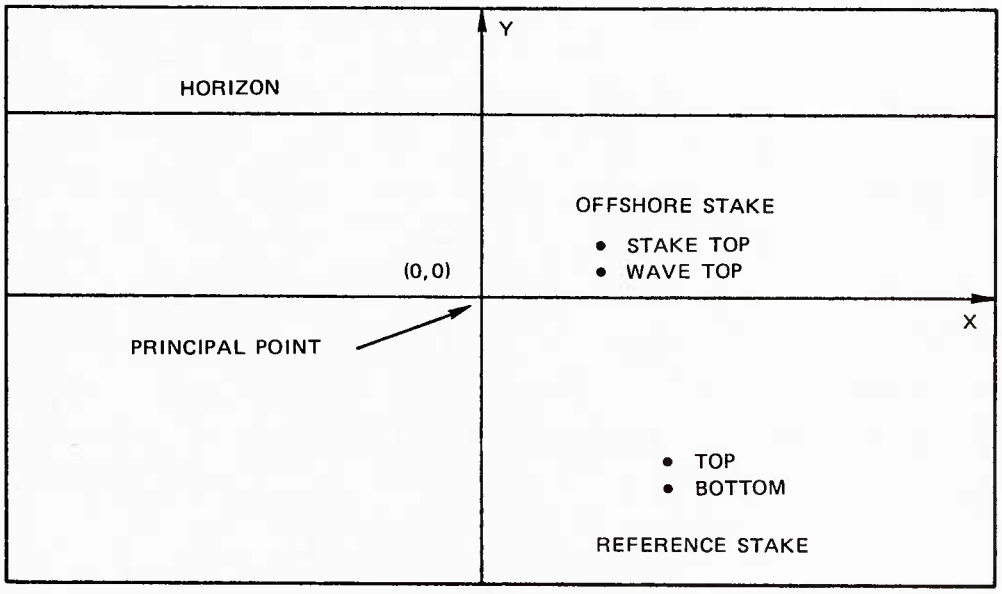

(a) HIGH-OBLIQUE IMAGE

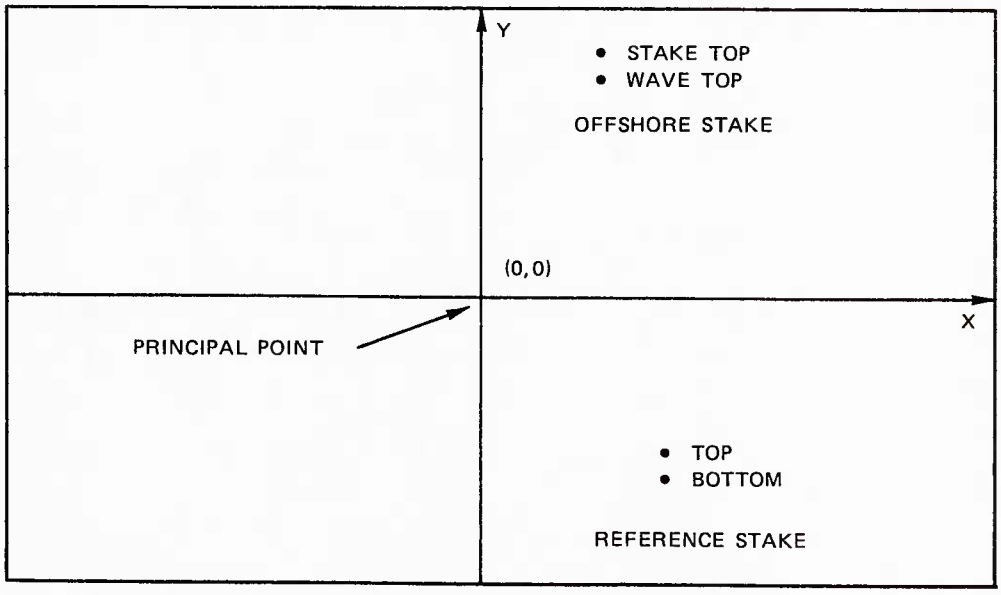

(b) LOW-OBLIQUE IMAGE

FIGURE 12 HIGH-OBLIQUE AND THE CORRESPONDING LOW-OBLIQUE IMAGES OF THE REFERENCE STAKES SHOWN IN FIGURE 11. The horizon appears only in the high-oblique image.

diagram shown in Figure 13. In Figure 13, $\overline{TI}$ represents the plane of the positive of a photograph taken by a camera with focal length f_c. Point P is the principal point of the image, and T is the intersection of the true horizon with the principal plane. A vertical line intersects the plane of the photograph at N, the photographic nadir point. The apparent horizon is located at X, and the tilt angle is given by $\tilde{t}$. The bisector of the tilt angle intersects the plane of the tilted photograph at point I, and a horizontal line through point I and parallel with the plane of the true horizon defines the plane of the equivalent vertical photograph, $\overline{N'I}$. The line of intersection of the plane of the tilted photo with the plane of the equivalent vertical photo is the axis of tilt or the isoline. Images along the isoline have the same photographic positions in both photos.

The real ground coordinates and heights of objects in the oblique image can be calculated from the geometry of the principal plane diagram. Following Maresca and Seibel (1976), the magnification, C, of the projected image on the photodigitizer is given by:

$$C = d_1/d_2 \tag{1}$$

where d_1 is the height of the film transparency and d_2 is the height of the enlarged picture projected on the screen. Points P, T, I, and N on the principal plane diagram can be calculated from the geometry if any two points are known. The points P and T are easily measured from the projected oblique image. Point P is located at the principal point of the projected oblique image, that is, at the center of the image as shown in Figure 12. The apparent depression angle, θ', is:

$$\theta' = \arctan(C\ PT/f_c) \tag{2}$$

where f_c is the focal length of the camera. The apparent horizon is actually lower than the true horizon and should be corrected by an amount $\delta\theta$:

$$\delta\theta = 0.98(H)^{1/2} \tag{3}$$

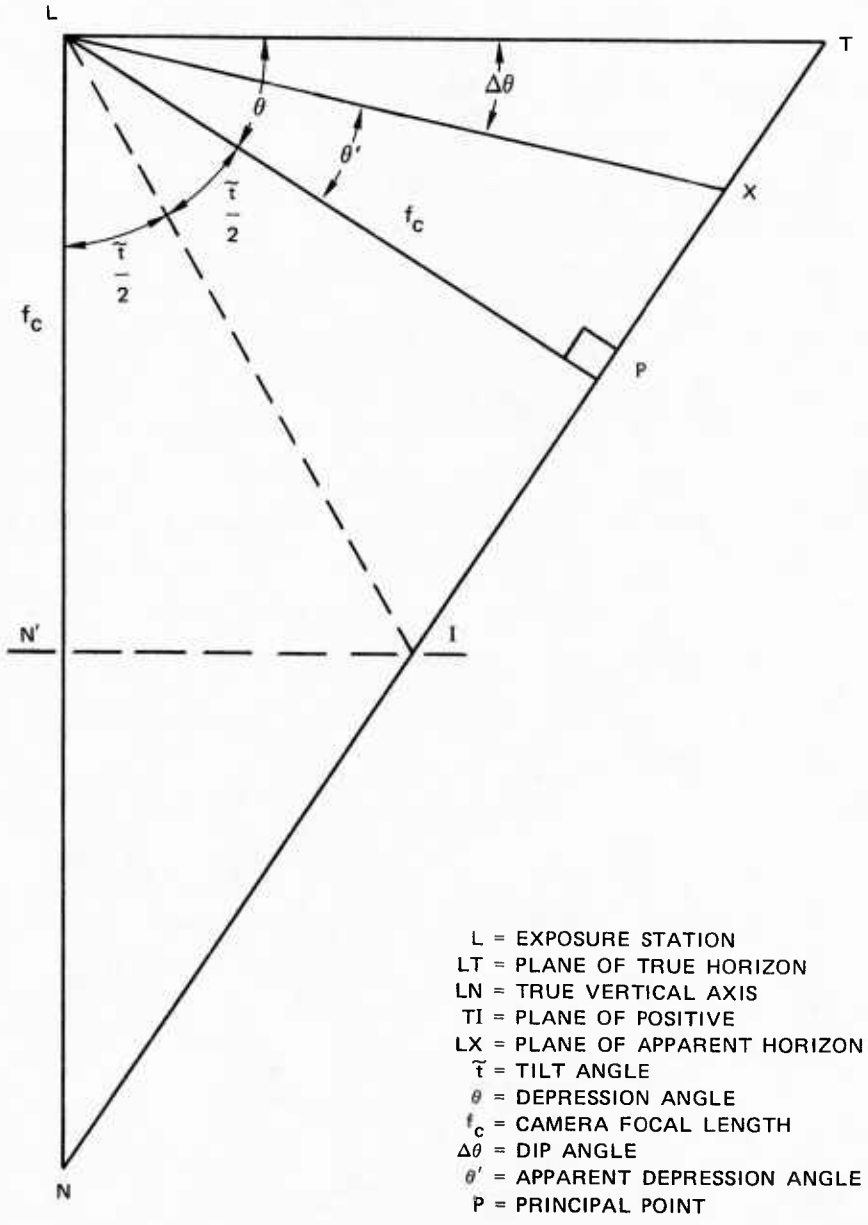

FIGURE 13 PRINCIPAL PLANE DIAGRAM USED TO DEFINE THE GEOMETRY OF OBLIQUE PHOTOGRAPHS

where H is the height in feet of the camera above the datum and where $\delta\theta$ is in minutes. The true depression angle is then given by:

$$\theta = '\theta' + \delta\theta \quad . \tag{4}$$

In low-oblique photographs such as those recorded during the Alameda experiment, the apparent horizon is not visible in the photograph (Figure 12). The depression angle, θ, for a low-oblique photograph must be computed based on the image of the reference stakes (or other surveyed datum control points) appearing in the photo. The position of these control points may be projected back from the plane of the oblique image shown in Figure 11 to define the principal plane diagram for the low-oblique photograph. The principal plane diagram for a low-oblique photograph is basically the same as that for a high-oblique photograph, except that the plane of the apparent horizon, $\overline{LX}$ in Figure 13, does not intersect the plane of the positive, $\overline{TI}$. The depression angle is computed directly from the geometry of the low-oblique principal plane diagram in the absence of the apparent horizon in the low-oblique image.

Noting from Figure 13 that the tilt angle, $\tilde{t}$, is expressed by:

$$\tilde{t} = \pi/2 - \theta \quad , \tag{5}$$

the following parameters may be derived from consideration of the geometry of the principal plane diagram:

$$\overline{PT} = f_c \tan(\theta) \tag{6}$$

$$\overline{PI} = f_c \tan(\tilde{t}/2) \tag{7}$$

$$\overline{PN} = f_c \tan(\tilde{t}) \tag{8}$$

$$\overline{TI} = \overline{PT} + \overline{PI} \tag{9}$$

$$\overline{TN} = \overline{PT} + \overline{PN} \tag{10}$$

$$\overline{NI} = \overline{PI} \quad . \tag{11}$$

Using Eq. (1) through (11), the coordinates of any point in the oblique image can be transformed to the coordinates of the equivalent vertical

photograph with origin at the camera. The x and y coordinates in the equivalent vertical photograph are given by:

$$x_{evp} = x_{ob}\, C\, (\overline{TI}/(\overline{TI}-K)) \tag{12}$$

$$y_{evp} = K\, (\overline{TI}/(\overline{TI}-K)) + \overline{NI} \tag{13}$$

where

$$K = y_{ob}\, C + \overline{PI} \quad . \tag{14}$$

In Eq. (12) and (14), x_{ob} and y_{ob} are the Cartesian coordinates in the oblique coordinate system with origin at the principal point. The real Cartesian ground coordinates with origin at the camera can then be computed from the equivalent vertical photograph coordinates:

$$x_{gr} = H\, x_{evp}/f_c \tag{15}$$

$$y_{gr} = H\, y_{evp}/f_c \quad . \tag{16}$$

Wolf (1974) derives the basic relief displacement equation for vertical photographs. Using his formula, the vertical height of objects appearing in the photograph may be estimated by:

$$h = \frac{d\, H}{r} \tag{17}$$

where h is the height of the object, d is the relief displacement of the object in the vertical photo, r is the radial distance on the photograph to the displaced image, and H is the elevation of the camera above the datum. The units of d and r must be the same. Both the top and bottom of the vertical object must be visible on the photograph to compute d. The datum may be selected arbitrarily but must be stationary from frame to frame in the photographic time series.

When using Eq. (1) through (17), it is necessary to maintain continuity of units and to correct for any scaling from the arbitrary photodigitizer coordinates to actual physical units of length on the oblique

image. The coordinates in the oblique image must be scaled relative to the principal point origin of the oblique photo, or an additional coordinate transformation is required.

The horizon must be horizontal in the oblique image. If the camera was tilted when the photographs were taken so that the horizon is not horizontal to within approximately 1°, a rotation of the oblique photo coordinates is required. Illuminated grid lines on the digitizing pad were used to verify that the horizon was horizontal in the field measurements reported here. This requirement must be considered during the field experiment when the camera is being set up.

3. Calibration of Run-Up from Oblique Photo Coordinates

Each run-up time series was produced by digitizing the location of the leading edge of the run-up along the selected transect appearing in the oblique image. It was possible to calibrate the run-up measured in the field directly from the oblique photo coordinates to physical units. One of the surveyed transects was selected for analysis of run-up, and the time series of the run-up along this transect was reviewed over the entire roll of film. The movie frame showing the maximum backwash during a swash cycle was identified. At this stage of the particular swash cycle, the greatest amount of "dry" beach face was exposed. During this time, the bottoms of the surveyed reference stakes penetrating the exposed beach face were clearly visible in the oblique image. The point of penetration was digitized for each reference stake along the transect from the stake furthest seaward (now temporarily exposed) to the landward-most stake.

The distances between all reference stakes in all transects were measured in the field during the survey conducted prior to the data-recording phase of the experiment. Given the oblique photo coordinates of the reference stake positions and the measured physical distances between the stakes, it was only necessary to correlate the two to provide the required calibration. A linear least-squares regression analysis was used for this calibration. The measured physical distances between

the stakes were regressed relative to the corresponding digitized photo coordinates, producing a simple linear calibration equation for run-up along the selected transect. This calibration equation was used to transform the time series of run-up measured in oblique photo coordinates to a run-up time series calibrated in real ground coordinates of centimeters.

This calibration procedure was repeated for all the run-up measurements. The correlation coefficient in each instance was better than 0.99, and the positions of the reference stakes computed using the calibration equation agreed with the distances measured in the field to better than 2.5 cm. This is excellent agreement, considering that small, 16-mm film was used instead of larger, 35-mm film and that the camera was located as much as 15 m from the mean run-up position.

With the photogrammetric techniques described above, it is possible to determine the ground coordinates and height of any object in the oblique image. However, as mentioned, calibration of low-oblique photographs requires at least one surveyed reference stake. While the height and ground coordinate information may be readily derived from oblique photographs without the aid of an array of many reference stakes, such an array may prove useful for other reasons when measuring surf zone phenomena photographically; for example:

- The stakes enable direct calibration of swash motion along the beach face.
- An array of stakes provides multiple control points for photo calibration and development of time series at fixed locations.
- Lines of reference stakes that cross the surf zone and are orthogonal to the mean shoreline define the onshore-offshore transects when oblique viewing angles are used.

This last point was important for the Coyote Point field measurements. During the Coyote Point experiment, the camera was positioned at an oblique angle to the surveyed reference transects crossing the beach face (Figure 7). With such a configuration, it is necessary to use a line of reference stakes to define the transect perpendicular to the shoreline. Run-up time series were developed at four transects along the beach for the Coyote Point experiment. As the distance between the

camera and the reference transect increased, it became increasingly difficult to identify the location of the moving shoreline along a single onshore-offshore transect without the aid of a line of reference stakes appearing in the oblique image. Large errors might be incurred in consistently identifying the run-up along the same single line perpendicular to the shoreline if reference stakes were not used.

Determination of the shoreline position along a straight line perpendicular to the shoreline is less difficult if the camera is aimed more directly offshore with the camera lens axis aligned nearly parallel with the reference stake transect, as in the Alameda experiment. The primary disadvantage of this viewing angle is that some resolution is lost in the onshore-offshore direction, and the observation of run-up along the shoreline is restricted. The oblique viewing angle optimizes the resolution of interstake run-up calibration and permits alongshore observation of the run-up. An oblique viewing angle relative to the reference stake transect and closely spaced reference stakes are recommended for surf zone measurements.

4. Calibration of Incident Waves from Oblique Photo Coordinates

Calibration of the run-up measurements required resolution of swash motion parallel with the plane of the beach face. Calibration of the run-up from the oblique photo coordinates into physical units was accomplished directly due to the presence of a surveyed control datum, i.e., the beach face, visible in the photographs. However, the techniques used to calibrate the run-up time series could not be used to calibrate the incident-wave time series. The photogrammetric equations [Eq. (1) to (17)] allow calculation of ground coordinates and heights of objects or features appearing in the oblique image relative to a known stationary datum. The amplitude fluctuations of the incident waves, however, produce a fluctuating datum. Thus, it is not possible to directly calibrate the incident waves appearing in the oblique image to physical units relative to the unknown MSWL.

The surveyed offshore reference stakes provided the necessary datum control to allow calibration of incident-wave time series at those locations. The incident-wave time series were derived from digitized time series of the water surface amplitude fluctuations measured at the reference stake in the oblique image. Only the elevations of the top and bottom of the reference stakes were measured during the field surveys. No height calibrations were available for the middle of the unmarked reference stakes, near the mean water level, where the waves passed the reference stakes. If the offshore reference stakes had been marked to indicate increments in their length, direct calibration of the incident-wave time series from the oblique photo coordinates to physical units might have been possible, providing the calibration marks were clearly visible in the photographs. Although perhaps more straightforward, providing calibration lines on each reference stake is time-consuming and unnecessary; rather, the photogrammetric equations may be used to provide the required calibration of incident-wave time series at vertical reference stakes.

The field survey measurements provided distance and elevation data for the camera and all the reference stakes in the two-dimensional reference grid. All surveyed elevation measurements were made relative to a common fixed datum. Thus, the elevation of the top and bottom of all reference stakes was known relative to the camera. Additionally, the distance measured from the camera to each of the reference stakes was known. Eq. (1) to (16) permit calculation of the real ground coordinates of objects appearing in the oblique image relative to a Cartesian coordinate system with origin at the camera. The only data required for the calculations are the camera focal length (f_c) and the height of the camera above the datum.

If a standard 50-mm lens, focused to infinity, is used for the photographic measurements, the focal length is known with sufficient accuracy. Since an infinitely adjustable telescopic lens was used on the 16-mm movie camera, however, it was necessary to first compute accurately the camera's focal length.

A computer program was written to work backward through Eq. (1) to (17) in order to compute the focal length. The tops and bottoms of reference stakes appearing in the oblique image were digitized. These oblique photo coordinates were input to the program, and the real ground coordinates and heights of the reference stakes were computed for different values of f_c. Since the measured height of these stakes and actual ground distances measured from the camera were known, f_c could be computed directly by using an error-minimizing iterative procedure. This process was repeated for many stakes appearing in the oblique image throughout the grid of reference stakes. The program simultaneously provided both the best estimate of f_c and a measure of the accuracy of height and distance measurements derived using Eq. (1) to (17) and the 16-mm Coyote Point data set. (If the camera is moved to a different viewing position and refocused, a new value for f_c must be derived.) The distance and height estimates computed using the program were compared directly with the actual values measured in the field during the experiments. The computed distance measurements agreed with those measured in the field to better than 1.3%. The computed heights agreed to within 4.5%. These accuracies are within the expected order of magnitude reported by Maresca and Seibel (1976) based on the larger, higher-resolution 35-mm photographic image.

Since the water surface is fluctuating, it cannot be used as a datum for the height measurements. However, the tops of the offshore reference stakes are stationary and clearly visible in the photographs, and their elevations are known with respect to both the camera and the absolute reference datum for the survey. For these reasons, the tops of the offshore reference stakes provided the requisite fixed datum for calibration of the incident-wave amplitude time series. For each incident-wave time series developed for an offshore reference stake, the top of that reference stake provided the local datum for the measurement. The top of each incident-wave reference stake was digitized in addition to the other parameters necessary to define the principal plane diagram (Figure 13).

The intersection of the free water surface with the reference stake was digitized in the same frames as was the run-up, and therefore the sampling rate was the same for both the run-up and the incident waves. Each frame of the movie film provided one time series point for both the run-up at any of the transects and the incident waves at any of the offshore reference stakes. Furthermore, the incident waves and run-up were digitized from the same individual movie frames over the entire roll of film. All of the resulting time series are thus time-registered.

Another computer program was written using Eq. (1) to (17) to calibrate the incident-wave amplitude time series into physical units measured relative to the top of the reference stakes. The incident-wave surface amplitude time series were calibrated with respect to the tops of the individual reference stakes. Subsequently, the incident-wave time series were calibrated into centimeters relative to the MSWL and output to a disk file for further processing by other analysis programs. The calibration program also computed the real ground coordinates and distances to the reference stakes. The computed distances agreed with the distances measured in the field to better than the 1.3% observed in the analysis to compute the camera focal length, f_c.

The mean of the measured and calibrated incident-wave time series was assumed to provide a reasonable estimate of the MSWL. Although this study is only concerned with the wave heights measured relative to the top of the reference stakes, the height computed using Eq. (17) is an absolute height. The assumption of equivalence between the mean of the incident-wave time series computed from the data and the MSWL provides an estimate of the MSWL. Any difference between the unknown, actual MSWL and the MSWL estimated from the incident-wave time series results in a small positive bias that is ultimately removed during the spectral analysis and does not affect the spectral estimates of the incident-wave conditions. This small bias does affect the estimate of the mean still water depth. The magnitude of this bias has not been estimated but is assumed to be small and within the limits of accuracy expected for this measurement technique.

C. Time Series Analysis

Using the photogrammetric analysis techniques and the calibration procedures discussed above, calibrated incident-wave and run-up time series were produced. Spectral analysis techniques were used to identify the frequency distributions of the energy in these time series. Additionally, the onshore-offshore and alongshore correlation analysis between measurement points required that the coherence and phase between time series be computed. Also of interest in this study was the slope of the run-up frequency spectrum over a particular frequency bandwidth. Software was developed to compute these statistical quantities and the spectral slopes. Standard stochastic data analysis methods, such as described by Bendat and Piersol (1971) or Otnes and Enochson (1978) were employed, and the basic equations are summarized here for completeness and to define variables that will appear in the following illustrations and discussions.

1. Spectral Analysis

The frequency decomposition of a time series can be used to detect inherent periodic fluctuations. If x(t) is the time series of a stationary random variable, then following Bendat and Piersol (1971), the autocorrelation function of x(t) is:

$$R_x(\tau) = E[x_k(t)x_k(t+\tau)] \tag{18}$$

where E [ ] indicates the expected or mean value, t is time, and τ is the time lag. $R_x(\tau)$ simply describes the dependence of the data values at a given time with the values at another time. The two-sided spectral density function, S(f), is the Fourier Transform of the autocorrelation function of x(t):

$$S_x(f) = \int_{-\infty}^{\infty} R_x(\tau)\exp(-j2\pi f\tau)d\tau \tag{19}$$

where f is frequency. The one-sided power spectral density function was computed for the amplitude measurements reported here and is given by:

$$G_x(f) = 2S_x(f) \tag{20}$$

where

$$0 \leqq f \leqq \infty \quad .$$

For a zero mean process, the variance σ^2 is given by:

$$S_x(f) = \sigma^2(f) \tag{21}$$

and

$$\int_{-\infty}^{\infty} S_x(f)df = E[(x(t)-\mu_x)^2] = \sigma_x^2 \quad , \tag{22}$$

which is Parseval's Rule of power conservation.

Fast Fourier Transform (FFT) techniques were used to compute the power spectrum given by Eq. (20). Parseval's Rule was checked in the code to verify that the power in the original raw time series was conserved during the spectral analysis. In addition, the resultant power spectrum was integrated numerically from zero to the Nyquist frequency, and the resultant integrated variance was compared to the variance in the original calibrated raw time series.

Several different processing options were available in the spectral analysis program. All combinations of processing options were tested to identify the optimal algorithm for the spectral analysis. Parameters studied in these tests included: rectangular, Parzen, and Hanning windows; different FFT lengths; methods of detrending and debiasing the time series; different amounts of FFT overlap; and both frequency and time domain spectral smoothing. The selected processing algorithm optimized spectral resolution and the confidence in each spectral estimate based on the time scales of the incident waves and run-up measured during the field experiments.

The incident-wave and run-up spectra reported here were computed by first debiasing and detrending the entire raw calibrated time series. Subsequently, the data in each FFT subwindow were debiased and detrended. A normalized (no power loss) Hanning cosine window was applied to each debiased and detrended FFT subwindow prior to computing the FFT. The spectra were computed over the entire available time series record and were time-domain-smoothed by incoherent averaging; a 50% overlap of the individual FFT subwindows was used to reduce spectral leakage.

2. Coherence and Phase Analysis

A second set of equations similar to Eq. (18) through (22) may be defined for a second time series, y(t):

$$R_y(\tau) = E[y_k(t)y_k(t+\tau)] \tag{23}$$

$$S_y(f) = \int_{-\infty}^{\infty} R_y(\tau)\exp(-j2\pi f\tau)d\tau \tag{24}$$

$$G_y(f) = 2S_y(f) \qquad (0 \leq f \leq \infty) \quad . \tag{25}$$

The cross-correlation function may be derived and is given by:

$$R_{xy}(\tau) = E[x_k(t)y_k(t+\tau)] \quad , \tag{26}$$

and the two-sided cross spectral density is:

$$S_{xy}(f) = \int_{-\infty}^{\infty} R_{xy}(\tau)\exp(-j2\pi f\tau)d\tau \quad . \tag{27}$$

The one-sided cross spectral density function, $G_{xy}(f)$, is given by:

$$G_{xy}(f) = 2S_{xy}(f) = C_{xy}(f) - jQ_{xy}(f) \tag{28}$$

where $C_{xy}(f)$ is the co-spectrum, and $Q_{xy}(f)$ is the quad-spectrum. In frequency space, the linear correlation function is given by the coherence function:

$$\gamma^2_{xy}(f) = \frac{G_{xy}(f)^2}{G_x(f)\, G_y(f)} = \frac{S_{xy}(f)^2}{S_x(f)\, S_y(f)} \qquad (29)$$

where

$$0 \leq \sigma^2_{xy} \leq 1 \quad .$$

The data were debiased prior to computing the coherence. The phase function, $\phi_{xy}(f)$, indicates the phase relationship between x(t) and y(t) and is given by:

$$\phi_{xy}(f) = \arctan(Q_{xy}(f)/C_{xy}(f)) \quad . \qquad (30)$$

In the coherence and phase plots that appear in Section V, $\gamma^2_{xy}(f)$ and $\phi_{xy}(f)$ are plotted directly as a function of frequency, f.

3. Spectral Slopes

An algorithm was incorporated in the spectral analysis program to compute the slope of the spectrum over a user-selected frequency band. The logarithms of the frequency, f, and power spectral density values, G(f), were computed at each frequency bin across the full selected band. A least-squares linear regression analysis was used to compute the slope of log (f) versus log (G(f)). The resultant slope value and linear correlation coefficient were output, and the slope was drawn on the plots by the computer graphics program.

4. Cumulative Distribution Functions and Statistical Hypothesis Testing

Spectral analysis of the incident-wave and run-up data helps quantify their properties in the frequency domain. Additional information concerning the statistical properties of the data in the amplitude domain can be obtained by computing the probability density function (PDF) or the cumulative probability distribution function, often referred to as simply the cumulative distribution function (CDF). The CDF was computed for the incident-wave and run-up data reported here. The CDF quantifies the probability that the instantaneous value of x(t) is less than or equal to some value x. The CDF can be indicated by P(x) where:

$$P(x) = \text{Prob}\,[x(t) \leq x] = \int_{-\infty}^{\infty} p(\xi)\ d\xi \qquad (31)$$

following Bendat and Piersol (1971). In Eq. (31), $p(\xi)$ is the probability density function, which describes the probability that the data value will fall within some defined range at any given instant.

The CDF was not derived from the PDF in this instance but was computed directly by ordering the data values by magnitude from largest to smallest and computing the cumulative frequency in percent. The ordered values were then plotted directly against cumulative probability in percent.

Computing and plotting the CDF is useful for several reasons. Ordering the data and displaying the CDF allows certain conclusions to be made concerning the statistics of the data in the amplitude domain, which complements the frequency domain statistics derived from the spectral analysis. The empirical CDF computed from the data can also be compared to various model statistical distributions. If the empirical CDF matches a particular model distribution, certain statistical properties associated with the model distribution can be inferred to also apply to the empirical data.

Various papers in the open literature have suggested that particular standard statistical distribution function models may be used to describe the amplitude distribution of waves and run-up. As will be discussed in detail in Chapter VI, both normal (Gaussian) and Rayleigh distributions have been proposed as model statistical distributions for both waves and run-up. Engineering run-up models based on a particular model distribution may yield erroneous results if the statistical distribution model selected does not accurately describe the real run-up distribution. There appears to be dissension in the literature concerning the correct statistical distribution to describe the run-up, i.e., normal or Rayleigh. For that reason, the empirical CDFs computed from the incident-wave and run-up data recorded in the field were compared to both normal and Rayleigh distributions. The agreement between the empirical and model distributions was quantified using two standard statistical hypothesis tests.

The chi-square (X^2) and Kolmogorov-Smirnov (KS) goodness-of-fit tests were used to quantify the agreement between distributions. Both of these tests, described in many standard references [Bendat and Piersol (1971); Benjamin and Cornell (1970)], are nonparametric, or distribution-free, meaning that they do not require a priori knowledge of a specific distribution function for the original random variable.

The general procedure for a X^2 test requires the use of a statistic with approximately a X^2 distribution as the basis for measuring the discrepancy between the empirical PDF and the theoretical PDF. For the X^2 tests reported here, a (0,1) normal distribution, denoted $p_o(x)$, was used as the basis of comparison. A general formula for the normal probability distribution function is:

$$P(x) = (\sigma_x\sqrt{2\pi})^{-1} \int_{-\infty}^{\infty} \exp\left[\frac{(\xi-\mu_x)^2}{2\sigma_x^2}\right] d\xi \quad . \qquad (32)$$

The X^2 test is applied by first grouping the N data observations into K intervals, forming an empirical frequency histogram. The number of data points falling into the i^{th} interval is the observed frequency, f_i, and the expected frequency, F_i, is the number of points expected to fall into the i^{th} interval if the true PDF of x(t) were $p_o(x)$. Following Bendat and Piersol (1971), the observed and expected frequencies of observation can be compared, and their difference is given by f_i-F_i. The X^2 sample statistic is then computed by summing the squares of the discrepancies in each interval, i, where:

$$X^2 = \sum_{i=1}^{N} \frac{(f_i-F_i)}{F_i} \quad . \qquad (33)$$

The number of degrees of freedom (DF) is equal to K-n, where n is the number of independent linear restrictions imposed on the observations.

For the normal distribution tested here using the X^2 test, the DF = K-3, since two constraints, the mean and variance, must be computed; the third restriction is due to the fact that once the frequencies in the K-1 intervals are known, the frequency in the last interval is also known.

The following hypotheses were formulated for the X^2 test:

H_0: Null hypothesis - data are normally distributed.

H_1: Alternate hypothesis - data are not normally distributed.

The data were grouped, the expected and observed frequencies were computed, and X^2 was computed based on Eq. (32). Any deviation of $p(x)$ from $p_o(x)$ results in an increase in X^2. Finally, X^2 was compared with tabulated critical values of $X^2(DF,\alpha)$, where α is the level of signficance and DF is the number of degrees of freedom. If $X^2 \leq X^2(DF, \alpha)$, the null hypothesis is accepted at the α level of significance, the $1-\alpha$ confidence interval. The run-up data were tested using the X^2 test at the 95% confidence interval, i.e., the 5% signficance level.

The same basic approach was used for the KS test. Both the Rayleigh and normal distributions were tested against the empirical distributions using the KS test. The empirical CDF was tested against the normal distribution function Eq. (32) and against a Rayleigh distribution function given by:

$$P(x) = 1-\exp\left[\frac{-Nx_i^2}{\sum_{i=1}^{N}(x_i^2)}\right] \qquad (34)$$

where N is the number of samples. The hypotheses H_0 and H_1 were formulated for both normal and Rayleigh distributions, and the deviations between the model CDF and the empirical CDF were measured. For the KS test, the maximum deviation was compared against the KS critical value, C, extracted from Table 4. If the maximum measured deviation is less than C, then H_0 is accepted; if the deviation is greater than C, then H_0 is rejected and H_1 accepted. The KS test was also conducted at the 95% confidence interval.

Table 4

CRITICAL STATISTIC, C, FOR THE
KOLMOGOROV-SMIRNOV GOODNESS-OF-FIT TEST*

Sample Size	$\alpha = 0.10$	$\alpha = 0.05$	$\alpha = 0.01$
5	0.51	0.56	0.67
10	0.37	0.41	0.49
15	0.30	0.34	0.40
20	0.26	0.29	0.35
25	0.24	0.26	0.32
30	0.22	0.24	0.29
40	0.19	0.21	0.25
Large N	$1.22/\sqrt{N}$	$1.36/\sqrt{N}$	$1.63/\sqrt{N}$

*Source: Benjamin and Cornell (1970)

α= level of significance

The data do not have to be grouped into bins or intervals for the KS test as for the X^2 test. The X^2 test can be sensitive to bin size, which is one drawback to this test. As shown in Table 4, C is inversely proportional to $\sqrt{N}$, where N is the number of sample points. If N is very large, the KS test may fail even if the empirical and theoretical distribution functions are very closely matched. As with any statistical test, the KS and X^2 tests must be used carefully, since outlying data points can cause the test to fail, as can too many data points or incorrect interval size.

V RESULTS

All incident-wave and run-up time series data computed from the Alameda and Coyote Point photographs were processed identically using the software and processing algorithms described in Section IV. Four primary categories of processing were identified, including spectral analysis, coherence and phase analysis, computation of spectral slopes, and statistical hypothesis testing on the CDFs. These results for both beaches are presented in this section.

A. Alameda Beach

Figure 3 shows the location of the stakes in the reference transect and the orientation of the camera relative to the reference stake transect. Using the methods summarized in Section IV, time series were developed for the incident waves recorded at reference stake 19 and for the run-up on the beach face.

1. Time Series and Spectra

The raw time series data were recorded at 10.66 Hz and were subsequently down-sampled to 5.33 Hz during the digitizing process. The entire roll of film was digitized. A total of 1024 time series points were processed for both the incident waves and run-up, representing approximately 192 s of data. A 128-point FFT window was used, which corresponded to a 24-s time series segment, giving a Nyquist frequency of 2.67 Hz and a spectral resolution of 0.042 Hz. The use of a 50% spectral overlap with the power-normalized Hanning window produced 26 equivalent degrees of freedom for the spectral estimates (Welch, 1967).

Figure 14 shows the time series of (a) the incident waves recorded at reference stake 19 and (b) the run-up recorded on the beach face. Recall that the component of run-up measured parallel to the beach face (R_B in Figure 1) was computed here. The full calibrated time series

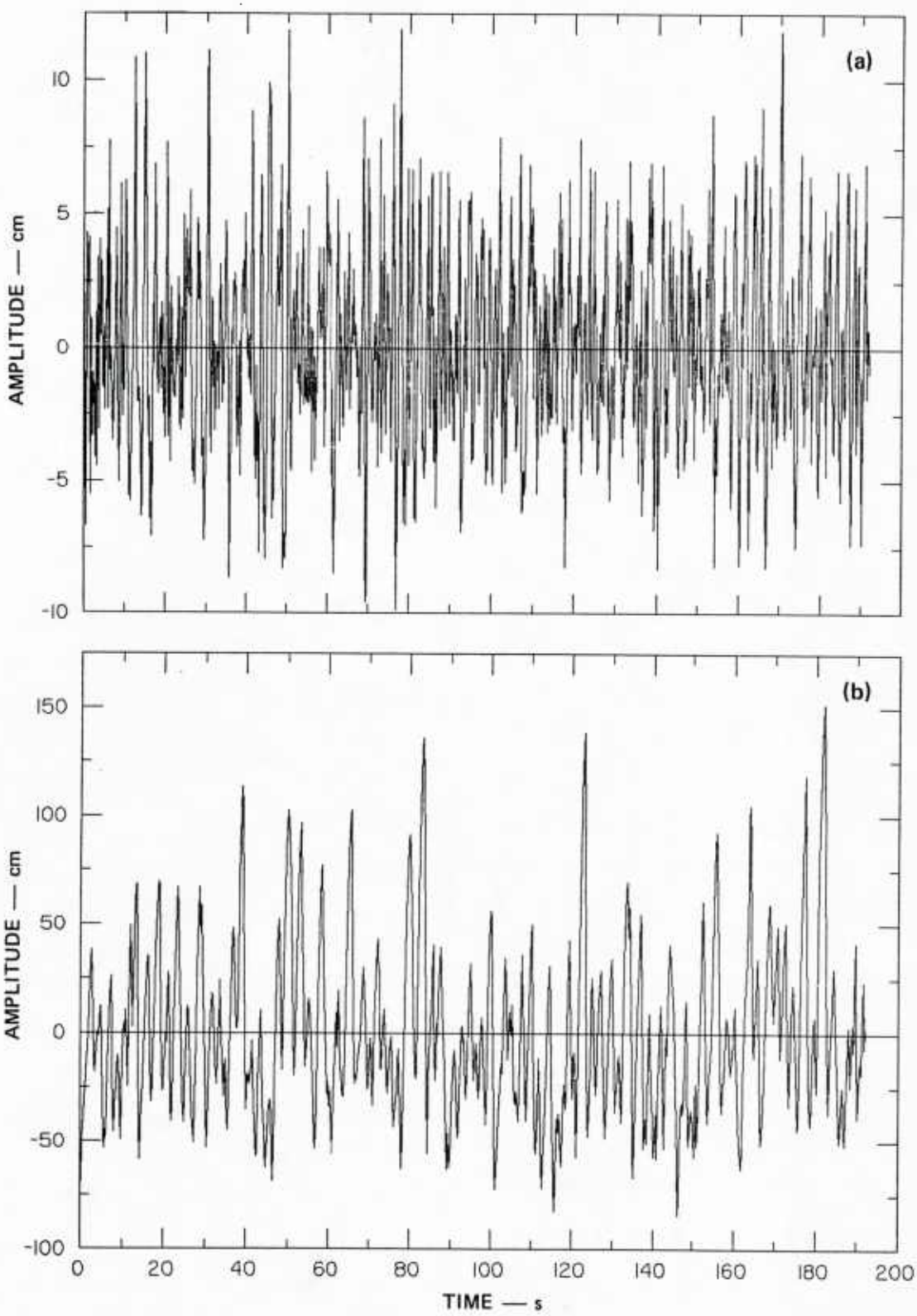

FIGURE 14 ALAMEDA BEACH (a) INCIDENT-WAVE AND (b) RUN-UP TIME SERIES

are shown in the figure with time plotted in seconds along the abscissa and amplitude plotted in centimeters along the ordinate. All time series plots presented henceforth will use this scaling format. Both time series have been debiased and detrended and are plotted with respect to their individual means.

The incident-wave amplitude time series is generally symmetric about its expected value, while the run-up time series shows positive run-up excursions greater in amplitude than the negative backwash excursions. Both time series are time-registered, and the lower frequency of the swash oscillations relative to the incident-wave oscillations is readily apparent, suggesting a red-shift in frequency should be observed between the incident-wave and run-up spectra.

This frequency shift is observed between the (a) incident-wave and (b) run-up spectra shown in Figure 15. The spectra illustrated in Figure 15 were computed from the time series of Figure 14. Each spectrum has been calibrated, and power spectral density (PSD) in centimeters squared/hertz is plotted as a function of frequency in hertz using linear scales. The predominance of low-frequency run-up spectral energy at frequencies not containing high energy densities in the incident-wave spectrum is striking. The absolute magnitude of the power in the run-up spectrum is greater than that of the incident-wave spectrum. As mentioned, the time series of swash motion in the plane of the beach face was recorded in these experiments. If the vertical component of run-up had been computed, the absolute magnitudes of the run-up PSD values would have been smaller, but the frequency distribution of the energy would remain the same.

The frequencies of the dominant peaks in the spectra are indicated in hertz next to the respective peak in the plots. The frequency resolution is 0.042 Hz, and the absolute position of any given peak with respect to frequency may vary by a single resolution cell in either direction. Thus, the 0.42-Hz peak in the wave spectrum matches the 0.37-Hz peak in the run-up spectrum. Guza and Thornton (1982) also report the presence of a large spectral peak in the run-up spectrum at the incident-wave

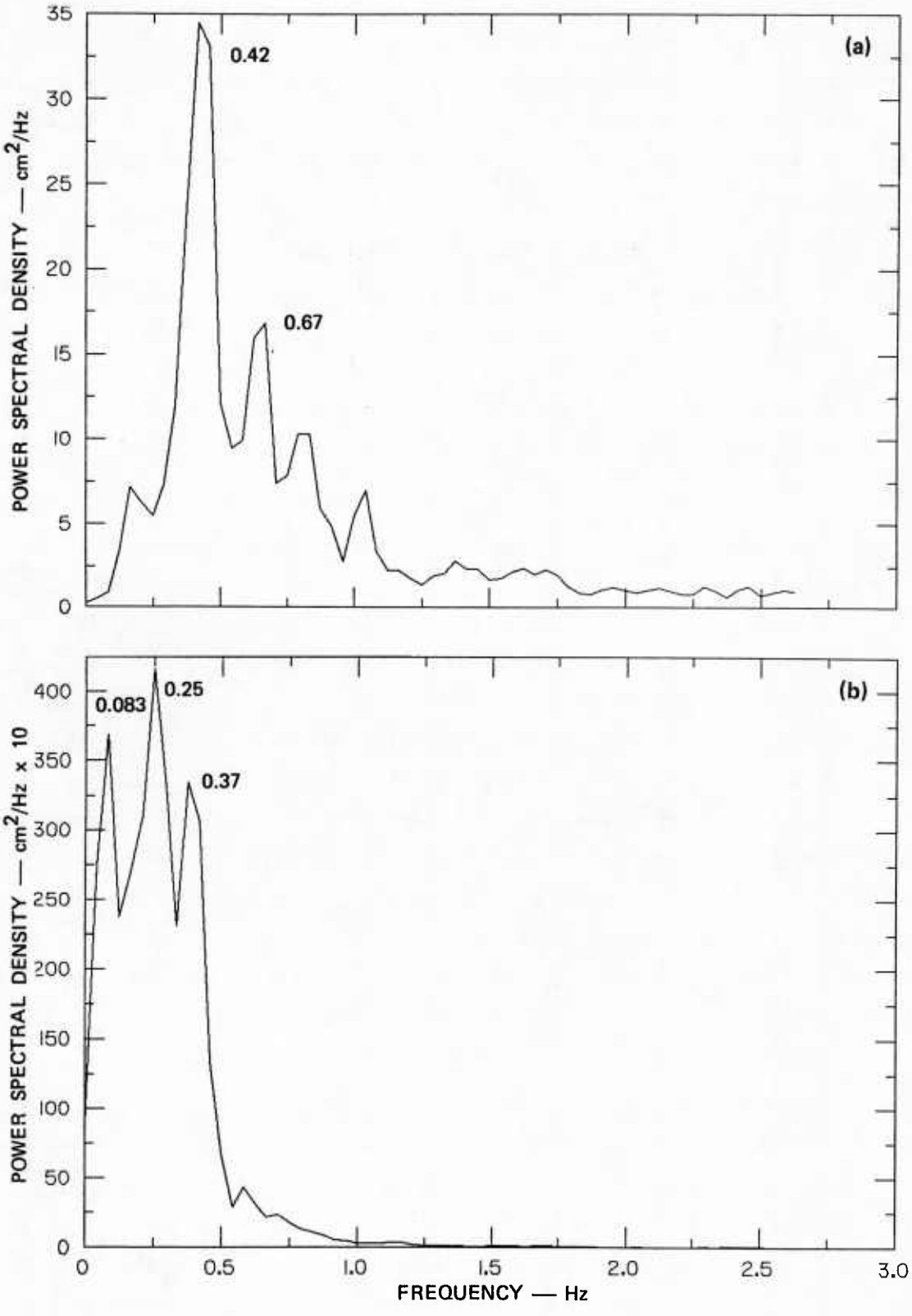

FIGURE 15 ALAMEDA BEACH (a) INCIDENT-WAVE SPECTRUM AND (b) RUN-UP SPECTRUM

frequency for run-up measured on steep beaches with narrow surf zones. The wave spectrum is virtually devoid of energy at the 0.083- and 0.25-Hz frequencies containing the majority of the energy in the run-up power spectrum. Conversely, the run-up spectrum does not exhibit energy at frequencies higher than about 0.5 Hz, whereas significant wave energy is present at frequencies greater than 0.5 Hz.

During the spectral processing the root-mean-square (rms) wave and run-up heights were computed both from the raw calibrated time series and by integrating the spectra from the first frequency bin to the Nyquist frequency. The values computed from the orginal time series agreed with those based on the spectral integration to better than 1%. The rms wave height computed for the Alameda data is 3.6 cm, and the rms run-up height is 39.0 cm.

2. Spectral Slope Analysis

The incident-wave and run-up spectra shown in Figure 15 were replotted in Figure 16 using a log-log format. The plots still show PSD in centimeters squared/hertz plotted as a function of frequency in hertz, and the 95% confidence interval in indicated. Spectral slopes were computed over the so-called saturation frequency band of the incident wind-wave spectrum. The slopes were computed by using a least-squares regression analysis (Section IV), and the best-fit line is shown on each plot. The slope computed for the (a) wave spectrum is -1.9 and for the (b) run-up spectrum is -3.2.

Huntley et al. (1977) (Appendix D) and Guza and Thornton (1982) computed spectral slopes from measurements made at beaches exposed to both swell and wind waves. Their incident-wave spectra showed a low-frequency roll-off, whereas the Alameda incident-wave spectrum contained only wind-wave energy, and the roll-off was actually more of a drop-off. The saturation frequency band was defined over the frequency band of the incident wind waves that broke near the shore (Section IV and Appendix D). Since the data recorded for the Alameda and Coyote Point field experiments contained only wind-wave characteristics, the saturation

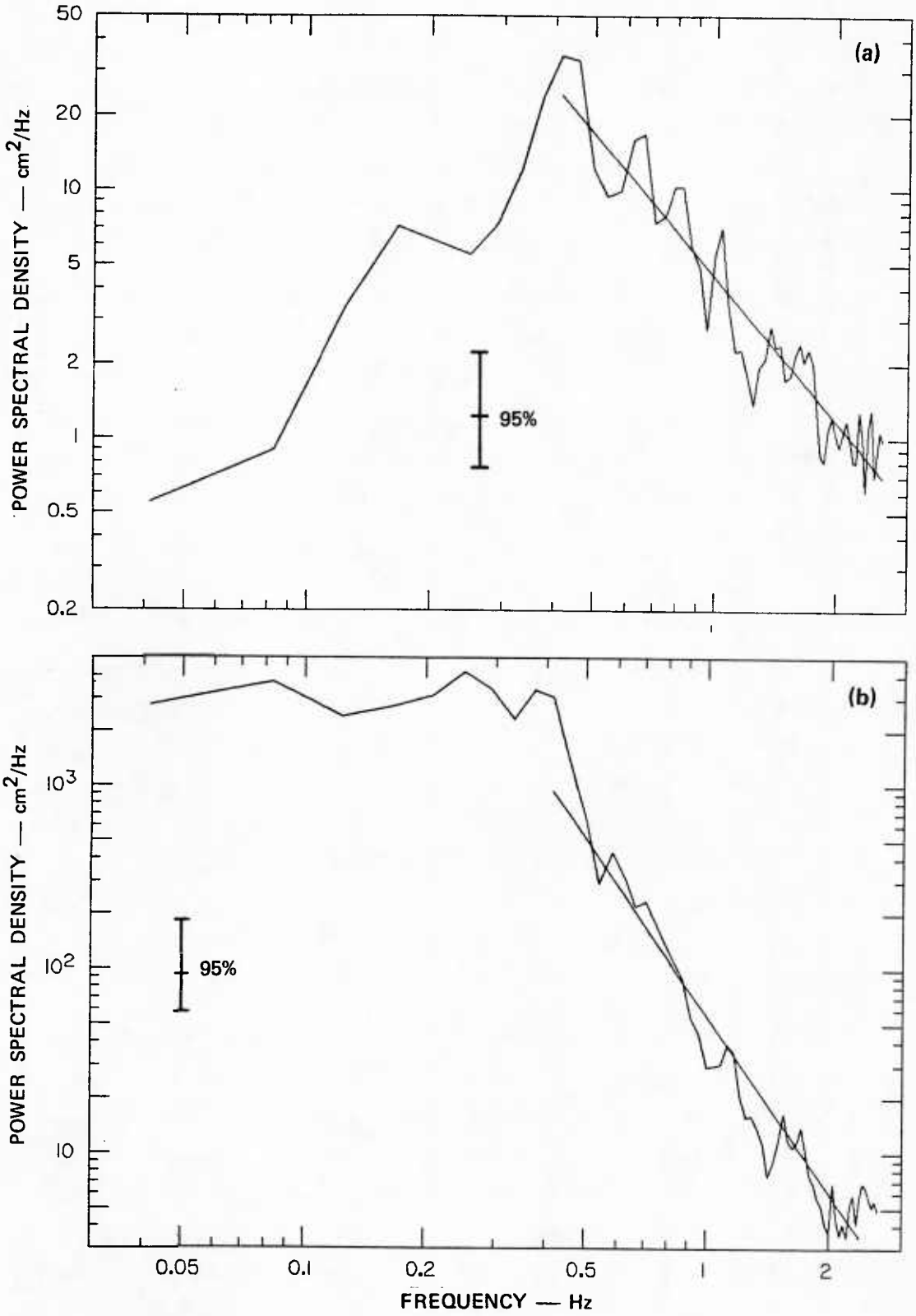

FIGURE 16 ALAMEDA BEACH (a) INCIDENT-WAVE SPECTRUM SHOWING -1.9 SLOPE AND (b) RUN-UP SPECTRUM SHOWING -3.2 SLOPE

region of the spectrum was defined here as all frequencies equal to and greater than the incident-wave peak frequency.

3. Correlation Analysis

Coherence and phase were computed between the incident-wave and run-up time series using the methods described in Section IV. Figure 17 shows (a) the coherence squared and (b) the phase in radians, both plotted as functions of frequency in hertz on log-linear scales. These plots may be compared directly with the energy distribution shown in the log-log scale spectral plots of Figure 16. Following Bendat and Piersol (1971), the 95% confidence limits are given in Table 5 as a function of coherence squared. At the 5% level of significance ($\alpha = 0.05$), the hypothesis that $\gamma_{xy} = 0$ results in an acceptance region for the variable equal to 0.19. Thus, if $\gamma_{xy} \geq 0.19$, the hypothesis that $\gamma_{xy} = 0$ must be rejected at the 95% confidence interval. That is to say that values of $\gamma_{xy} \geq 0.19$ are considered statistically significant at the 5% level of significance.

Table 5

THE 95% CONFIDENCE LIMITS FOR $\gamma^2(f)$ WHEN DF = 26

$\gamma^2(f)$	0.4	0.5	0.6	0.7	0.8	0.9
Upper limit	0.64	0.72	0.78	0.84	0.90	0.95
Lower limit	0.087	0.17	0.28	0.42	0.58	0.78

DF = Number of degrees of freedom.

The coherence is generally low across the entire frequency band, and the phase is random, indicating that the incident waves and run-up are generally not linearly correlated. This lack of linear coherence between the offshore incident waves and the run-up on the beach face is not surprising and has been observed by others. The relatively higher

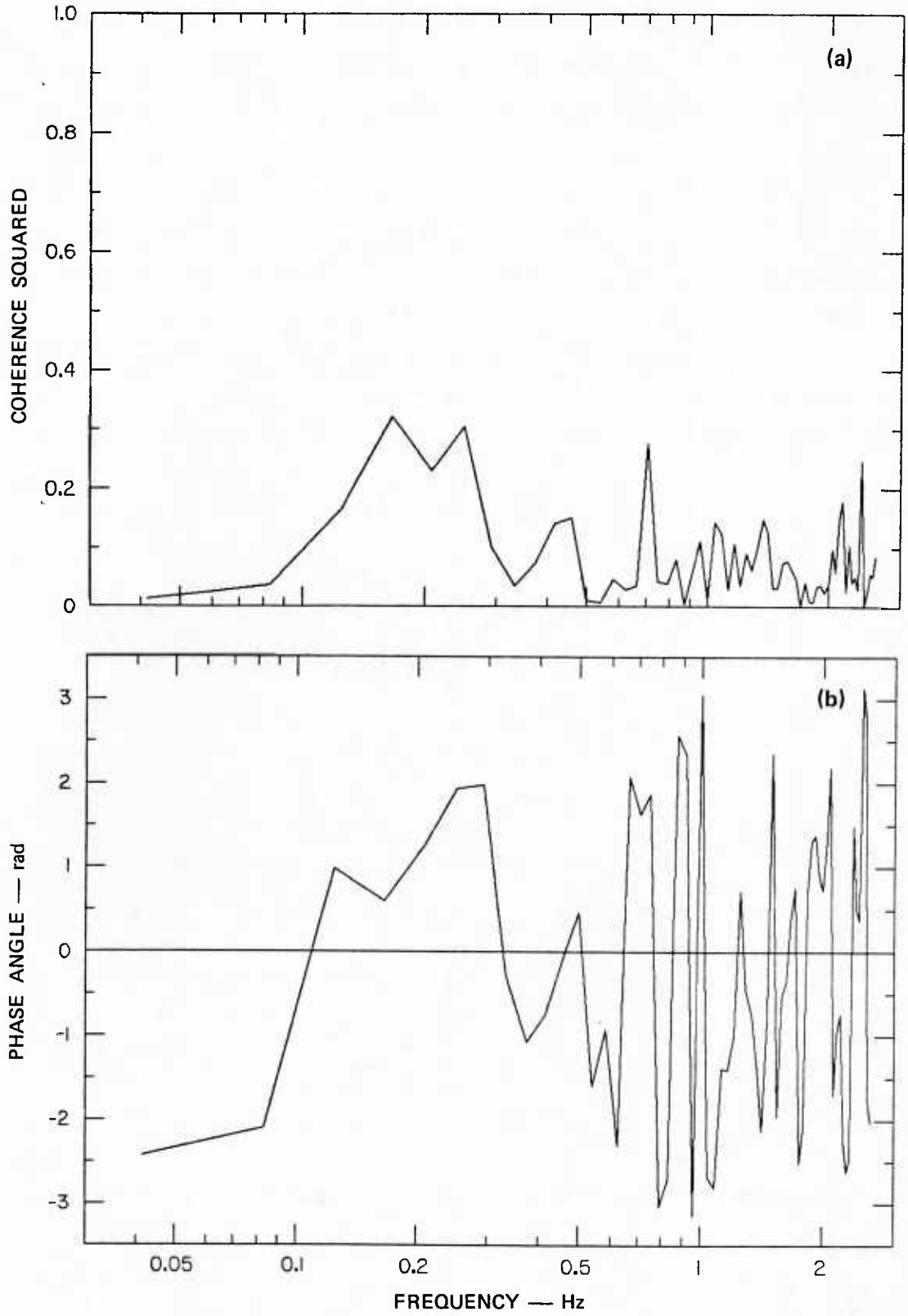

FIGURE 17 ALAMEDA BEACH (a) COHERENCE AND (b) PHASE BETWEEN THE INCIDENT WAVES MEASURED AT STAKE 19 AND THE RUN-UP ON THE BEACH FACE

levels of coherence at the lower frequency bands are based on few data points.

4. Cumulative Distributions

Using the techniques described in Section IV, the CDFs were computed for the Alameda incident waves and run-up. Two different data formats were used in comparing the empirical CDFs and the normal and Rayleigh CDFs. For hypothesis testing of the measured data with respect to the model normal distribution, the incident-wave and run-up amplitude time series were converted to time series of standard deviations, using:

$$x(t) = \frac{x(t) - E[x(t)]}{\sigma_x} \tag{35}$$

where E[ ] is the expected value and σ_x is the standard deviation. Figure 18 shows the CDF of the transformed time series of the (a) run-up and (b) incident waves compared to the standard normal CDF. Cumulative probability in percent is plotted as a function of the variable values computed using Eq. (35).

Figure 19 shows the (a) run-up and (b) incident-wave CDFs compared to the Rayleigh distribution. Because the Rayleigh distribution is defined for values greater than or equal to zero, a different data variable transformation was used. Prior to plotting the CDFs, the run-up and incident-wave time series were redefined using:

$$x(t) = x^2(t)/\langle x^2(t)\rangle \tag{36}$$

where

$$\langle x^2(t)\rangle = \left[\sum_{i=1}^{N} x_i^2\right]/N \quad .$$

The Rayleigh CDF is given in general terms by:

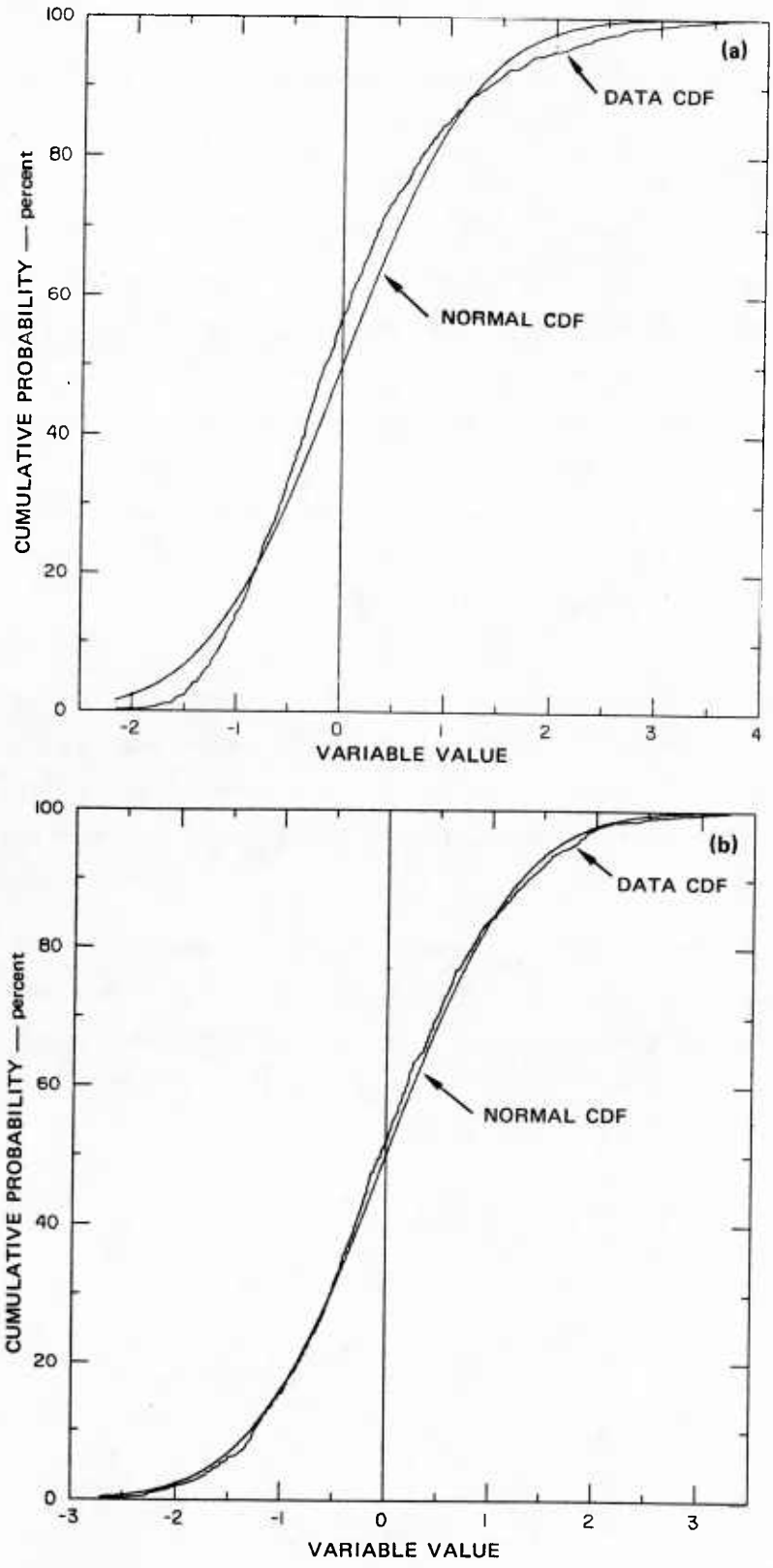

FIGURE 18 COMPARISON OF A NORMAL CDF AND CDFs COMPUTED FOR ALAMEDA BEACH (a) INCIDENT WAVES AND (b) RUN-UP

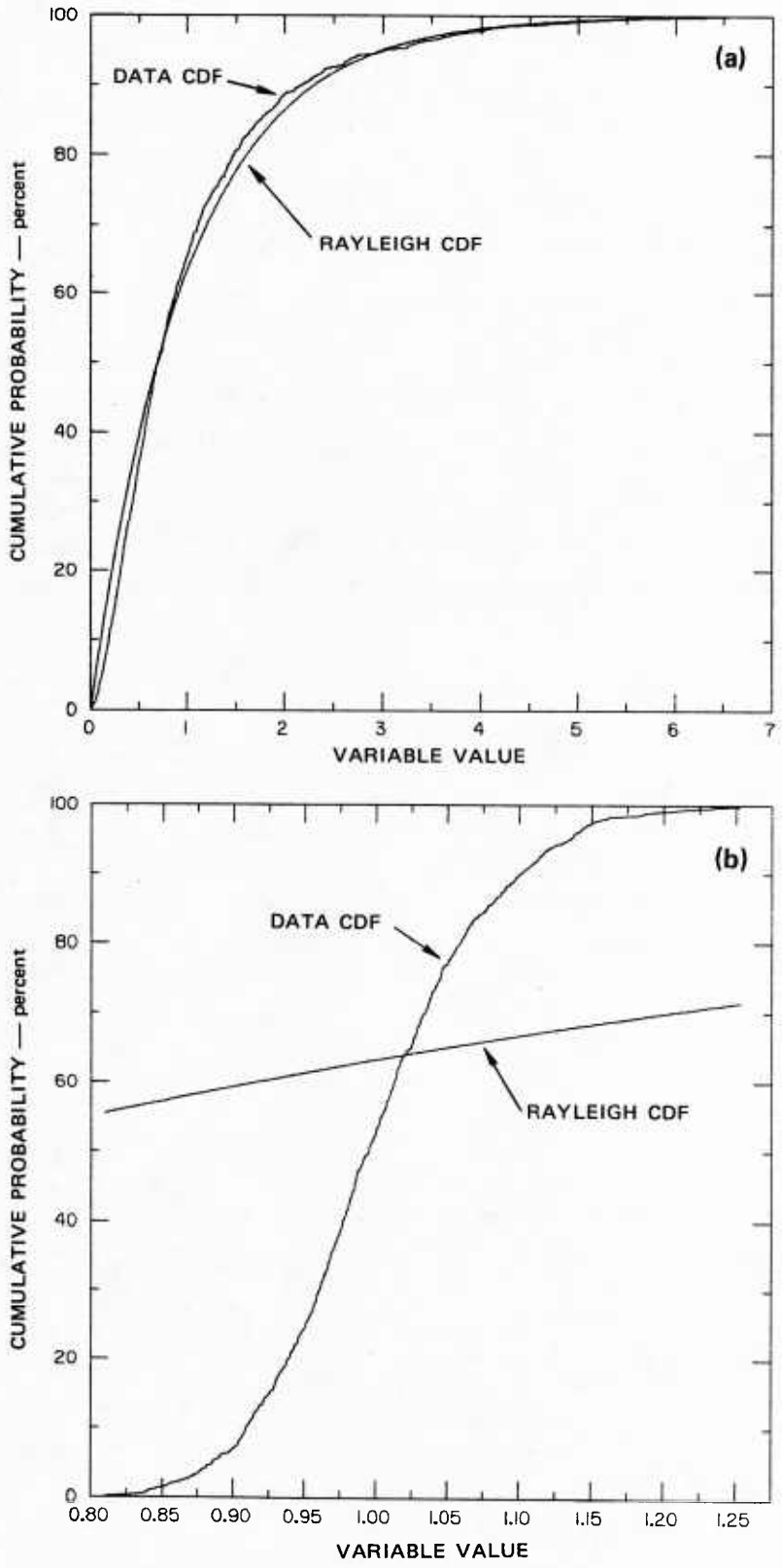

FIGURE 19 COMPARISON OF A RAYLEIGH CDF AND CDFs COMPUTED FOR ALAMEDA BEACH (a) INCIDENT WAVES AND (b) RUN-UP

$$\text{Prob}(x \leq X) = 1-\exp(x^2(t)/\langle x^2(t)\rangle) \quad . \qquad (37)$$

In Figure 19, the values of Eq. (36) and the Rayleigh distribution of Eq. (37) are plotted with the cumulative probability in percent.

With the exception of the Rayleigh distribution for the waves, the empirical distributions provide a very close fit to either the normal or Rayleigh model CDF, and it might be tempting to conclude that both distributions provide a good fit to the data. The KS statistical hypothesis test described in Section IV was used to quantify the quality of the fit between the empirical, normal, and Rayleigh distributions. The hypotheses H_0 and H_1 were formed for the KS test against the normal CDF:

H_0 = Null hypothesis - data are normally distributed

H_1 = Alternate hypothesis - data are not normally distributed.

Corresponding hypotheses H_0 and H_1 were identified for the Rayleigh distribution. The results of the KS hypothesis tests are summarized in Table 6, which shows the data and model types being compared. The null hypothesis, H_0, is accepted if $D < C$; otherwise, it is rejected and H_1 is accepted.

Table 6

KS TEST RESULTS FOR
ALAMEDA BEACH INCIDENT WAVES AND RUN-UP

Data	Model	N	C	D	Result
Run-up	Normal	1024	0.0425	0.0734	Reject H_0
Waves	Normal	1024	0.0425	0.0329	Accept H_0
Run-up	Rayleigh	1024	0.0425	0.0767	Reject H_0
Waves	Rayleigh	1024	0.0425	0.562	Reject H_0

N = Number of data points used in test.

C = KS test critical value.

D = Maximum difference between the theoretical and empirical CDFs.

Result: Accept H_0 if $D < C$; otherwise, reject H_0.

The null hypothesis, H_0, was rejected in three out of the four tests, and only the incident-wave CDF and normal CDF appeared to be statistically the same with respect to the KS test statistic critical value. That is, the two CDFs did not appear to be statistically different using the KS test statistic. It should be emphasized here that these statistical tests do not indicate the distribution to which the empirical data conform; rather, the tests identify the model statistical distributions from which the empirical data are not different statistically. The tests conducted on the Alameda data indicate that the distribution of amplitudes of the incident waves measured at stake 19 was statistically similar to a normal distribution and not a Rayleigh distribution. Although the hypotheses of a normal or Rayleigh run-up distribution were rejected y the tests, the differences were close to the critical statistic. The fit between the distributions was visually close in each case. It is also possible that some other statistical distribution, not tested here, may fit the empirical run-up and incident-wave distributions.

It is interesting to note the skew of the run-up CDF shown in Figure 18 relative to the more symmetrical distribution of the incident-wave CDF. Recall that this asymmetry was also observed in the run-up time series.

B. Coyote Point Beach

The location of the Coyote Point field site and the experimental reference stake array are shown in Figures 2, 6, and 7. The reference stakes were numbered consecutively from 1 to 15 in transect 1 (Figure 6) in the onshore-to-offshore direction. The incident waves were measured at four offshore locations, which included reference stakes 10 and 15 in transect 1 and points A and B in the offshore reference stake triangle shown in Figure 7. The run-up was measured along transects 1, 3, 5, and 6 (Figure 6), spanning an alongshore distance of approximately 3.5 m.

The 16-mm photographic time series was processed using the same methods described for the Alameda data, as detailed in Section IV. The Coyote Point incident-wave and run-up time series data were recorded at 14 Hz and were downsampled to 3.5 Hz during digitizing. All eight time series are time-registered.

Five rolls of film were recorded during the experiment, and the best of these was selected for analysis based on clarity and resolution of the run-up in the alongshore direction. All five rolls were reviewed frame by frame, and the roll selected for analysis was typical of the entire data set. Spectral analysis of these data was accomplished using a 36-s, 128-point FFT window, producing a spectral resolution of 0.0273 Hz and a Nyquist frequency of 1.75 Hz. The 50% spectral overlap, Hanning window, and other processing techniques described in Section IV were used.

1. Time Series and Spectra

Figure 20 shows the incident-wave time series recorded at offshore reference stakes A and B. Amplitude in centimeters is plotted with respect to time in seconds. Each time series is approximately 268 s in duration and is symmetric about its respective mean. Figure 21 shows the incident-wave time series recorded along transect 1 at reference stakes 15 and 10. Stake 10 was located nearer to the shoreline than stake 15. Each of these time series is about 256 s in length, and a decrease in wave amplitude is observed between stake 15 and stake 10 as the shoreline is approached. The waves were steepening or just beginning to break as they reached stake 15; the largest waves broke by plunging just seaward of stake 15, while the smaller waves broke by plunging just shoreward of stake 15. The waves measured at stake 10 were actually bores moving shoreward toward the beach, the waves having already broken in the vicinity of stake 15.

Figures 22 and 23 show the run-up time series recorded at reference transects 1 and 3 and at transects 5 and 6, respectively. The run-up time series have been debiased, and the absolute magnitude of the expected values for each of the time series agreed to within about 8%. Inspection of the four run-up time series reveals that the amplitude fluctuations are all basically of the same magnitude. Comparison of these run-up time series with the incident-wave time series shows that the frequency of oscillation is much lower for the run-up than for the waves. A low-

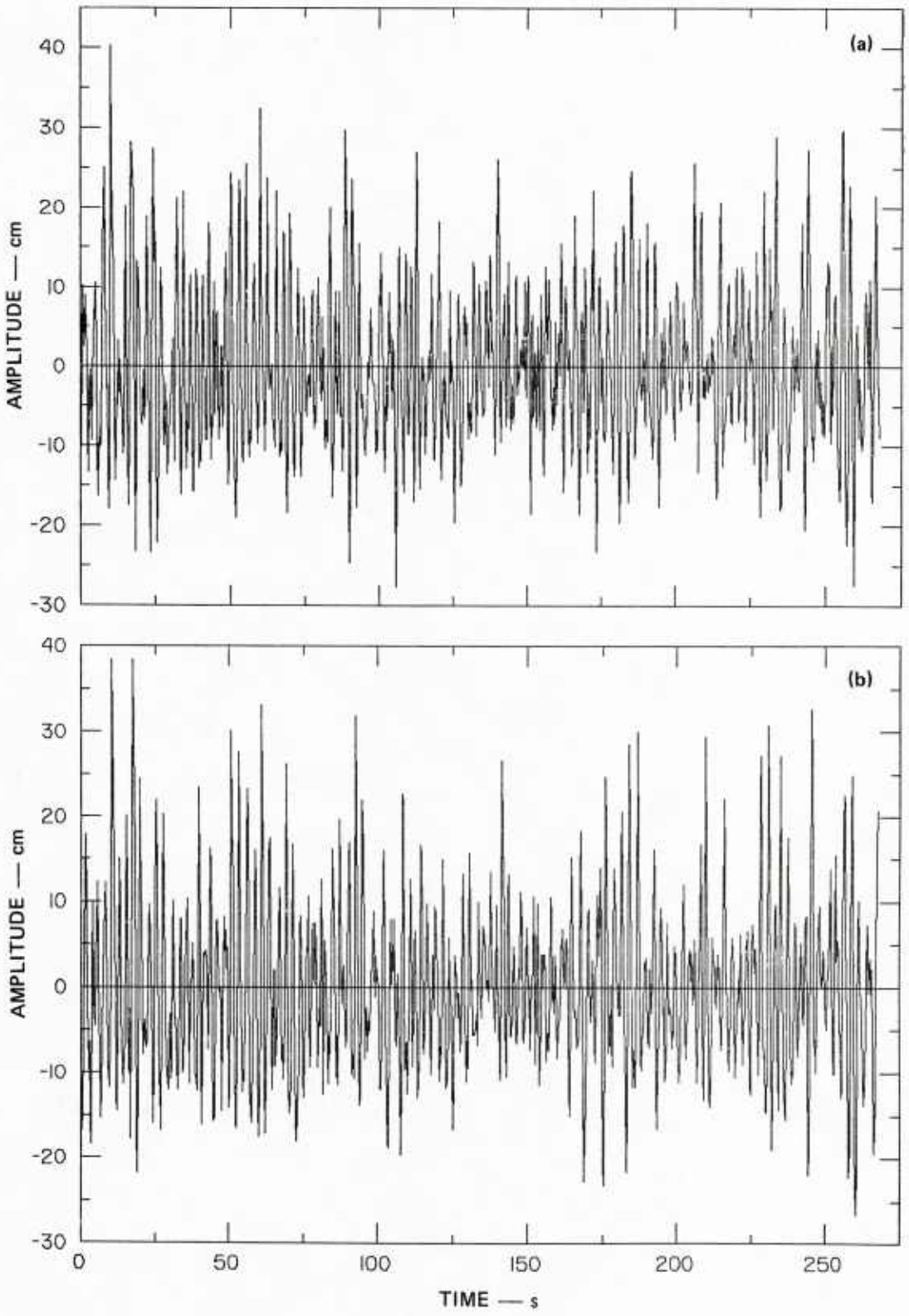

FIGURE 20 COYOTE POINT INCIDENT-WAVE TIME SERIES MEASURED AT (a) OFFSHORE REFERENCE STAKE B AND (b) OFFSHORE REFERENCE STAKE A

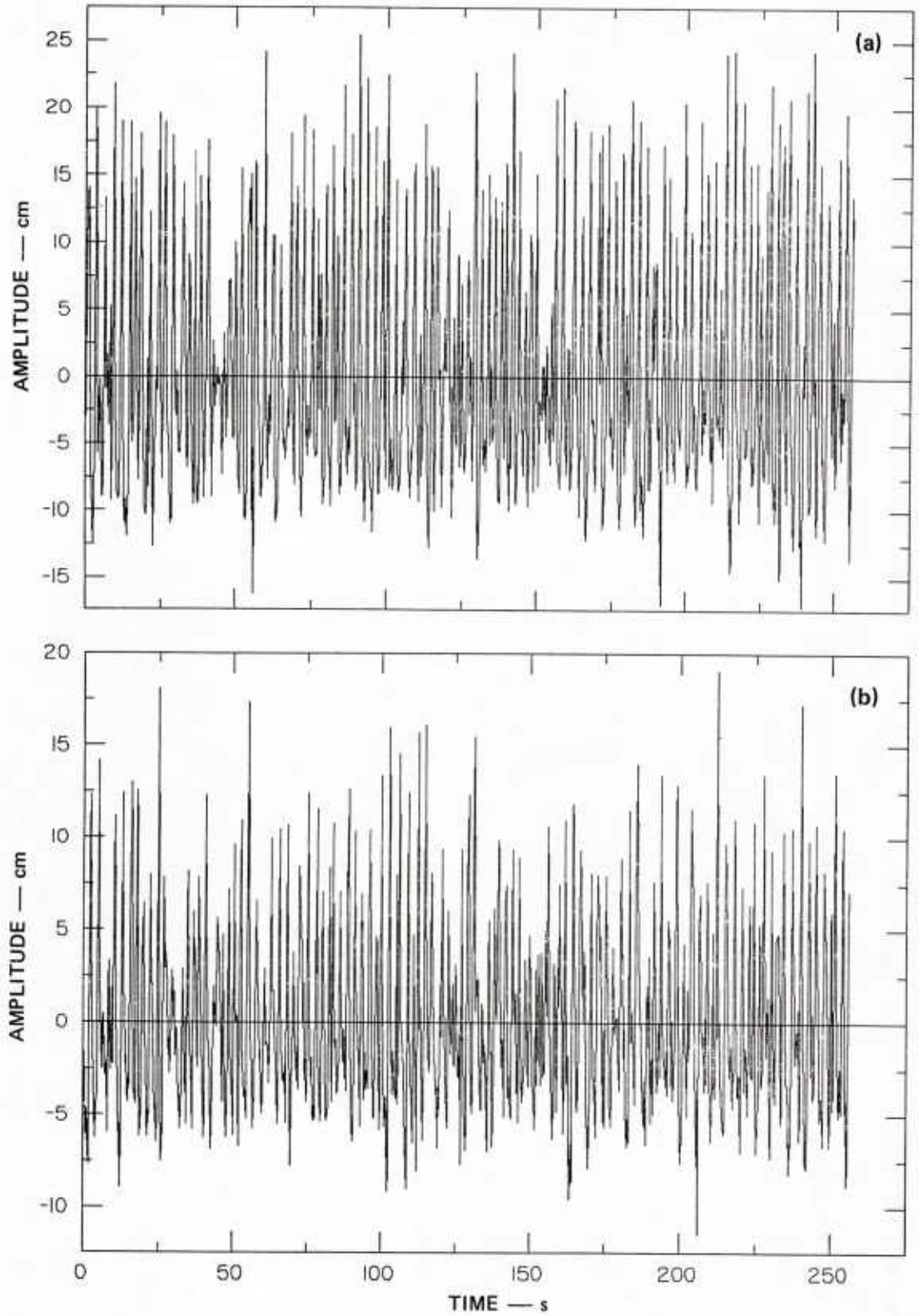

FIGURE 21 COYOTE POINT INCIDENT-WAVE TIME SERIES MEASURED AT (a) STAKE 15 AND (b) STAKE 10 IN REFERENCE TRANSECT 1

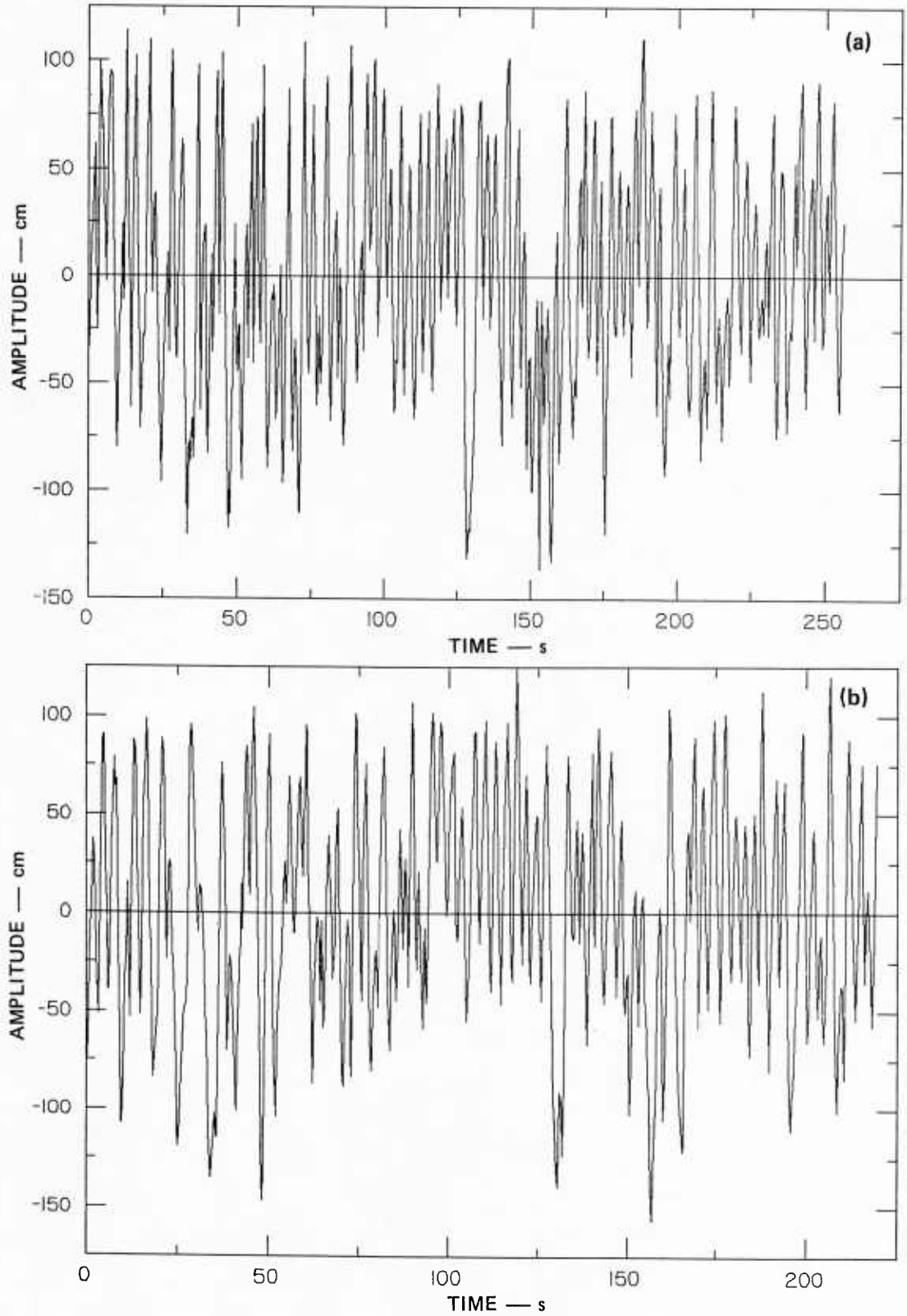

FIGURE 22 COYOTE POINT RUN-UP TIME SERIES MEASURED ALONG (a) TRANSECT 1 AND (b) TRANSECT 3

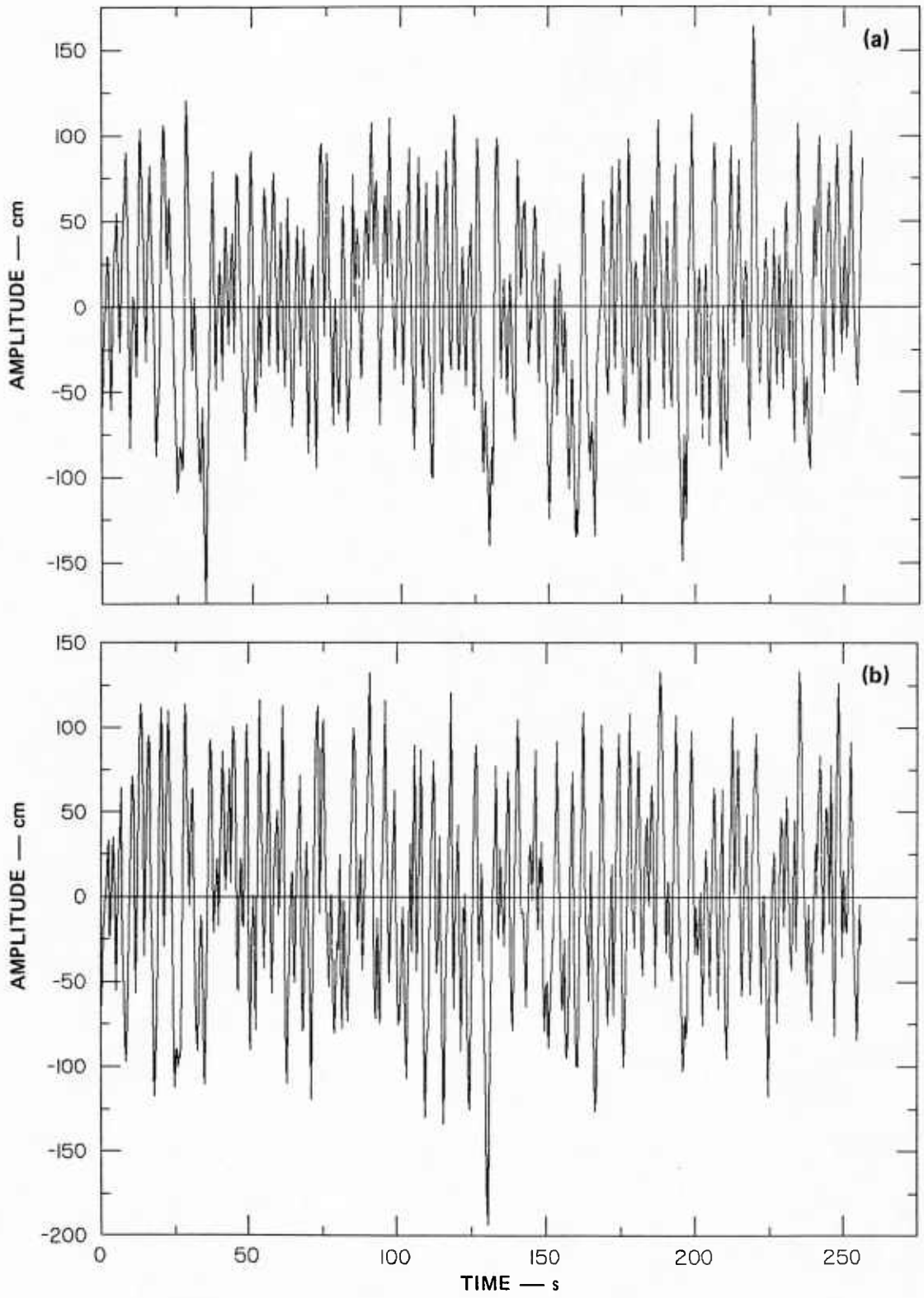

FIGURE 23 COYOTE POINT RUN-UP TIME SERIES MEASURED ALONG (a) TRANSECT 5 AND (b) TRANSECT 6

frequency modulation appears to be superimposed on the primary run-up wave form in each time series plot. These observations will be quantified by the spectra.

The spectra computed for the Coyote Point incident-wave and run-up time series are shown in Figures 24 to 27. Figure 24 shows the incident-wave spectra computed for the data recorded at offshore stakes B and A. Each plot shows PSD in centimeters squared/hertz plotted as a function of frequency in hertz. The frequencies of the most predominant spectral peaks are indicated in hertz on the plots. Figure 25 shows the incident-wave spectra measured along transect 1 at stakes 15 and 10. The spectral peak frequencies between all four of the incident-wave spectra agree to within 1 frequency resolution cell.

The incident-wave spectra measured at all four locations are uniformly narrow-band, with one primary frequency. Virtually no low-frequency energy is observed in any of the incident-wave spectra measured either well offshore at stakes A and B or nearer the shoreline at stakes 10 and 15. Stakes A and B were separated in distance by approximately 2 m, and the wave spectra computed for these locations are nearly identical, supporting the consistency of the analysis and data processing.

An expected net decrease in wave height is observed across the reference stakes moving shoreward in order B-A-15-10, as summarized in Table 7. The rms wave heights reported in Table 7 were computed both directly from the time series variance and by integration of the spectra across the full frequency band from zero to the Nyquist. Agreement between the two methods was uniformly better than 1%, thus verifying power conservation during the spectral processing and correct normalization of the Hanning window used to minmize spectral leakage. Some transfer of spectral energy from lower to higher frequencies is observed in the spectra computed for stakes 10 and 15. This observed energy transfer is common and has been observed by others (Thornton, 1979). Waves shoaling and breaking on a beach first become saturated at the peak energy density, and the energy is subsequently transferred from lower to higher frequencies. This is the opposite of the mechanism

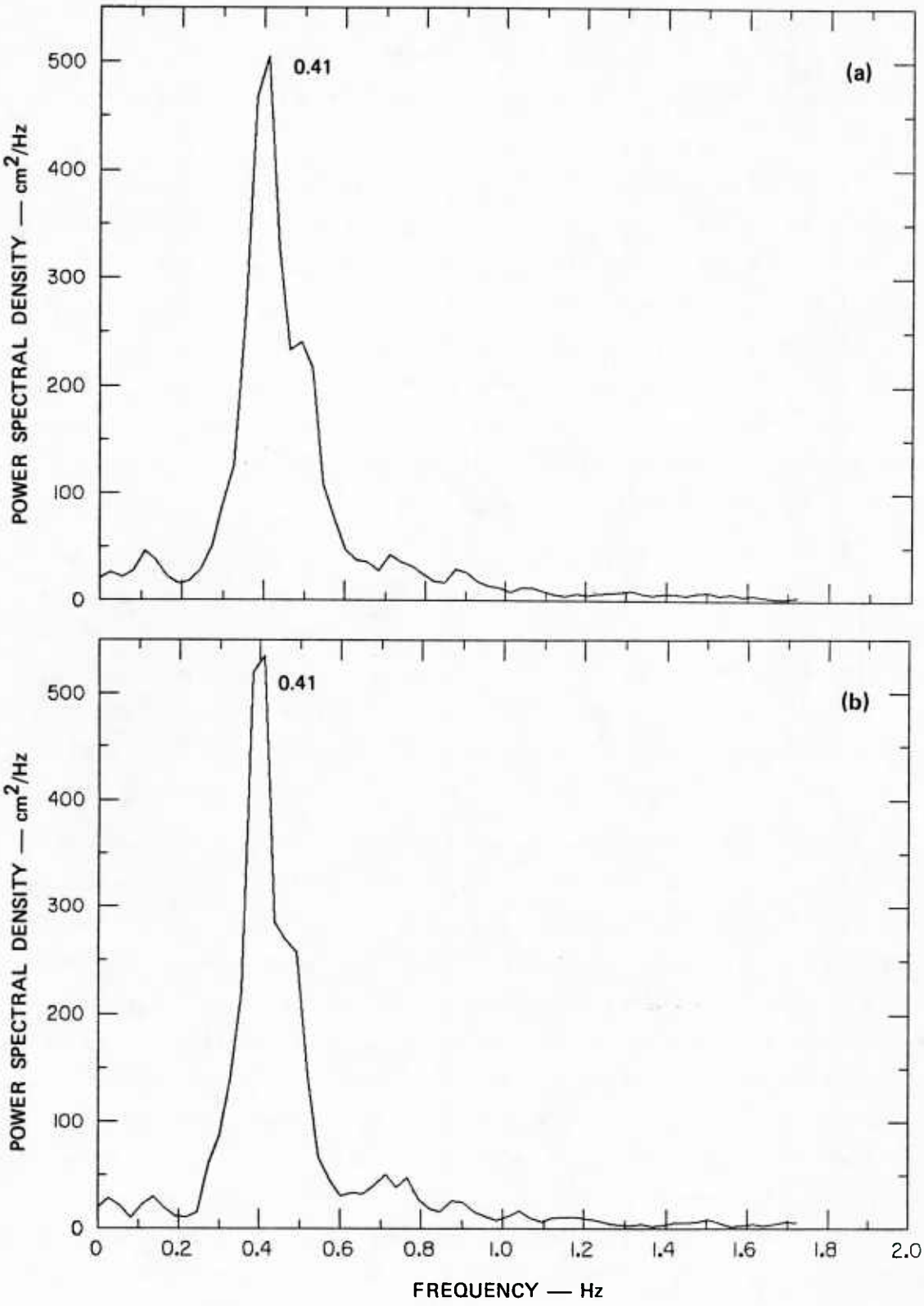

FIGURE 24 COYOTE POINT INCIDENT-WAVE SPECTRA MEASURED AT (a) OFFSHORE REFERENCE STAKE B AND (b) OFFSHORE REFERENCE STAKE A

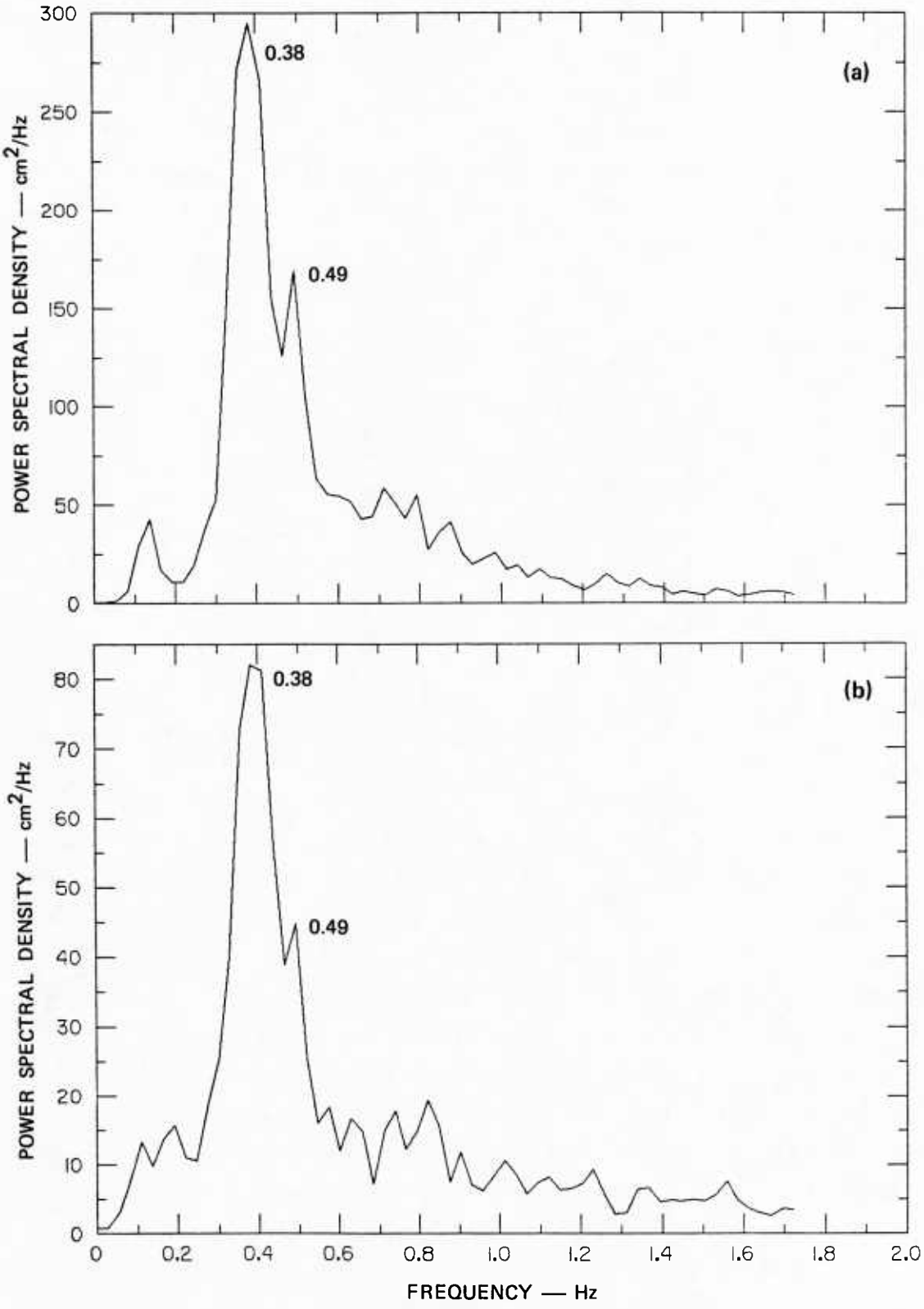

FIGURE 25 COYOTE POINT INCIDENT-WAVE SPECTRA MEASURED AT REFERENCE STAKES (a) 15 AND (b) 10 IN REFERENCE TRANSECT 1

controlling wave growth in deep water, where the energy is transferred from higher to lower frequencies. This behavior is not always observed in the surf zone and is controlled primarily by the energy density of the primary breaking-wave frequency. If the primary frequency is not completely saturated, the blue-shift energy transfer may be minimized or not observed at all.

Table 7

COYOTE POINT rms WAVE HEIGHTS (h_{rms})

Reference Stake Location	h_{rms} (cm)	DF
B	10.0	23
A	9.7	23
15	8.6	23
10	5.1	23

DF = equivalent degrees of freedom in spectral calculations.

The run-up spectra measured at reference transects 1 and 3 and at transects 5 and 6 are shown in Figures 26 and 27, respectively. The frequencies of the predominant peaks in each spectrum are marked on the plots, and each spectrum is plotted in the standard format of PSD as a function of frequency in hertz. The predominance of the low-frequency energy in each run-up spectrum is the most striking feature. Recall that the spectral peak frequency of the incident waves was located at approximately 0.38 Hz. The predominant run-up spectral energy is located at frequency bands much lower than 0.38 Hz, although each of the measured run-up spectra do show some energy at the incident-wave frequency. This relationship was also observed between the incident-wave and run-up spectra measured at Alameda Beach. The 0.14-Hz spectral peak is observed in all of the run-up spectra measured at Coyote Point. A peak at 0.22 to 0.25 Hz (1 resolution cell apart) is observed in the run-up spectra measured at transects 1, 3, and 5.

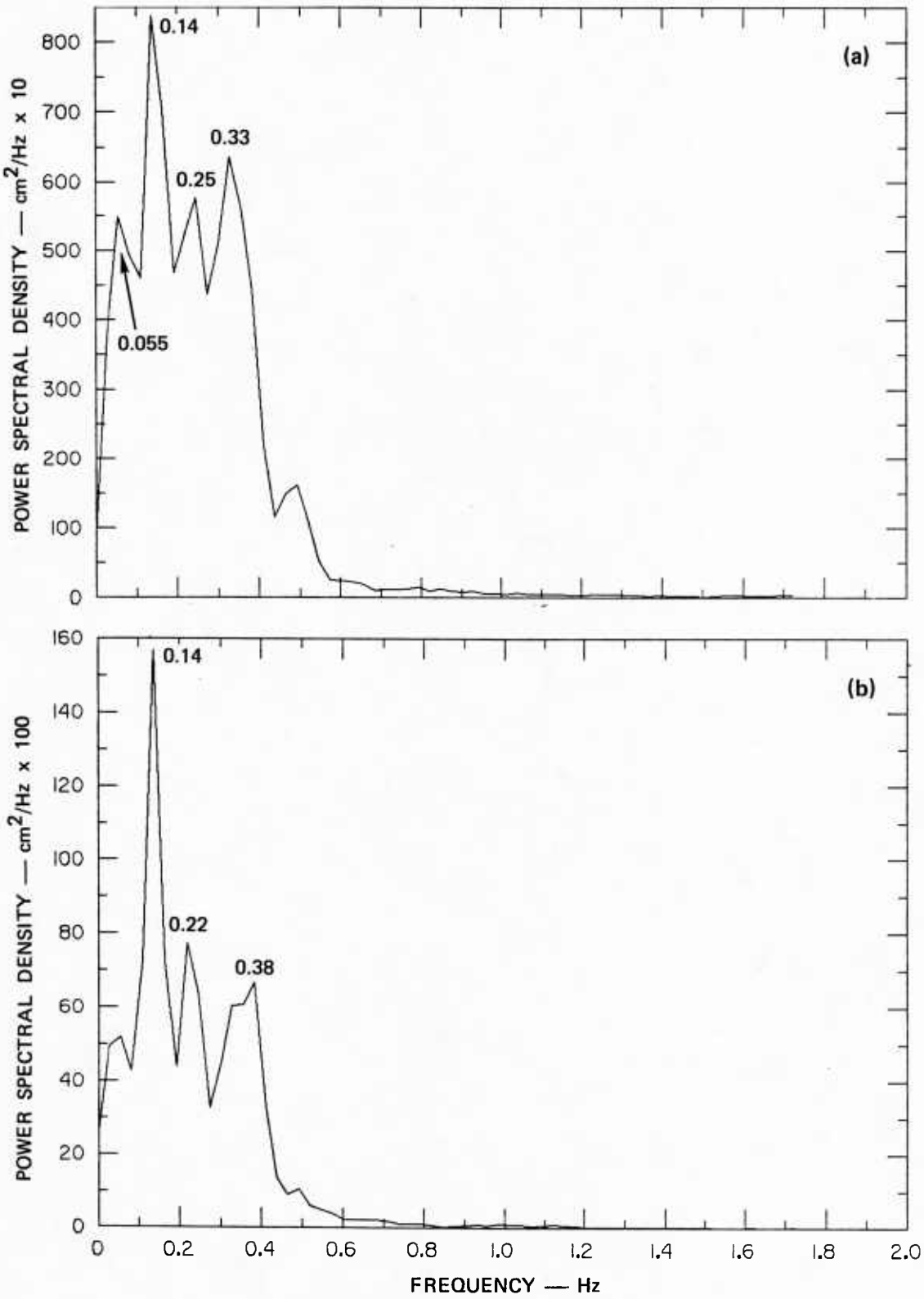

FIGURE 26 COYOTE POINT RUN-UP SPECTRA MEASURED ALONG (a) REFERENCE TRANSECT 1 AND (b) TRANSECT 3

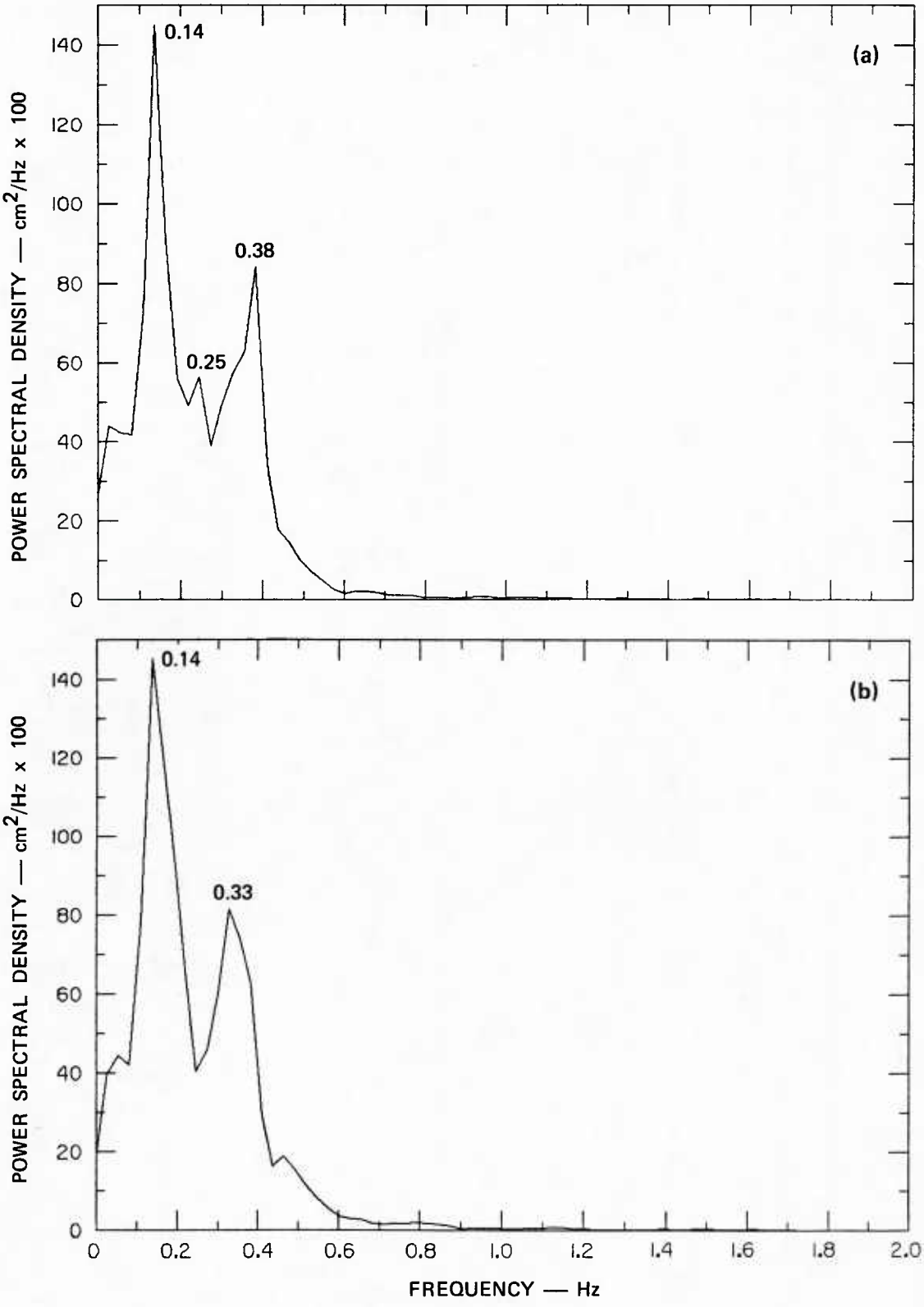

FIGURE 27 COYOTE POINT RUN-UP SPECTRA MEASURED ALONG (a) REFERENCE TRANSECT 5 AND (b) TRANSECT 6

Although the frequency resolution of all four run-up spectra is identical, there appears to be a loss of fine structure detail in the spectra moving from transect 1 to transect 6. This is attributed to the increasing distance of the measurement point from the camera location (Figure 7), coupled with the photographic resolution of the small 16-mm film. During analysis, it was increasingly difficult to observe the fine details of the swash motions on the beach face as transects further down the beach were analyzed. The predominant run-up and backwash motions at frequencies 0.14 and 0.38 Hz were readily observable along all of the transects analyzed here. The smaller-amplitude motions were not as easily identified further down the shore. For that reason, the continuum of energy located in frequency bands surrounding the dominant 0.14- and 0.38-Hz peaks in the run-up spectra recorded at transects 3, 5, and 6 is not as pronounced as in the spectrum recorded at transect 1. The basic shape of the energy continuum surrounding the 0.14-Hz spectral peak is conserved in the spectra measured at transects 1, 3, and 5.

The rms run-up height was computed at each of the four transects both from the calibrated time series and by spectral integration across the entire frequency band. Agreement was within the 1% observed for the incident waves. Table 8 shows the equivalent degrees of freedom for each run-up spectrum and the associated rms run-up height computed in the plane of the beach. The run-up excursions parallel to the beach face can be converted to vertical run-up by multiplication of the sine of the beach slope.

2. Spectral Slope Analysis

The spectral slopes were computed for the run-up and incident-wave data recorded at Coyote Point using the computational methods described in Section IV. The saturated frequency band for the spectral slope computations was defined in the same manner as for the Alameda data, i.e., the band of the breaking incident wind waves. The log-log format for the incident-wave spectra recorded at stakes B and A and stakes 15 and 10 is shown in Figures 28 and 29, respectively. The log-log run-up

Table 8

COYOTE POINT rms RUN-UP HEIGHTS (R_{rms})*

Reference Transect	R_{rms} (cm)	DF
1	50.3	23
3	55.2	20
5	53.4	23
6	55.7	23

*rms run-up height computed for the component of run-up parallel to the beach slope.

DF = equivalent degrees of freedom in the spectral calculations.

spectra are shown for transects 1 and 3 (Figure 30) and transects 5 and 6 (Figure 31).

The least-squares-fitted line is shown on each plot as computed and drawn by the graphics routine in the computer program. The slopes (Table 9) compare favorably with the slopes computed for the Alameda data and with spectral slopes reported in the open literature. The run-up spectrum measured at the Alameda Beach showed a slope of -3.2, and the Alameda wave spectrum had a -1.9 slope. All of the Coyote Point run-up spectral slopes are on the order of -3.0, which shows good agreement with slopes reported recently by Guza and Thornton (1982). The slopes of the incident-wave spectra decrease in the shoreward direction. This appears to be explained by the transfer of energy in the spectrum from lower to higher frequencies as the waves shoal and break. The spectral slopes measured in these field experiments will be discussed further in Section VI.

3. Correlation Analyses

The coherence and phase were computed for several of the time series pairs in the Coyote Point data set. Coherence and phase analyses were

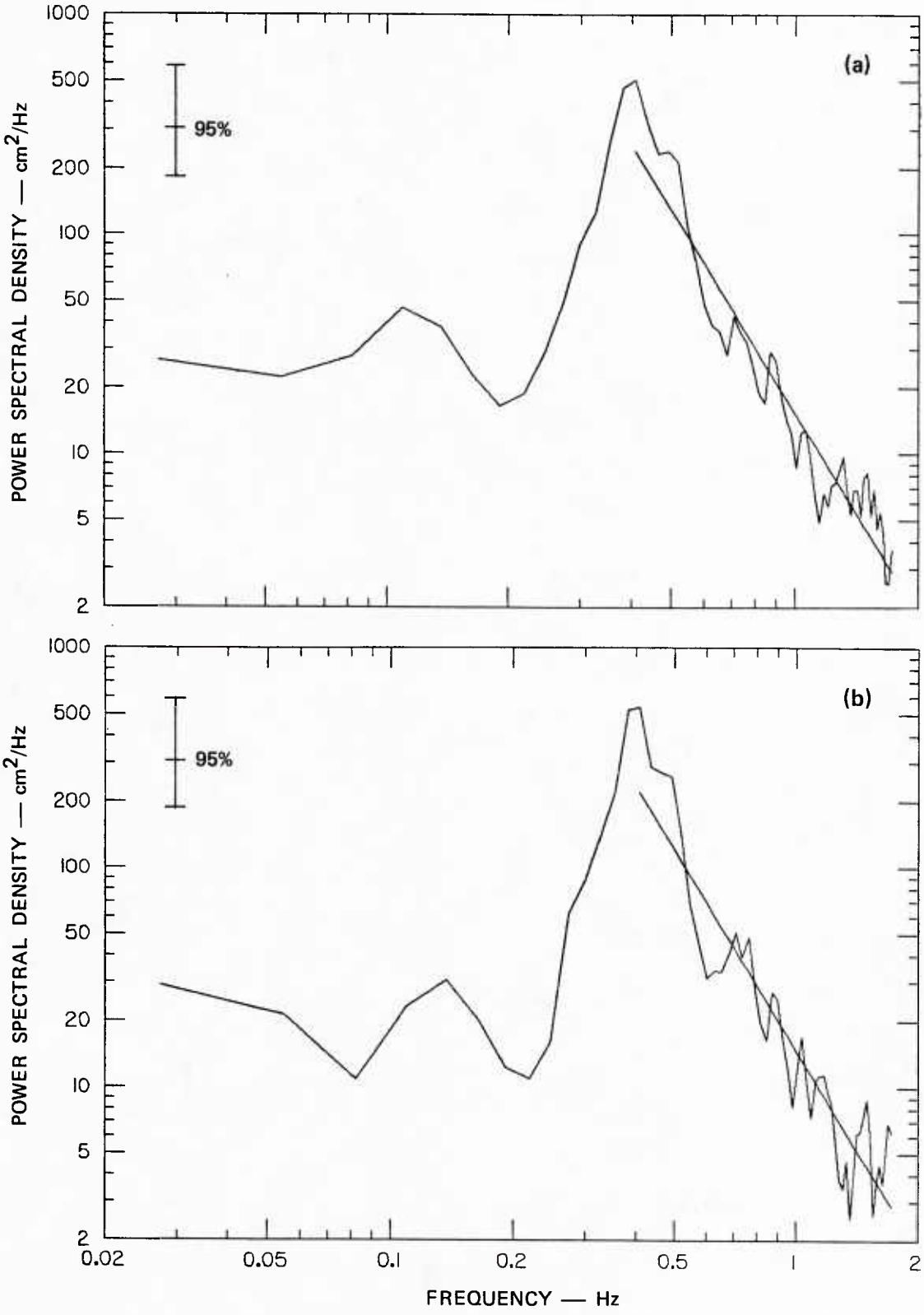

FIGURE 28 COYOTE POINT INCIDENT-WAVE SPECTRA MEASURED AT (a) OFFSHORE REFERENCE STAKE B SHOWING -3.1 SLOPE AND AT (b) STAKE A SHOWING -3.0 SLOPE

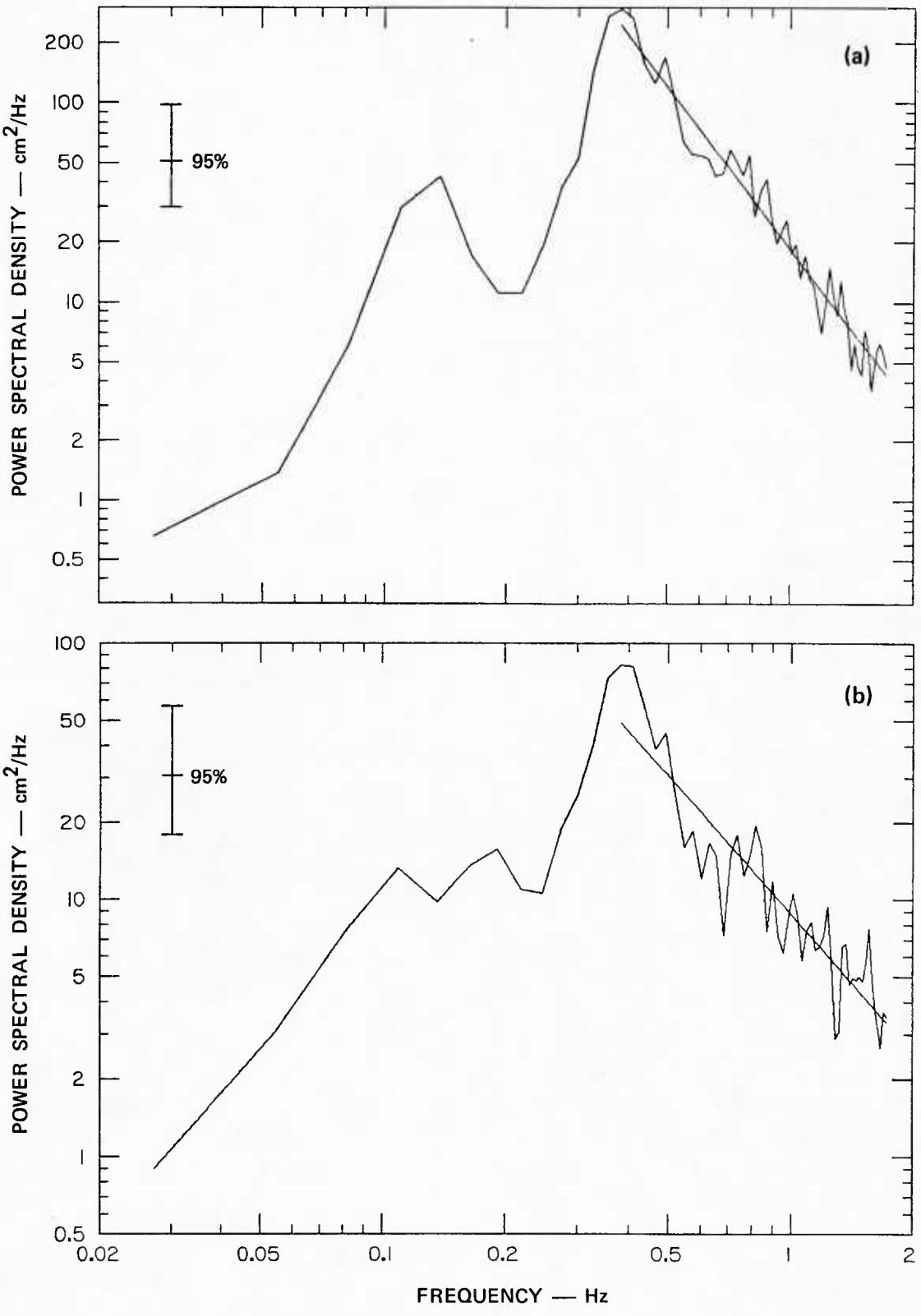

FIGURE 29 COYOTE POINT INCIDENT-WAVE SPECTRA MEASURED ALONG REFERENCE TRANSECT 1 AT (a) STAKE 15 SHOWING -2.7 SLOPE AND (b) STAKE 10 SHOWING -1.8 SLOPE

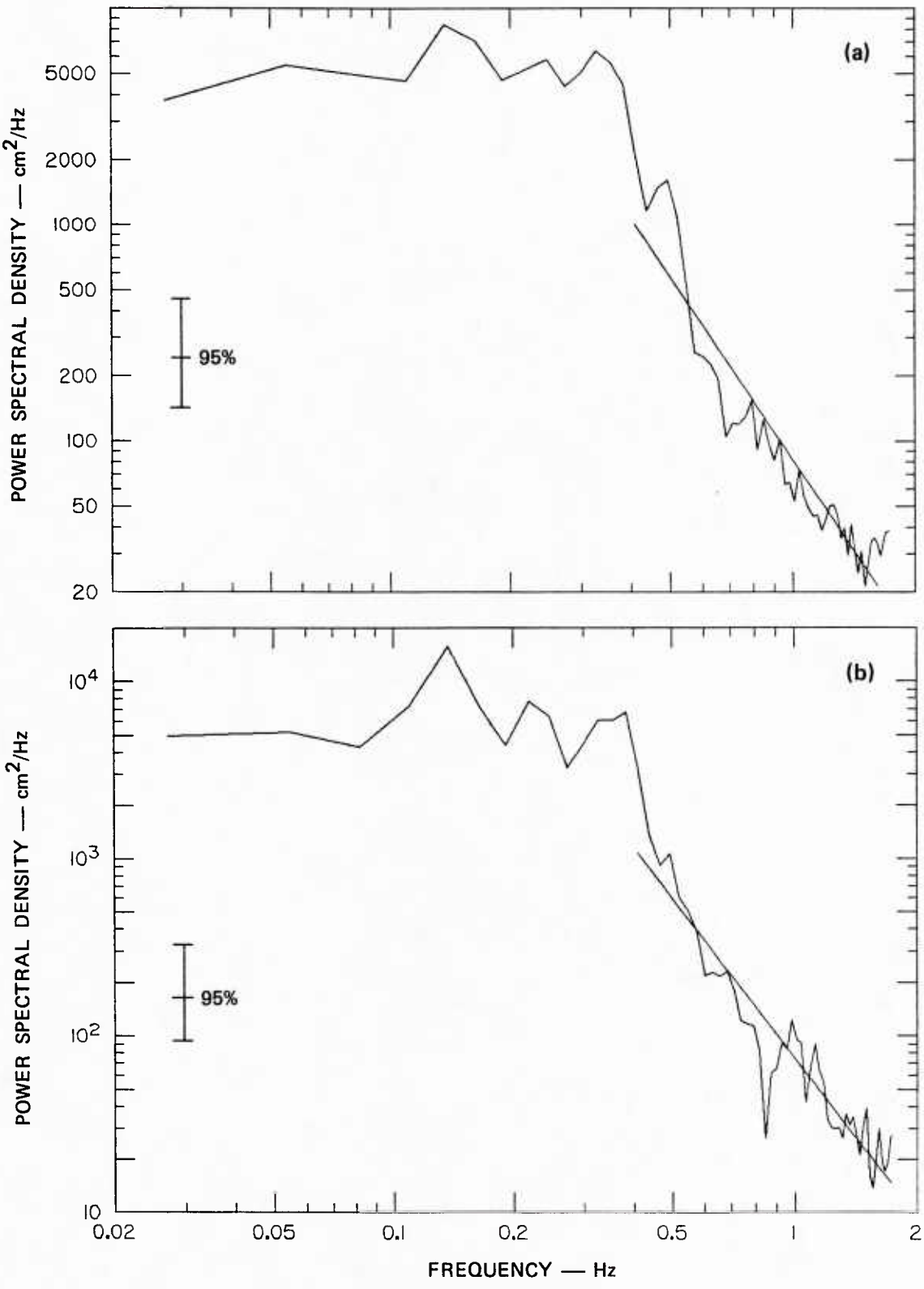

FIGURE 30 COYOTE POINT RUN-UP SPECTRA MEASURED ALONG (a) REFERENCE TRANSECT 1 SHOWING -2.8 SLOPE AND ALONG (b) TRANSECT 3 SHOWING -3.0 SLOPE

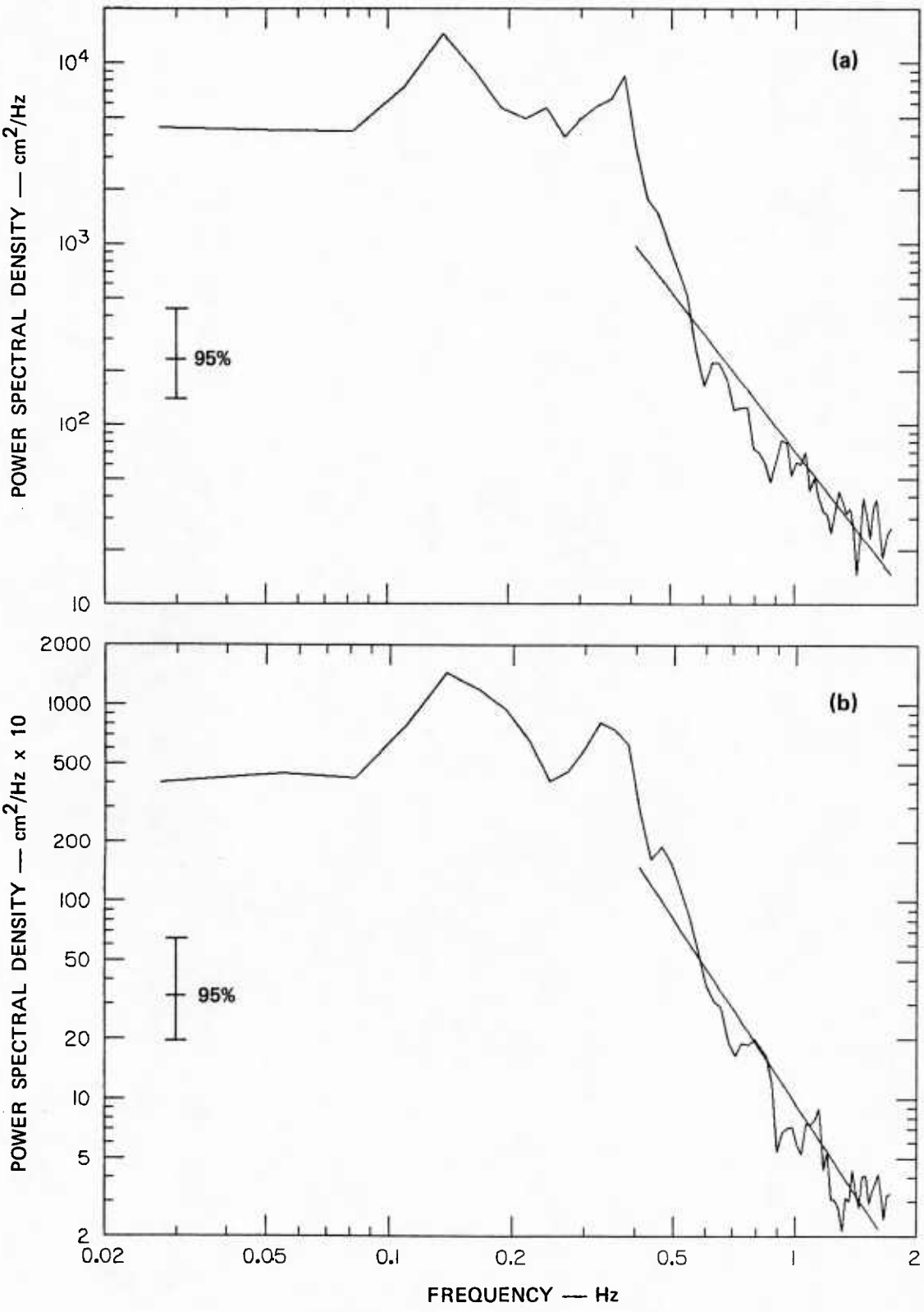

FIGURE 31 COYOTE POINT RUN-UP SPECTRA MEASURED ALONG (a) REFERENCE TRANSECT 5 SHOWING -2.9 SLOPE AND (b) TRANSECT 6 SHOWING -3.1 SLOPE

Table 9

COYOTE POINT SPECTRAL SLOPES

Data Type	Location	Slope
Run-up	Transect 1	-2.8
	Transect 3	-3.0
	Transect 5	-2.9
	Transect 6	-3.1
Waves	Stake B	-3.1
	Stake A	-3.0
	Stake 15	-2.7
	Stake 10	-1.8

conducted for run-up/wave time series pairs and for run-up/run-up pairs to estimate the amount of linear correlation in the onshore-offshore and alongshore directions, respectively.

To estimate the onshore-offshore correlation between the run-up and the incident waves, the coherence and phase were computed between the run-up measured at reference transect 1 and the incident waves measured at reference stakes B, 15, and 10. Figures 32(a,b) and 33(a) show the coherence squared and the associated phase in radians plotted as a function of frequency in hertz for the run-up measured along transect 1 and the waves measured at offshore stakes B, 15, and 10. The 95% confidence limits are shown in Table 10 as a function of coherence squared. The acceptance region for $\gamma_{xy} \geq 0$ at the 95% confidence interval ($\alpha = 0.05$) is 0.21. Values of $\gamma_{xy} \geq 0.21$ are considered statistically significant. All of the Coyote Point coherence and phase plots are presented in the same linear-log format shown for the Alameda Beach data. These coherence and phase plots may be compared with the appropriate spectra plotted in log-log format in Figures 28 to 31.

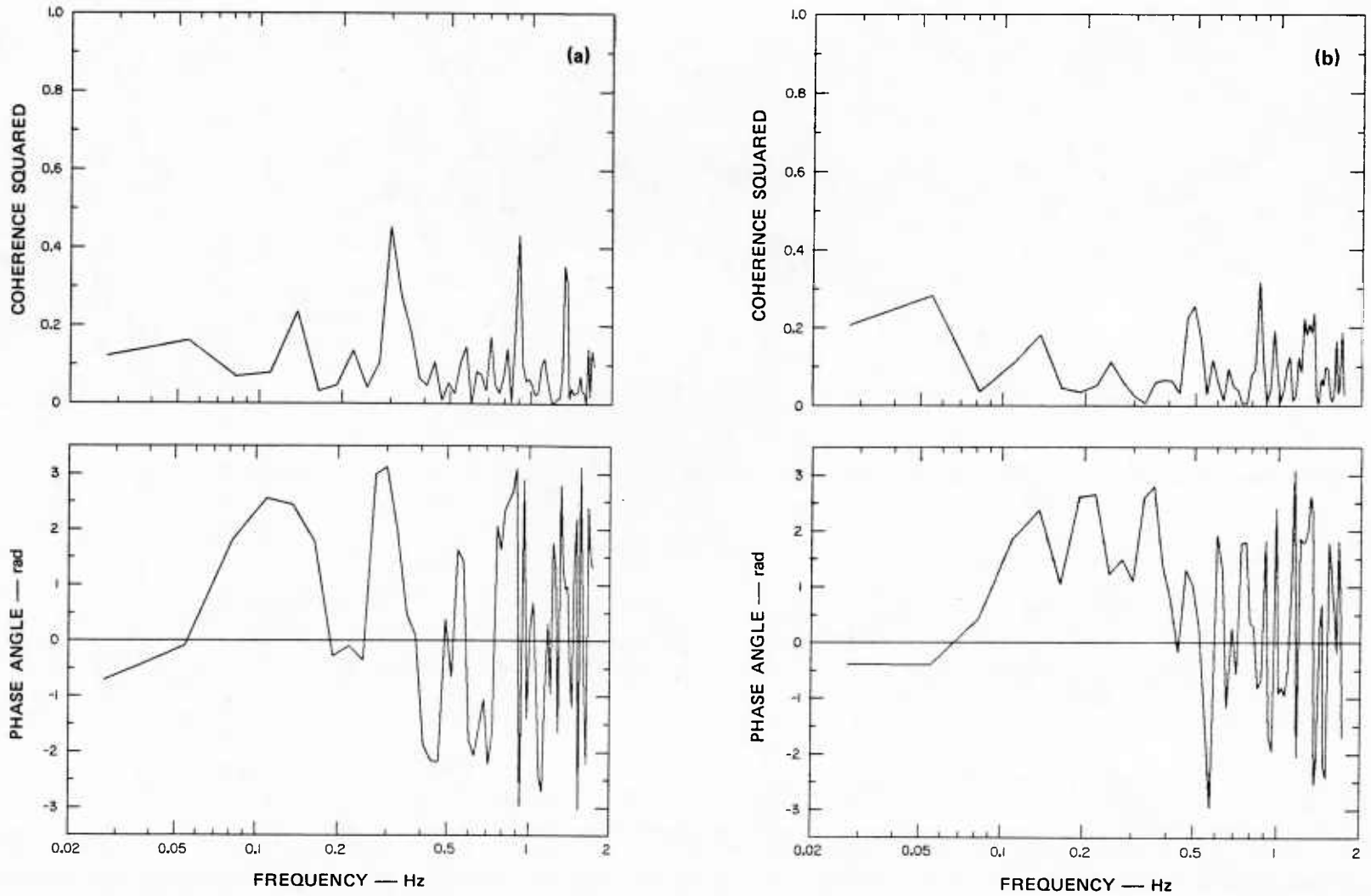

FIGURE 32 COYOTE POINT COHERENCE AND PHASE BETWEEN THE RUN-UP ALONG TRANSECT 1 AND THE INCIDENT WAVES AT (a) STAKE B AND (b) STAKE 15

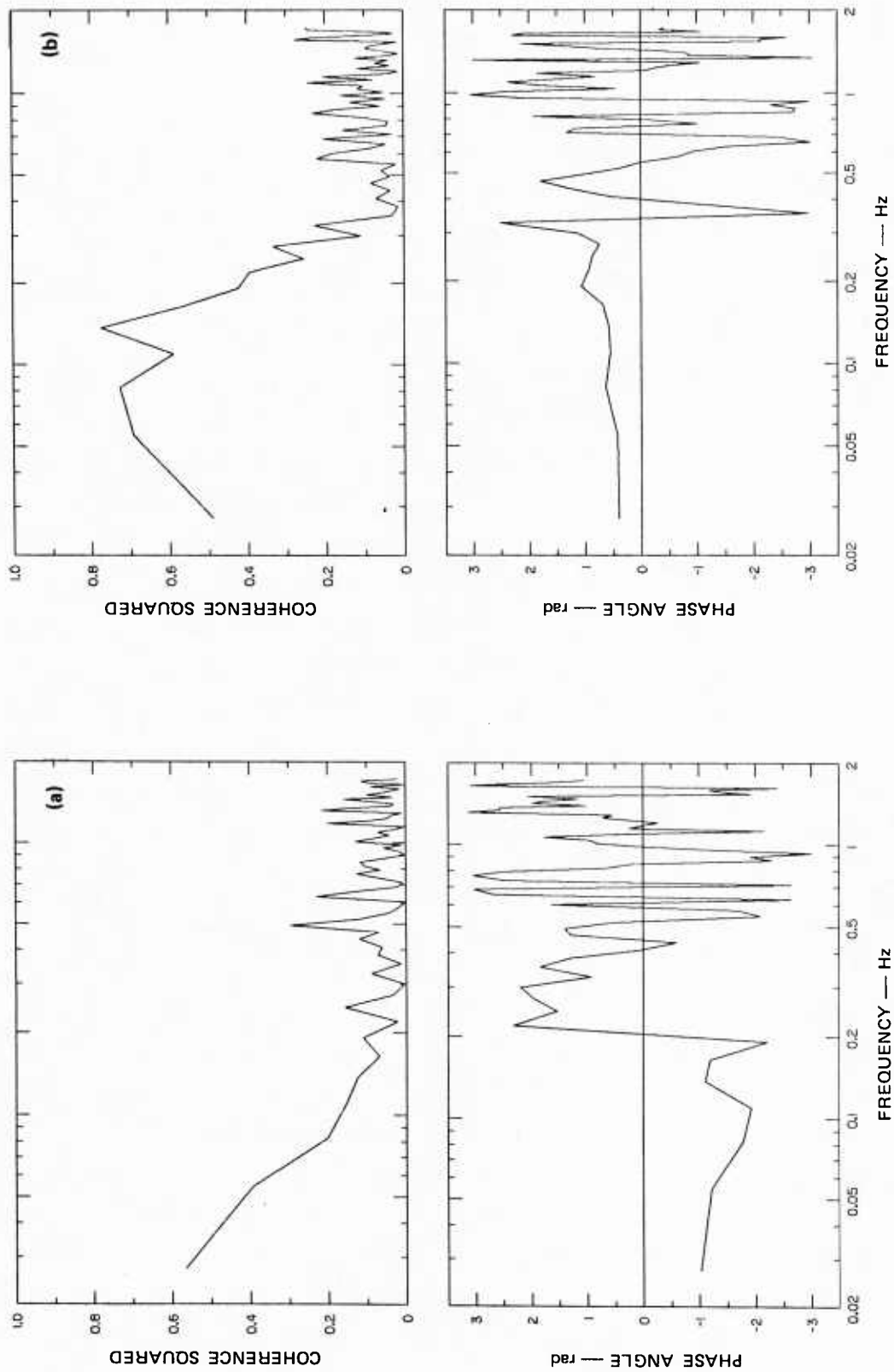

FIGURE 33 COYOTE POINT COHERENCE AND PHASE BETWEEN THE RUN-UP ALONG TRANSECT 1 AND (a) INCIDENT WAVES AT STAKE 10 AND (b) RUN-UP ALONG TRANSECT 3

Table 10

THE 95% CONFIDENCE LIMITS FOR $\gamma^2(f)$ WHEN DF = 23

$\gamma^2(f)$	0.4	0.5	0.6	0.7	0.8	0.9
Upper limit	0.66	0.73	0.79	0.85	0.90	0.95
Lower Limit	0.07	0.15	0.26	0.39	0.56	0.76

DF = Number of degrees of freedom.

In each case, the correlation between the incident waves and the run-up at transect 1 is low. The coherence squared between the run-up and waves at stake 15 shows harmonic spikes at approximately 0.3, 0.9, and 1.2 Hz. The presence of the harmonics is expected for the highly nonlinear conditions at stake 15. The coherence is relatively low even at these points. The coherence between the run-up at transect 1 and the incident waves generally decreases in the shoreward direction, with the exception of the very low frequencies in the correlation between the run-up and waves at stake 10, where the highest γ^2_{xy} value is about 0.55. Phase in the wave and run-up correlations is generally random at frequencies above 0.5 Hz, which is consistent with qualitative comparison of the narrow-band incident-wave spectra and the run-up spectra.

The alongshore correlation in the run-up was also examined by computing the coherence and phase between the run-up time series measured at transects 1, 3, 5, and 6. The calculations were made for all combinations of the time series pairs, and the results are shown for combinations of run-up at transect 1 and transects 3, 5, and 6. These results are representative of all combination studied here. Figure 33(b) shows the squared coherence and the phase computed for the run-up at transects 1 and 3, and Figure 34 shows the coherence and phase for the run-up measured at transects 1 and 5 and transects 1 and 6. Phase in the run-up correlations is generally random above 0.4 Hz, and coherence is low. The spatial separation between transects 1 and 6 is approximately 3.5 m. Coherence squared is generally high between all four run-up transects across the

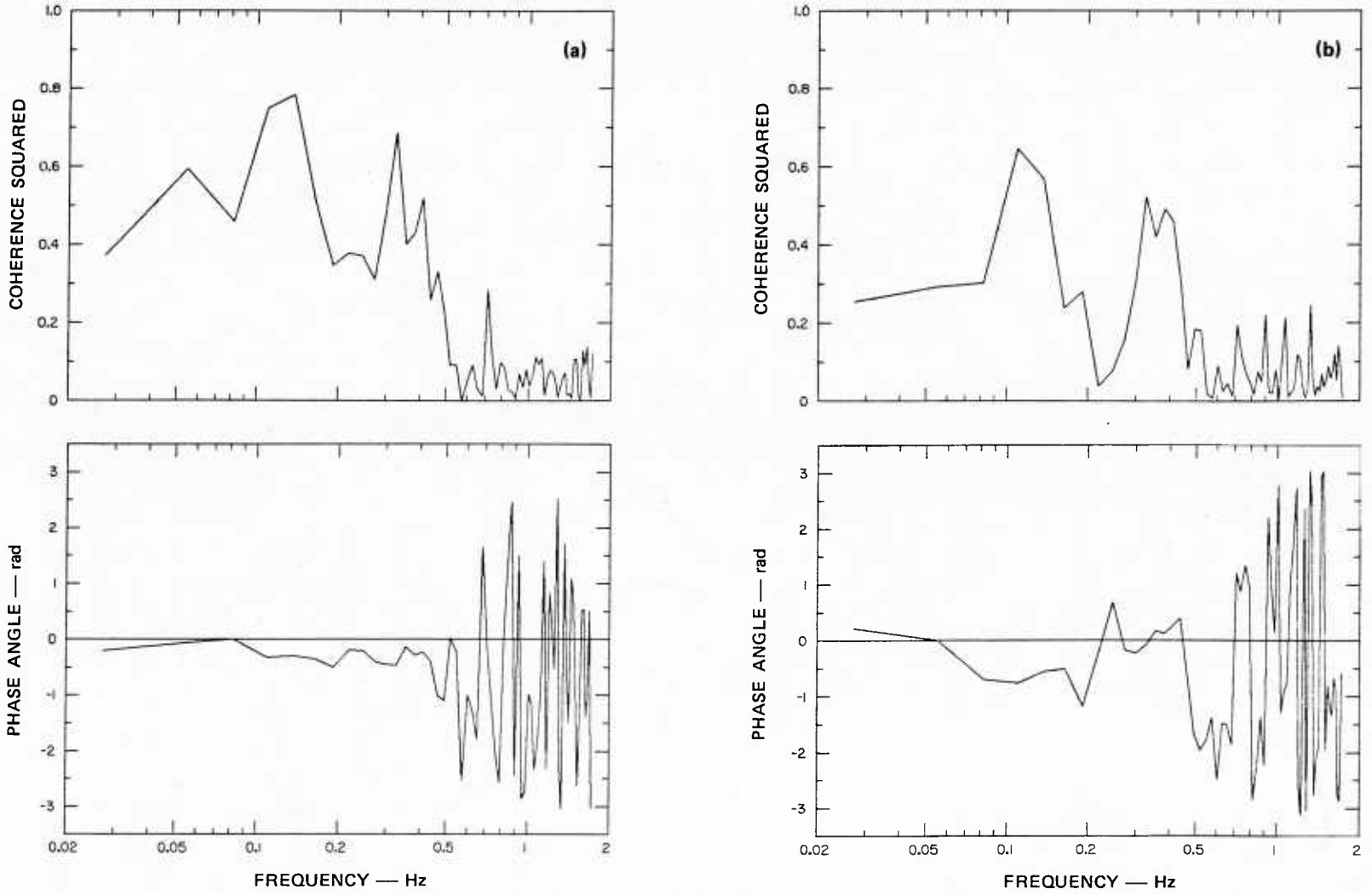

FIGURE 34 COYOTE POINT COHERENCE AND PHASE BETWEEN THE RUN-UP ALONG TRANSECT 1 AND THE RUN-UP ALONG (a) TRANSECT 5 AND (b) TRANSECT 6

lower frequency bands containing the predominant run-up spectral energy, reaching a maximum of approximately 0.8. The alongshore correlation in the run-up does tend to decrease, however, with increasing separation between measurement points. Across all transects, the coherence does remain consistently high near 0.14 and 0.38 Hz, the frequencies of the dominant peaks in the run-up spectra. The phase is nearly constant and is approximately zero in the band of frequencies less than 0.3 Hz, where the coherence is high, indicating that the time series are in phase.

4. Cumulative Distributions

The CDFs of the time series recorded for the run-up at transects 1, 3, 5, and 6 and for the incident waves at offshore stake A were compared to model normal and Rayleigh distributions. As with the Alameda Beach data, the KS statistical hypothesis test was used to quantify the goodness-of-fit between the empirical and the model distributions. The X^2 test was also used as an additional measure of the goodness-of-fit between the empirical Coyote Point run-up CDF and the model normal CDF.

Prior to application of the statistical hypothesis testing, the incident-wave and run-up time series were modified as described earlier for the Alameda data. Eq. (35) was used to transform the raw calibrated time series of amplitude fluctuations into time series of standard deviations for both the run-up and the incident waves. The CDF of the standard deviation time series was computed and plotted on the same plot as the standard (0,1) normal distribution.

Figure 35 shows both the empirical and the model normal CDFs for the run-up at transects 1 and 3. The ordered variable value computed by using Eq. (35) is plotted as a function of cumulative probability in percent. A similar comparison is made in Figure 36 between the normal CDF and empirical CDF computed for the run-up at transects 5 and 6, using the same plotting format and variable transformation. In each instance, the fit between the model- and data-derived CDF is very close.

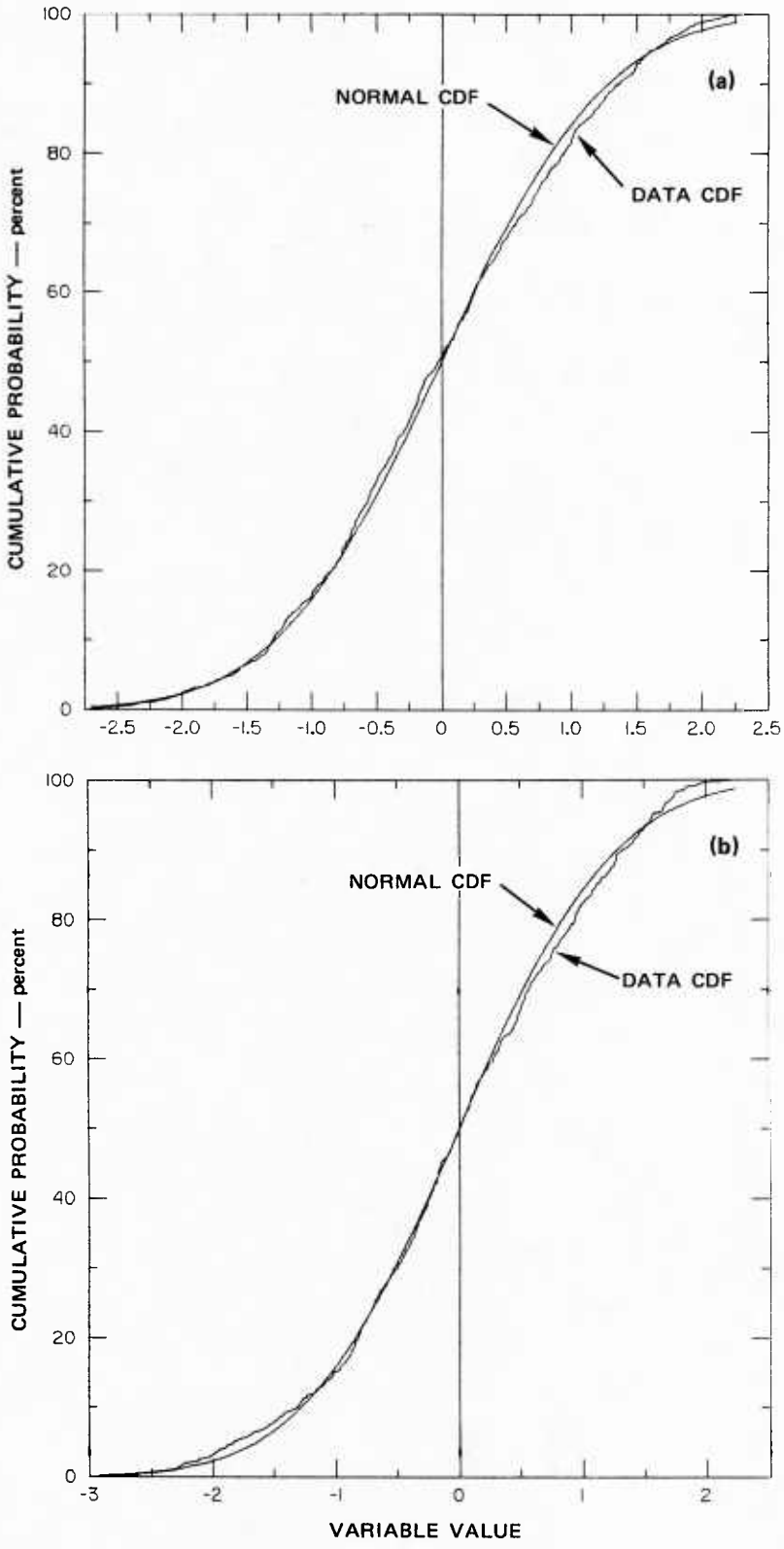

FIGURE 35 COMPARISON OF A NORMAL CDF AND CDFs COMPUTED FOR COYOTE POINT RUN-UP ALONG (a) TRANSECT 1 AND (b) TRANSECT 3

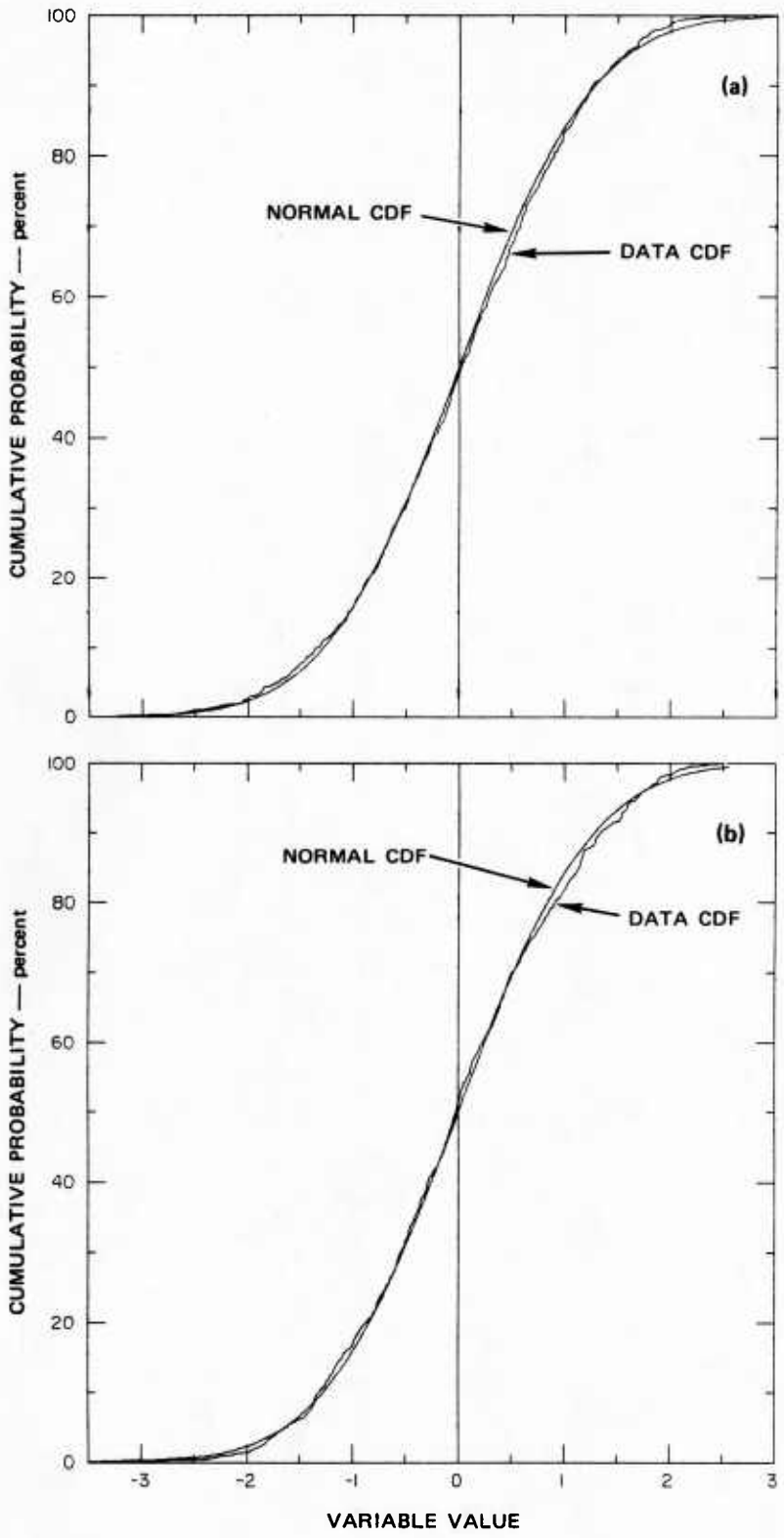

FIGURE 36 COMPARISON OF A NORMAL CDF AND CDFs COMPUTED FOR COYOTE POINT RUN-UP ALONG (a) TRANSECT 5 AND (b) TRANSECT 6

The KS goodness-of-fit test was applied to the data shown in Figures 35 and 36 by first forming hypotheses H_0 and H_1:

H_0: Null hypothesis - data are normally distributed

H_1: Alternate hypothesis - data are not normally distributed.

The same approach as described previously for the Alameda Beach KS test was used, based on the methods summarized in Section IV. The maximum deviation between the empirical and standard (0,1) normal CDF was computed and compared against the tabulated KS critical statistic. The test results are summarized in Table 11. The null hypothesis is accepted if $D < C$ and rejected if $D \geq C$. The KS test results show that the null hypothesis cannot be rejected at the 95% confidence interval in any of the tests, and thus a Gaussian, or normal, distribution is not statistically different from the Coyote Point run-up data for all four transects reported here.

Table 11

KS TEST RESULTS FOR COYOTE POINT RUN-UP
VERSUS A NORMAL DISTRIBUTION

Transect	N	C	D	Result
1	943	0.044	0.025	Accept H_0
3	820	0.047	0.025	Accept H_0
5	943	0.044	0.027	Accept H_0
6	943	0.044	0.030	Accept H_0

N = Number of data points used in test.

C = KS test critical statistic (α =0.05).

D = Maximum discrepancy between the normal and empirical CDFs.

Result: Accept H_0 if $D < C$; otherwise, reject H_0.

A X^2 test was also applied to the run-up data recorded at these four transects as a second test of the goodness-of-fit between the

empirical data and a normal distribution. Specifics of the X^2 test were summarized in Section IV. The raw calibrated time series data were used for the X^2 test without additional transformation. The data were, however, debiased and detrended prior to application of the test. Again, the maximum deviation was computed, this time between the observed and the expected frequencies of data observations within the given observation window in the frequency histogram. The same hypotheses, H_0 and H_1, were formed, and the results of the X^2 test are summarized in Table 12. The null hypothesis cannot be rejected in any of the four cases. The observed value of the X^2 statistic is less than the expected value in each case, and thus, based on the X^2 test, the Coyote Point run-up data are not different from a normal distribution at the 95% confidence interval.

Table 12

X^2 TEST RESULTS FOR THE COYOTE POINT RUN-UP

Transect	N	DF	Observed X^2	Expected X^2	Result
1	945	6	8.6	12.6	Accept H_0
3	820	7	13.7	14.1	Accept H_0
5	940	6	8.8	12.6	Accept H_0
6	945	12	19.0	21.0	Accept H_0

N = Number of data points used in test.

DF = Number of degrees of freedom.

Result: If observed X^2 < expected X^2, then accept H_0; otherwise, reject H_0.

The distributions of the run-up data were also tested against a Rayleigh distribution. Due to the positive nature of the Rayleigh distribution, the raw calibrated run-up time series data were transformed using Eq. (36), as described for the Alameda data, prior to computation of the run-up CDF at each reference transect. The empirical run-up distribution functions are compared to the Rayleigh distribution of Eq. (37) in Figures 37 and 38. CDFs for the run-up at transects 1 and

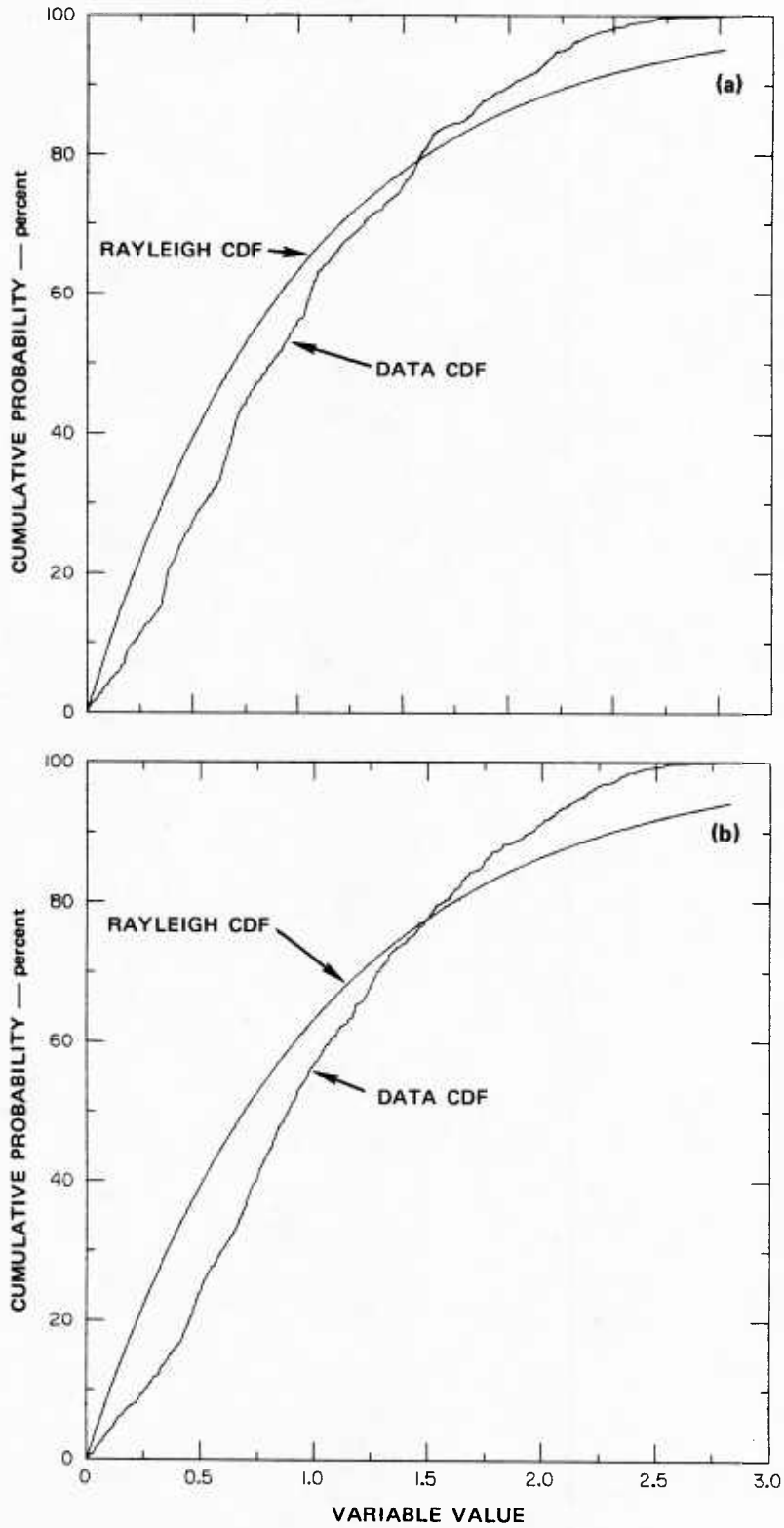

FIGURE 37 COMPARISON OF A RAYLEIGH CDF AND CDFs COMPUTED FOR COYOTE POINT RUN-UP ALONG (a) TRANSECT 1 AND (b) TRANSECT 3

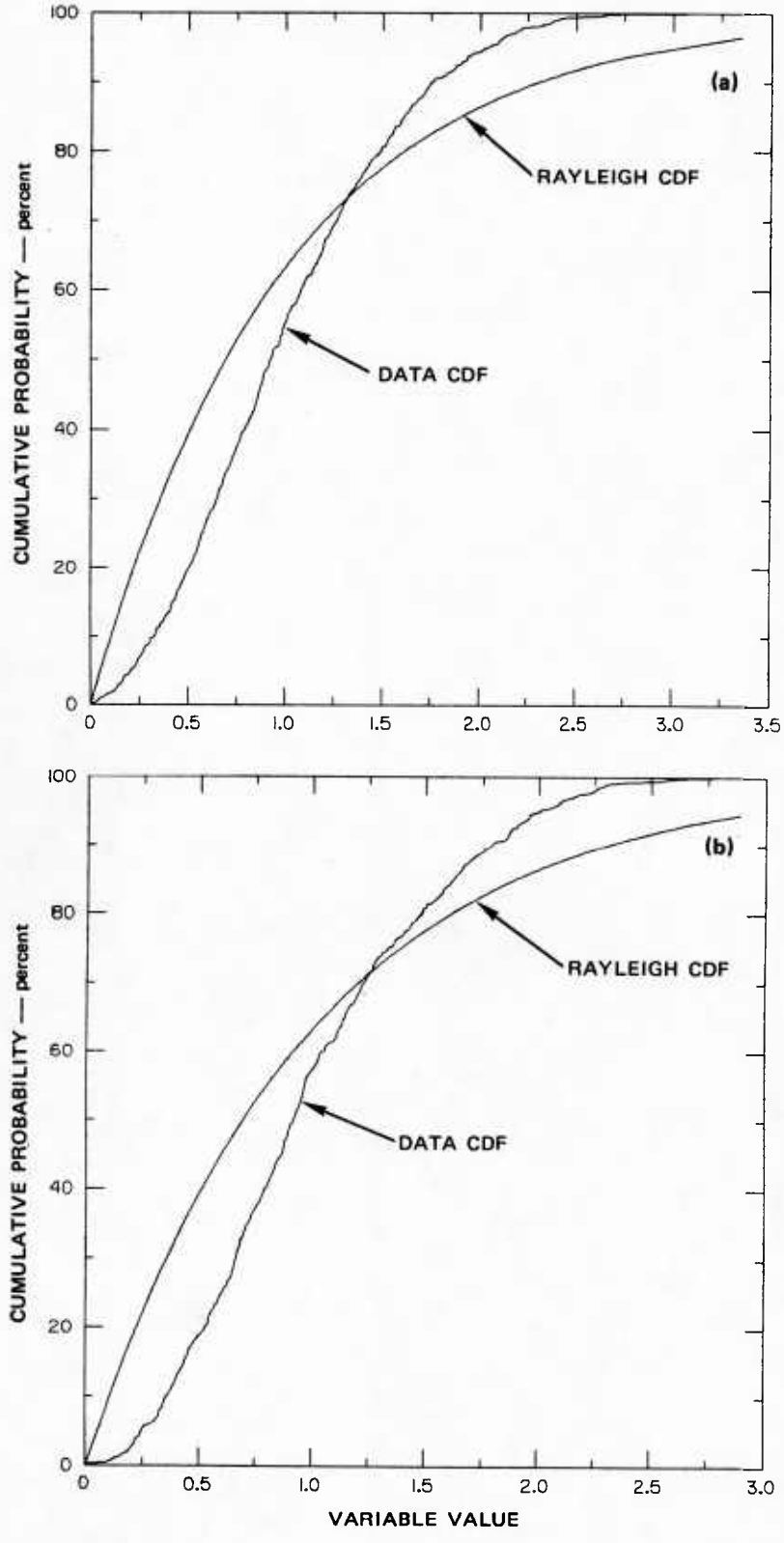

FIGURE 38 COMPARISON OF A RAYLEIGH CDF AND CDFs COMPUTED FOR COYOTE POINT RUN-UP ALONG (a) TRANSECT 5 AND (b) TRANSECT 6

3 (Figure 37) and transects 5 and 6 (Figure 38) show a wide margin of difference with the Rayleigh distribution. Hypotheses H_0 and H_1 were formed for a Rayleigh distribution in these tests, and the results are summarized in Table 13. The null hypothesis, H_0, was rejected at the 95% confidence interval in all four cases. Based on these tests, the amplitude distribution of the Coyote Point run-up measured at transects 1, 3, 5, and 6 are not statistically different from a standard (0,1) normal distribution but is different from a Rayleigh distribution.

Table 13

KS TEST RESULTS FOR THE COYOTE POINT RUN-UP VERSUS A RAYLEIGH DISTRIBUTION

Transect	N	C	D	Result
1	943	0.044	0.14	Reject H_0
3	820	0.047	0.17	Reject H_0
5	940	0.044	0.20	Reject H_0
6	943	0.044	0.21	Reject H_0

N = Number of data points used in test.

C = KS test critical statistic.

D = Maximum discrepancy between the Rayleigh and empirical CDFs.

Result: Accept H_0 if $D < C$; otherwise, reject H_0.

These same tests were repeated at offshore reference stake A. The empirical CDF for the waves at stake A is shown plotted with the (0,1) normal distribution in Figure 39(a) and with the Rayleigh distribution in Figure 39(b). While the Rayleigh distribution does not accurately describe the amplitude distribution of offshore waves, the normal distribution appears to come close. Quantitatively, the normal distribution fails the KS test at the 95% confidence interval, however, with the KS critical statistic equal to 0.044 and the maximum deviation, D, of the empirical CDF from the model CDF equal to 0.053. Thus, the incident

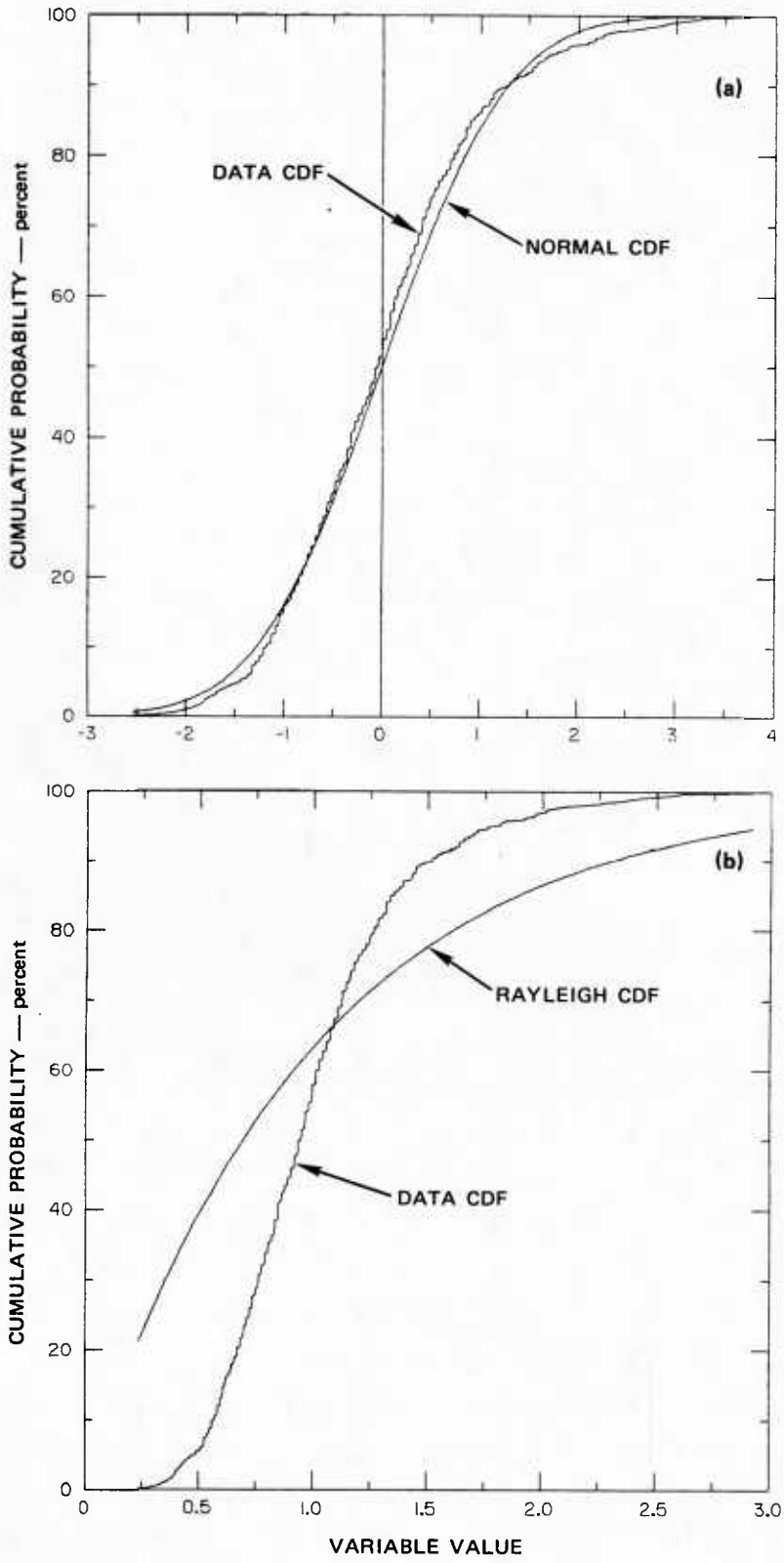

FIGURE 39 COMPARISON OF COYOTE POINT INCIDENT WAVES MEASURED AT STAKE A AND (a) NORMAL AND (b) RAYLEIGH CDFs

waves could be qualitatively described as nearly normally distributed, but this is not confirmed statistically at the 95% confidence interval. It is interesting to note, however, that the KS critical statistic computed at the 99% (α =0.01 in Table 4) confidence interval is 0.0532, approximately equal to D computed above. Practically speaking, the waves could be assumed to be normally distributed at the 99% confidence interval. Recall that the KS critical value is inversely proportional to $\sqrt{N}$, and that as N grows larger, it becomes increasingly difficult for the data to pass the KS test, even for very close fits. Hence, it may be acceptable in this instance to model the distribution of the offshore incident waves using a normal distribution function. Further testing would be suggested however.

VI DISCUSSION

It is interesting that two field sites were selected randomly, each with similar yet statistically different incident-wave and beach slope conditions, and in both cases low-frequency wave run-up was observed with similar characteristics. A small percentage of run-up energy was observed at the incident-wave peak frequency, but the largest percentage of the run-up energy was located at frequencies that were significantly lower. The fact that some run-up spectral energy is located at the predominant incident-wave frequency seems to indicate that a small percentage of the offshore-wave characteristics are transmitted to the run-up. Although wave-breaking by plunging is a highly nonlinear process, there is some memory involved whereby some of the incident-wave frequency information is transferred to the run-up. The mechanism for this transfer may be the collision between the seaward-moving backwash and the shoreward-moving incident bore.

The correlation analyses generally showed little or no linear coherence between the offshore incident waves and the run-up on the beach. Some statistically significant coherence was observed at the very low frequencies between the run-up along transect 1 and the bores measured at stake 10. The coherence was high between all of the run-up transects. After the wave broke and formed a bore, some low-frequency energy was present that was linearly correlated with the run-up on the beach face. The offshore incident-wave time series were time-lagged prior to computing the coherence and phase with the run-up, to account for the spatial separation between measurement positions. The time-lagging did not significantly increase the coherence levels. Although highly variable phase can indicate large time delays, the time-lagged phase remained random. The low linear coherence levels between the offshore wave measurements and the run-up on the beach are real and not processing artifacts.

Visual and photographic observations of the run-up made during the field experiments revealed a common behavior, and a typical swash-cycle scenario was identified. A wave broke by plunging in the shallow water near the shoreline, forming a bore that traveled a very short distance before surging up the beach. Before this first wave reached the run-up limit and began its backwash, a second wave plunged and surged up the beach face over the top of the moving layer of water created by the first wave. The backwash generated by the combination of these first two waves would often attenuate the run-up of the subsequent wave, thereby producing a modulation of the swash cycle. Generally, more than one swash crest was present on the beach at all times. Thus, a resonance effect appears between individual swash cycles whereby the run-up of one swash cycle may reinforce that of the next, and their subsequent backwash may attenuate the run-up of the successive wave. This process was simulated by the model described in Appendix C.

Because a spectrum of incident-wave frequencies was present, the relative timing between the run-up and backwash was not always a constant, thus creating the spectrum of low run-up frequencies. Peaks in the run-up spectrum are observed in each field data set at frequencies near the first subharmonic as well as at lower frequencies. In all instances, the spectral peaks in the run-up located at frequencies lower than the predominant incident-wave frequency contain a significantly greater proportion of the run-up spectral energy than the run-up in the incident-wave frequency band.

The red-shift often observed in run-up frequency spectra relative to the corresponding incident-wave spectra may be due to different mechanisms. The beach does appear to behave as a low-pass filter to the incident waves when exposed to a broadband spectrum of incident-wave energy. When exposed to both long swell waves and shorter wind waves, the longer waves produce the larger run-up excursions, and the run-up generated by the shorter waves becomes embedded in the long-wave run-up. As a result, the run-up spectrum shows a prominant peak at the long-wave frequency, as well as at other frequencies.

Unlike the run-up field data reported in the open literature, however, the Alameda and Coyote Point run-up measurements were specifically made for wind-wave conditions exclusively. The Alameda and Coyote Point incident-wave fields were narrow-band in frequency and contained only one predominant wind-wave component. The peak in the run-up spectrum coincident with the incident-wave peak frequency was not produced by long waves masking the run-up generated by shorter waves. Instead, the incident wind waves produced components in the run-up at their characteristic frequency and at lower frequencies through the interaction of the run-up and backwash during the swash cycle. If the beach were simply acting as a low-pass filter to the incident-wave field, the run-up spectral energy would be observed at the wind-wave frequency only, since that is the predominant forcing frequency at the shoreline. There is no bimodal or broadband distribution of incident-wave energy to be low-passed by the beach, but instead only one predominant forcing frequency.

This study has focused on the swash resonance problem. The resonance between the run-up and the backwash in the swash cycle can produce low-frequency energy in the run-up. Edge wave modulation of the run-up on the beach face can also produce low-frequency run-up spectral energy, possibly obscuring the measurements of swash resonance. Generally, it is desirable to have both current velocity and water surface amplitude measurements at various locations within the surf zone to identify the presence of edge waves. Since only amplitude data were available in this study, the beach conditions that prevailed at the selected field sites during the experiments must provide the basis for discounting the influence of edge waves on the run-up measurements.

The purpose of making the field measurements of incident waves and run-up on a dissipative beach (Appendix D) exposed only to narrow-band wind waves was to minimize edge-wave and standing-wave effects on the run-up. Edge waves are normal trapped modes of longshore periodic wave motion that occur along the shoreline and cannot radiate energy out into deep water. When combined in amplitude with the waves incident at the shoreline, edge waves can modulate the run-up on the beach face.

Edge waves can occur along both straight and curved shorelines and at beaches with linear, concave, or convex profiles. Edge waves can either be standing or progressive, and the standing variety has been linked to beach cusp formation.

It is not sufficient only to select a dissipative beach and declare that edge waves cannot be present. Waves on dissipative beaches can break several times at offshore bars and, following their reformation, can eventually reflect from the beach face. Thus, it is necessary to identify global and local surf zone scales. At beaches fronted by very wide surf zones, the entire beach system may be dissipative, but the beach face may be reflective. Conversely, a reflective beach system may have a dissipative beach face.

The reflectivity of a beach is a function of both beach slope and the type of waves incident at the beach. In this study, both the Coyote Point and Alameda beaches were dissipative, with respective ε values of 19 and 6 (Appendix D) and only one breaker zone present near the shoreline. The experiments were conducted for incident waves that broke only by plunging. Guza and Inman (1975) report that when incident waves break by plunging, edge waves are no longer visible in the run-up. This is not to say that the edge waves are present but not visible, but instead that the edge waves are completely suppressed. Guza and Bowen (1976) suggest that the turbulence and effective eddy viscosity increase rapidly with breaker height. Spilling or steep plunging breakers such as those present during both field experiments do not permit subharmonic resonances to occur since the strong viscous effects suppress the nonlinear instabilities and edge wave forcing. Guza and Bowen indicate that the resonance disappears when the incoming wave breaks cleanly by plunging, as did the waves measured in this study.

The beach reflectivity parameter ε described in Appendix D has been used to identify the beach/incident-wave conditions for which edge waves are expected to be present. Guza and Inman (1975) and Guza and Bowen (1976) show that for values of ε greater than about 2.4 to 3.0, waves cease to surge up the beach and begin to plunge, and edge wave

resonance disappears. The values of ε observed during the Alameda and Coyote Point experiments were respectively 6 and 19, both well above the critical value of 2.5, again supporting the absence of edge waves during the field experiments.

No regular alongshore modulation of the run-up was observed at any time during the field experiments. The shoreline remained straight, and no cusps or regularly spaced deposits of sea-foam or debris that may have been caused by edge waves were observed alongshore. The time series of the run-up measured at transects 1, 3, 5, and 6 all showed approximately the same mean value. Thus, no quantitative alongshore variability of the mean run-up was observed over the 3.5-m spatial separation of transects 1 and 6. In summary, all data suggest that edge waves were not present at either of the field sites during the experiments.

Huntley et al. (1977) proposed a universal form for swash spectra. As discussed in Appendix D, Huntley presented run-up spectra measured at four separate natural beaches. They observed an f^{-4} frequency dependence over the saturated portion of the run-up spectrum. The f^{-4} region of the spectrum was defined over the incident wind-wave frequency band. Guza and Thornton (1982) reported swash measurements for which an f^{-3} frequency dependence was observed. Guza and Thornton's results supported the premise of a saturated region of the run-up spectrum, but their observed slopes did not agree with Huntley's. Both the Alameda and Coyote Point run-up spectra show spectral slopes on the order of -3, which agrees well with the results of Guza and Thornton (1982). Thornton (1979) presented data for which an f^{-3} slope was observed over the high-frequency saturation region of shallow water surface amplitude and velocity spectra. While the Alameda and Coyote Point data shown here do not resolve whether the same mechanism is operative in both the surf zone and on the beach face producing the f^{-3} spectral slopes, these data do support the idea of saturated run-up spectra.

Generally, the log-log amplitude spectra measured during both field experiments show a decrease in spectral slope in the offshore-to-onshore direction. This observation is consistent with Thornton (1979). A -5

slope is observed in very deep water, where energy is slowly transferred from higher to lower frequencies in the spectrum. The energy transfer becomes more rapid as the waves propagate into shallow water, as evidenced in the slope decrease from -5 to -3 in the saturated portion of the spectrum. Very near the shoreline, the Coyote Point data show a further decrease in slope from -3 to -2, followed by an increase to -3 again in the run-up spectra. Thornton (1979) also shows surf zone spectra for plunging and collapsing breakers that display a -7/3 slope, suggesting possible surface tension effects on the spectral shape at high frequencies.

Several investigators have studied the statistical distribution of run-up amplitudes with similar yet statistically different conclusions. Consistently, however, either a normal (Gaussian) or Rayleigh distribution appears to provide a reasonable model for the run-up amplitude distribution. Webber and Bullock (1968) describe laboratory wind-wave tests during which the wave run-up was measured and found to be best described by a normal distribution. Battjes (1971) suggests that run-up is more appropriately modeled using a Rayleigh distribution based on an assumed Rayleigh distribution for incident-wave heights and the square of the wave periods. Battjes also assumed that the run-up of an irregular wave train could be approximated by using Hunt's formula. Sawaragi et al. (1977) used a modified Rayleigh distribution in their run-up distribution model. Most recently, Ahrens (1977) assumed a Rayleigh distribution for the run-up in his proposed method for predicting the run-up due to irregular waves.

Scaling inconsistencies can affect laboratory modeling of wave height and possibly run-up amplitude distributions. Assumptions made when developing a distribution model may lead to results that are not universally applicable. For these reasons, it is helpful and often enlightening to make in-situ measurements to substantiate assumptions made for modeling purposes.

The run-up measured during the Coyote Point field experiment showed a statistically good fit with a normal distribution, as verified by the X^2 and KS statistical hypothesis tests. Formal statistical hypothesis

test results have not been reported in the open literature where comparisons have been made between empirical data and a chosen model probability distribution. Many of the reported fits look good qualitatively but may not be acceptable in terms of formal statistical tests. For example, if one of the Rayleigh run-up models proposed in the literature were used to estimate the normally distributed Coyote Point run-up, agreement between model and in-situ observations might not be acceptable.

VII CONCLUSIONS

Field measurements of narrow-band, incident wind waves and the resulting run-up on the beach face were made at two different natural beaches. The run-up spectra measured at both beaches show low-frequency energy concentrated at frequencies much lower than the frequency band of the predominant incident waves. This low-frequency run-up spectral energy was generated on the beach face by the resonant interaction between the run-up and the backwash in the swash cycle. No low-frequency energy was observed in any of the incident-wave spectra measured either offshore or near the shoreline. No continuous offshore-to-onshore red-shifting of spectral energy was observed. Prevailing wave conditions and beach topography indicate that edge waves should not have been present during the experiments. Photographic observations of the swash cycle on the beach face indicated that a beat condition generated by the resonant interaction between the run-up and the backwash appears to be the source of the low-frequency energy.

Coherence between the incident waves and the run-up is very low across the surf zone. Although some run-up spectral energy is present at the dominant incident-wave frequency, the coherence level in this frequency band is not statistically significant. Wave-breaking by plunging and bore motion between the break point and the shoreline are highly nonlinear processes. Some incident-wave information appears to be transmitted to the run-up, but linear coherence estimates do not identify the mechanism. Nonlinear wave-wave interactions may permit such a transfer of energy across the surf zone; however, the data described here do not allow substantiation of this theory.

An equilibrium region of the run-up spectrum appears to exist over the frequency band of the incident breaking waves. Run-up spectra measured during both field experiments show consistent -3 slopes over the frequency band defined by frequencies greater than or equal to the incident-wave peak frequency.

The CDF computed for the Coyote Point run-up amplitude data is not statistically different from a standard (0,1) normal distribution. Use of run-up models found in the open literature based on Rayleigh or other distributions would probably not provide acceptable estimates of run-up behavior at the Coyote Point Beach during conditions similar to those existing during the field experiment. The Alameda run-up was statistically different from both normal and Rayleigh distributions, although the data were more nearly normally distributed.

VIII RECOMMENDATIONS

High-resolution wave run-up measurements generally are not readily available. Although wave amplitude and velocity measurements are frequently reported in the open literature, the link between those offshore measurements and the swash on the beach face is seldom made. A comprehensive experimental field program is needed to simultaneously measure the wave amplitude and current velocity fields near the shoreline and the run-up on the beach face. Although often painfully tedious to analyze, photographic measurements of incident waves and run-up provide accurate and reliable amplitude information. Such measurements should be made at multiple locations over a grid, using 35-mm or larger sized film, and should be accompanied by time-synchronized velocity measurements.

These measurements should be made for narrow-band wind wave conditions such as those that existed during the Alameda and Coyote Point experiments. Elimination of the swell-wave component from the spectrum of incident waves provides a less complex forcing mechanism for the swash on the beach; this would help keep the system relatively simple yet still ensure proper hydrodynamic scaling.

Appendix A

LABORATORY WAVE BASIN EXPERIMENTS

Laboratory measurements of incident waves and the resulting run-up were conducted to study the characteristics of run-up generated by monochromatic waves. The laboratory measurements were made in the 1.8- by 4-m (6- by 13-ft) wave basin in the Hydraulic Engineering Laboratory of the Hydraulic and Coastal Engineering Department at the University of California, Berkeley.

The selected wave basin features a full-width paddle-type wave maker driven by an electric motor with an eccentric crank that controls the paddle stroke. The paddle speed and the frequency of the generated waves are controlled by a hand-operated rheostat. An impermeable, steel beach with adjustable linear slope was used in one end of the basin. Metal shavings were used behind the wave paddle to minimize undesirable reflections.

The laboratory wave basin was set up and tested, and an electronic measurement system was constructed. Methods were devised to provide continuous analog recording of the incident-wave field in the wave basin. Equipment was assembled, tested, and calibrated, and off-line computer software was developed to provide post-experiment analysis of the measured time series.

1. Laboratory Equipment

The incident waves were measured at three locations within the wave basin as illustrated in Figure A-1. Wave gage 1 was mounted on a movable carriage to allow easy positioning relative to gage 2. The incident-wave time histories were measured by using resistance-type wave gages, bridge boxes with isolation transformers, and Daytronic Type 91 Strain Gage Transducers. The special isolation transformer bridges provided complete electronic isolation between adjacent wave

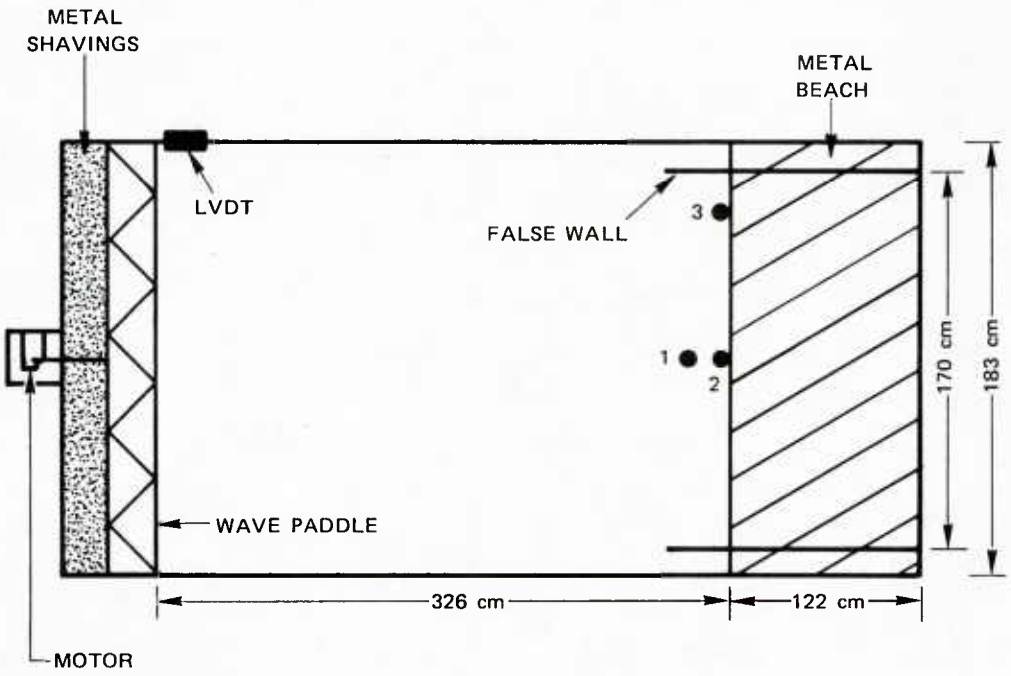

FIGURE A-1 WAVE BASIN GEOMETRY AND GAGE LOCATIONS USED IN THE LABORATORY EXPERIMENTS

gages, as described in Appendix G. The analog voltages from each gage were output to strip-chart recorders and simultaneously recorded on magnetic tape by a Model 3960 Hewlett Packard (HP) four-channel instrument recorder. The analog signal of the wave paddle motion was also directly recorded on the magnetic tape using a variable differential transformer (LVDT) connected to the wave paddle and driven by an HP dc power supply.

The wave probes constituted one resistance element on one leg of the bridge. The bridges were balanced with the wave probes immersed in the basin during still water conditions. When the circuit is balanced properly, any departure of the water surface from the mean causes an imbalance in the circuit. The magnitude and sense of the imbalance in the signal was amplified by the Daytronic unit and recorded on the magnetic tape.

During one of the testing and calibration experiments, data were recorded to verify that "pumping" of the steel beach by the incident waves was not a problem. The LVDT was attached to the beach surface

and the LVDT output was monitored while the incident waves broke on the beach face. No detectable beach motion was measured by the LVDT during the tests. Since very short waves were used in these laboratory experiments, beach pumping was not a problem during any of the experiments.

The wave run-up was recorded with the Bolex 16-mm movie camera used for the field experiments; the camera was mounted on a scaffold that straddled the wave basin. The camera motor drive was powered by another HP power supply, to provide a constant film exposure rate. The camera operation was controlled from the ground by means of a remote switch. The film exposure rate and camera lens aperture and focus were set prior to the experiments and checked between each experimental run. The ability to control the camera remotely eliminated the need for a camera operator on the scaffold, thus preventing unnecessary vibration of the camera during data recording. To aid in later analysis of the run-up photographs, a grid was affixed to the metal beach face, and the water was dyed dark blue. Fifteen reference lines were applied to the beach using white vinyl tape, and a linear grid with 1-cm increments was marked on each. The dyed water provided excellent contrast against the white grid lines during the run-up cycle. A quartz floodlight was used to provide the lighting for the photography. Also shown in Figure A-1 are the false walls used along the edges of the beach. These walls were constructed of plywood with neoprene rubber strips along the bottom that sealed against the beach and were used to eliminate potential instabilities due to water leakage along the side edges of the beach.

2. Methodology and Data Analysis

a. The Incident-Wave Measurements

A total of three runs were conducted during the laboratory experiment. The duration of these runs was determined by the time scales of the run-up and the incident-wave activity. Each experimental run was approximately 100 s in duration. At the frequency of the incident waves, this provided a statistically significant sample population of approximately 170 waves. Six earlier experiments were conducted to develop laboratory

hardware, computer software, and methodology. Only the incident-wave field was measured during these preliminary experiments. It was determined that time series approximately 100 s in duration provided sufficient resolution for these experiments.

For Runs 1 and 3, the incident-wave conditions were identical, but the beach slope was different. To simulate a field of irregular incident waves, the rheostat on the wave paddle control unit was oscillated by hand during Run 2. The paddle stroke and water depth was held constant for all three runs.

The wave gages were calibrated (on the strip charts and on the analog tape) both before and after the experiments to verify that the electronic drift was minimal and that their calibration transfer functions were linear throughout the range of interest. The net signal-to-noise ratio (SNR) was approximately 30 dB for all four channels. Here dB = 20log(R), where R is the ratio of signal voltage to noise voltage. Once the experimental system was set up, the wave paddle was started and the system was allowed to establish equilibrium. The incident waves and resulting run-up were then recorded simultaneously.

Analysis of the incident-wave records required several processing steps, as outlined in the data flowchart shown in Figure A-2. The incident-wave and paddle motion time series data on the four-channel analog tape was digitized at 40 Hz using an HP 21-MX computer and an analog-to-digital converter (ADC). To further reduce electronic noise, a four-channel RC filter (Appendix E) was built with a break frequency of approximately 10 Hz and approximately 35 dB of attentuation at the half-power point. This filter was placed in-line between the analog tape output and the ADC input. A sampling program on the computer digitized the four channels of analog time series data (three wave gages and the wave paddle) sequentially at 40 Hz per channel and output the digitized time series to a standard 9-track magnetic digital tape.

Three separate computer programs were developed to analyze the incident-wave time series read from the 9-track tape. The first of these was used to produce continuous time series plots for all four

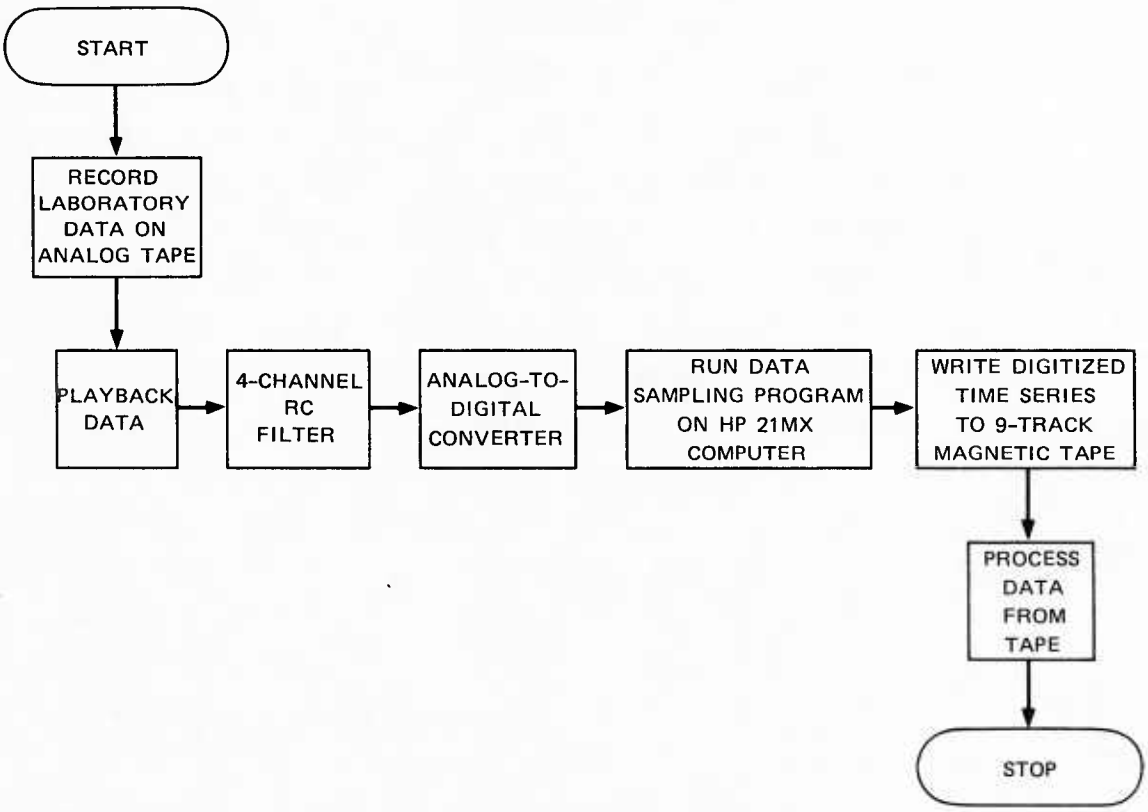

FIGURE A-2 DATA PROCESSING FLOWCHART FOR WAVE DATA RECORDED IN THE UCB WAVE BASIN

channels and to output values for the variables required for data calibration. These plots were used primarily for diagnostic purposes and data preview and calibration. Four large spikes that appeared on the plots were used to identify the transition between experimental runs. These spikes were produced by electronic signals recorded on the analog tape during the experiment at the beginning of each run. The second program for the incident-wave time series analysis provided calibrated time series plots, and the third program provided the actual spectral analysis of the calibrated time series for each channel. The results of these measurements are discussed in Section 3 below.

b. The Run-Up Measurements

The wave run-up was recorded using a Bolex 16-mm movie camera and a 100-ft roll of Kodachrome 25 daylight color film. The film exposure

rate was verified to be 14 Hz (frames per second) by analyzing the sweep hand motion of an analog clock visible in each of the movie frames.

The sequence of processing steps ultimately required to compute a run-up spectrum is shown in Figure A-3. The processed 16-mm movie film was digitized manually at a rate of 14 Hz using the photodigitizer at SRI. The photographic image was projected onto a Tektronix 4956 Graphics Tablet connected to a Tektronix 4052 terminal. An electronic pad with crosshairs was used to digitize the points of interest in the photograph. The resolution of the graphics tablet was approximately 0.03 cm (0.01 in.), which permitted the reference grid on the beach in the photograph to be digitized accurate to 0.08 mm $\pm$0.7 mm. This accuracy was contingent upon the clarity of the points being digitized in the photograph. This system was used to digitize the time series of the run-up motion on the beach face as recorded in the movie frames. The actual position of the leading edge of the run-up in the photograph was less clearly defined than the calibration grid on the beach face, and some minor loss of resolution was expected when digitizing the run-up time series. The digitized points were stored on cassette tape and subsequently transferred from the Tektronix terminal to a DEC VAX 11-780 disk file from which an HP-compatible 9-track ASCII digital magnetic tape was generated. Another separate program on the HP-21 MX was then used to read this tape, calibrate and plot the run-up time series, and compute the run-up spectra.

The run-up time series recorded photographically were calibrated from the oblique photo coordinates to physical units of centimeters using a method similar to that used for the field data analysis. A transfer function between the photo coordinates of the run-up calibration grid on the beach face and the actual physical coordinates was developed. The run-up time series were then calibrated directly by multiplication of the transfer function with the digitized oblique photo coordinates.

3. Laboratory Results and Discussion

This study focused on swash resonance generated on the beach face by the interaction of the run-up and backwash. It was necessary to

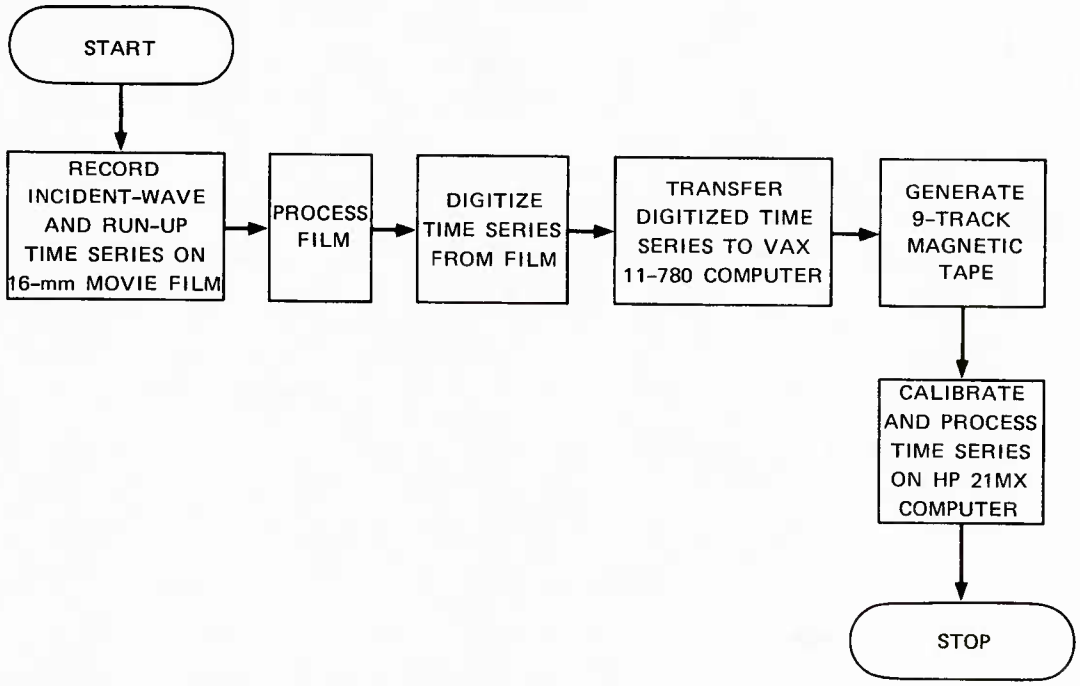

FIGURE A-3 DATA PROCESSING FLOWCHART FOR RUN-UP TIME SERIES DATA RECORDED PHOTOGRAPHICALLY IN THE LABORATORY

avoid reflective beach conditions in which resultant nonlinear perturbation of the incident-wave field might affect the frequency distribution of the run-up on the beach face. For this reason, both the laboratory and field measurements were conducted for dissipative beach conditions. Beach reflectivity and in-shore resonance may be characterized by a reflectivity or surf scaling parameter, ε, as discussed in Appendix D. Dissipative beach conditions are characterized by values of ε greater than about 2.5, and highly dissipative beaches yield ε values greater than 33. The experiments described here focused on swash activity in the moderately dissipative regime. Ideal beach reflectivity conditions for these laboratory experiments would yield values of ε between 5 and 20. Table A-1 shows the physical conditions for the laboratory experimental Runs 1 to 3 and the characteristic ε values. Clearly, the values were in the dissipative regime and, as expected, plunging breakers were observed in all three runs.

Table A-1

BEACH SLOPE AND INCIDENT WAVE CONDITIONS
FOR THE LABORATORY WAVE BASIN EXPERIMENTS

Run	Water Depth (cm)	Beach Slope (deg)	Frequency (Hz)	H_{rms} (cm)	ϵ
1	13.0	8.0	1.69	1.20	13.7
2	13.0	8.0	1.80	1.33	17.2
3	13.0	8.5	1.69	1.20	12.1

In the three runs conducted during the experiment, conditions for Runs 1 and 3 differed in beach slope only. The beach slope used for Run 3 was 0.5° steeper than for Run 1 but produced no visible change in the run-up. For this reason, only the results for Runs 1 and 2 are presented here. For Run 2, the wave paddle rheostat was oscillated by hand, producing a distinct change in the incident waves and the resulting wave run-up.

a. Experimental Run 1

The wave paddle was set to generate an incident-wave train with a single frequency and amplitude for Run 1. Figure A-4(a,b,c) shows the incident-wave time series recorded at wave gages 1, 2, and 3, and Figure A-4(d) shows the time series for the wave paddle horizontal motion. The position of the gages is illustrated in Figure A-1. The plots shown in Figure A-4 were produced by the computer program and are not strip-chart records. However, these computer-generated plots are identical with the strip-chart plots and were scaled here to enhance visual clarity. The plot segments for each channel form a continuous time series if placed end to end starting with the top segment. Each plotted segment is 6 cm full-scale; i.e., the calibrated time series are plotted from +3 cm to -3 cm, and the time series may be compared directly between channels since they are registered in time. The time series are not, however, time-lagged to account for the spatial separation of the wave gages. Time increases from left to right across the figure and from

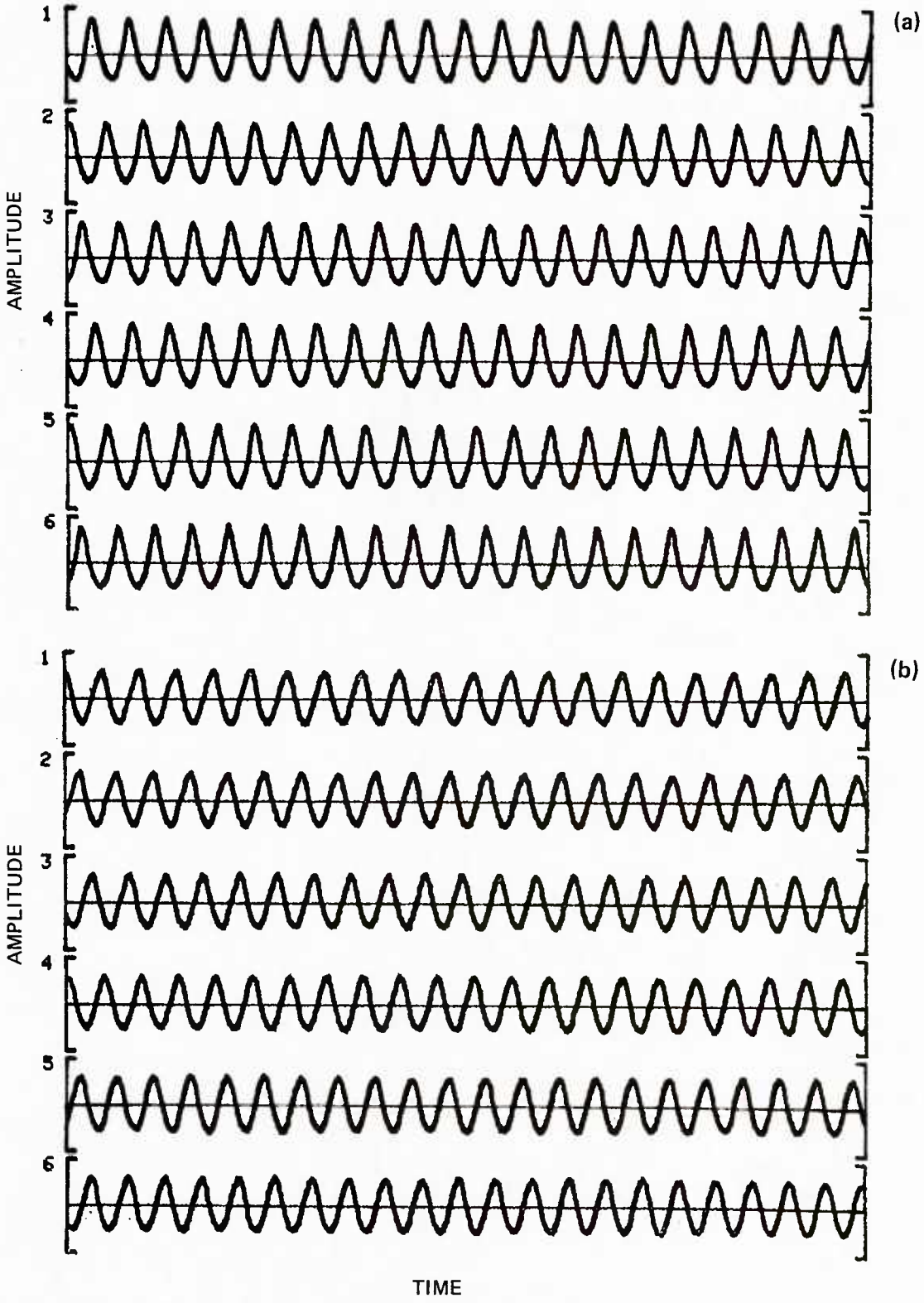

FIGURE A-4 TIME SERIES FOR (a-c) INCIDENT WAVES AND (d) PADDLE MOTION MEASURED DURING WAVE BASIN EXPERIMENTAL RUN 1. Plots (a-c) are 6 cm full scale. Each segment is 12.8 s long.

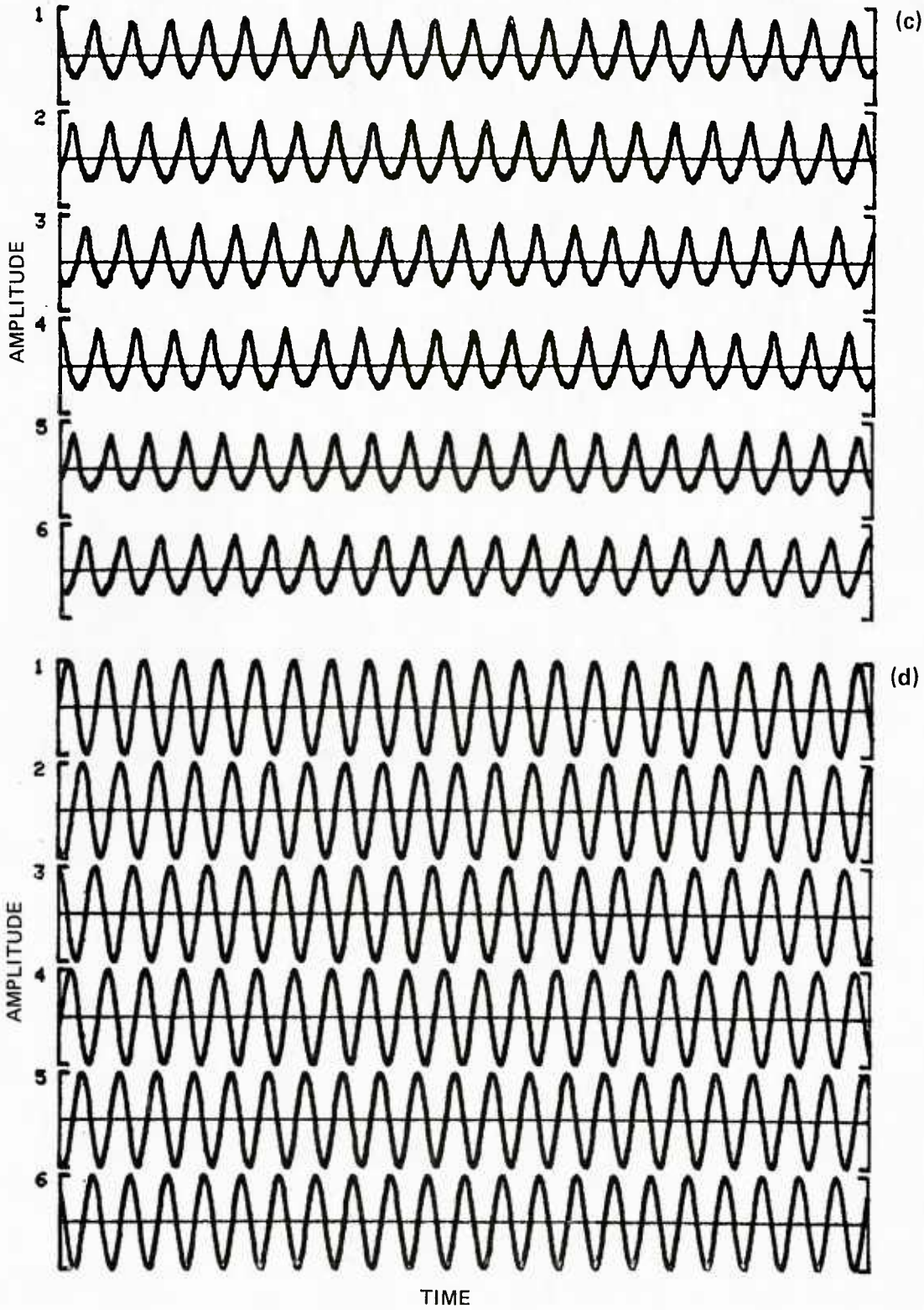

FIGURE A-4 (Concluded)

top to bottom in moving from one segment to the next. Each segment represents approximately 12.8 s of data. The time series plotted for the wave paddle motion is not calibrated for the absolute amplitudes of oscillation; however, the frequency, or wave-length, of the motion is properly scaled. The analog to physical displacement calibration transfer function for the LVDT output was computed and verified to be linear over the range of paddle motion applicable here. These laboratory experiments, however, were not specifically concerned with the relationship between the amplitude of the wave paddle motion and the resulting wave or run-up amplitudes. Instead, it was only necessary to identify the frequency distribution of the paddle motion, since the LVDT output was used for diagnostic and experimental control purposes. Thus, the wave paddle motion time series shown were not calibrated for amplitude in physical length units.

It is clear that the waveforms are clean and that no second harmonics are visible in the time series. Following each experimental run, the wave paddle was stopped and the water in the basin was allowed to return to the still condition. No cross waves, edge waves, standing waves, or other higher order phenomena were observed at any time during or following these experiments. Furthermore, the water in the basin stilled immediately once the paddle was stopped, and no basin seiching or other residual motions were observed.

Figure A-5 shows the power spectra computed from the time series for channels 1 to 4. PSD in centimeters squared/hertz is plotted as a function of frequency in hertz for each of the wave spectra [Figure A-5(a-c)]. The number above the spectral peak is the peak frequency of that spectrum as located by a cursor routine in the graphics subroutine of the computer program. The spectrum for the wave paddle [Figure A-5(d)] is uncalibrated with respect to amplitude, and the PSD has been plotted in digital units only; this does not affect the frequency distribution of the spectral energy. Each of these spectra were computed for a 512-point, 12.8-s FFT window with 31 equivalent degrees of freedom (Welch, 1967). A normalized (no power loss) Hanning window was applied to the debiased and

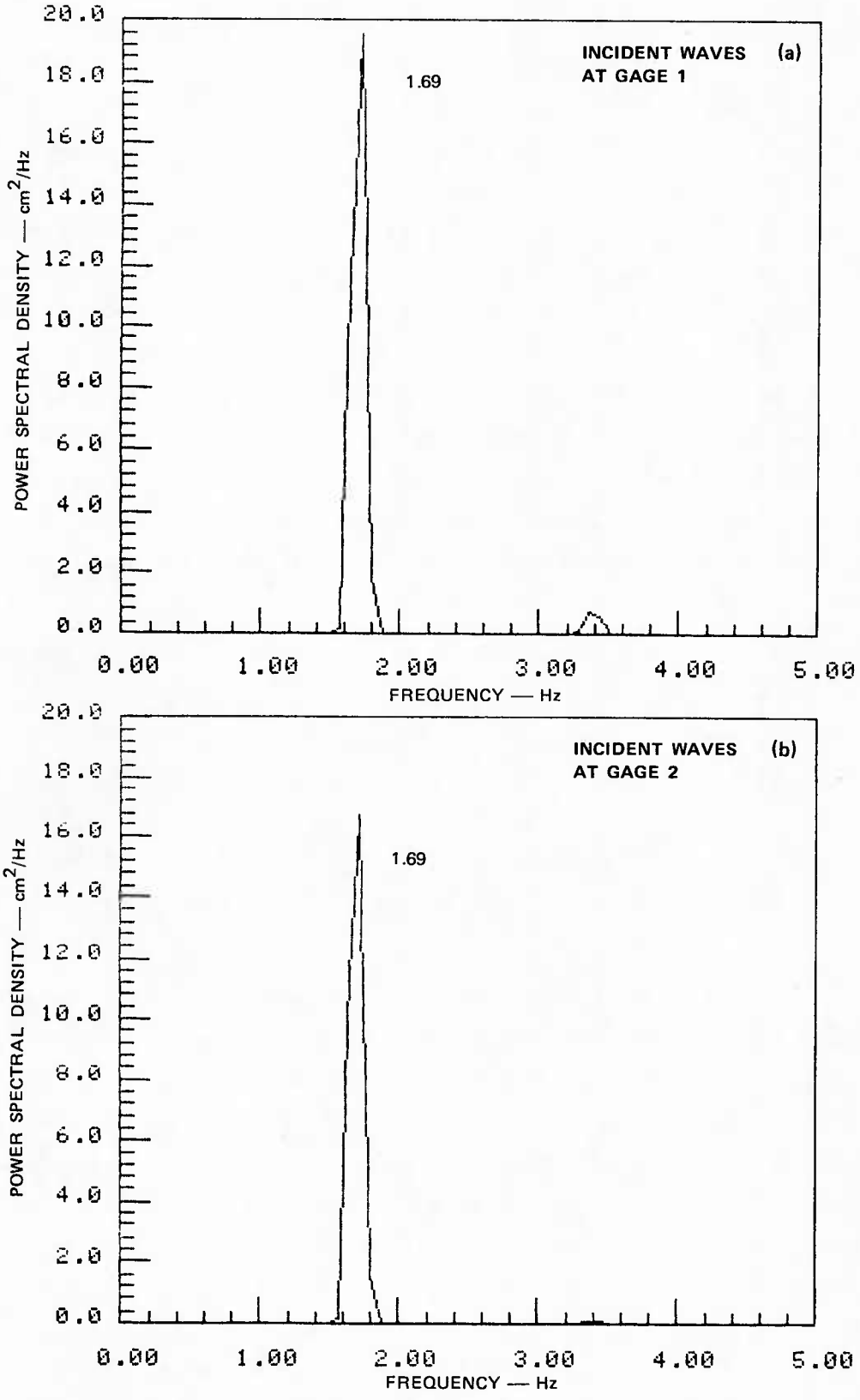

FIGURE A-5 INCIDENT-WAVE AND PADDLE MOTION SPECTRA MEASURED FOR WAVE BASIN EXPERIMENTAL RUN 1

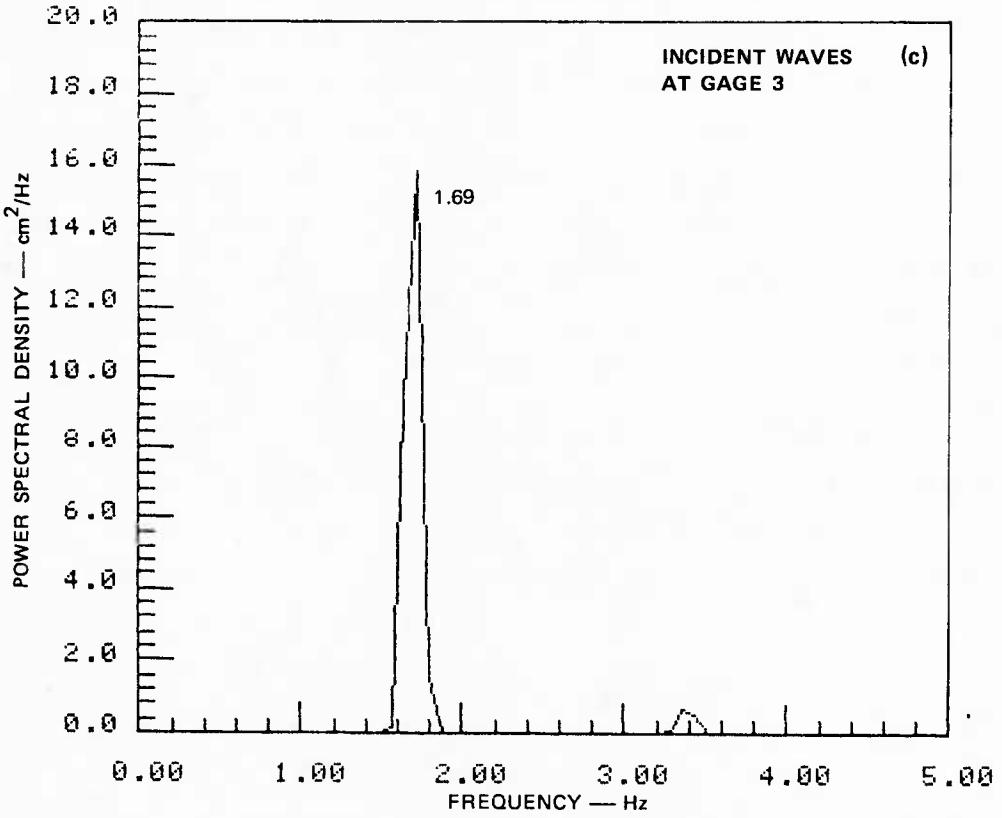

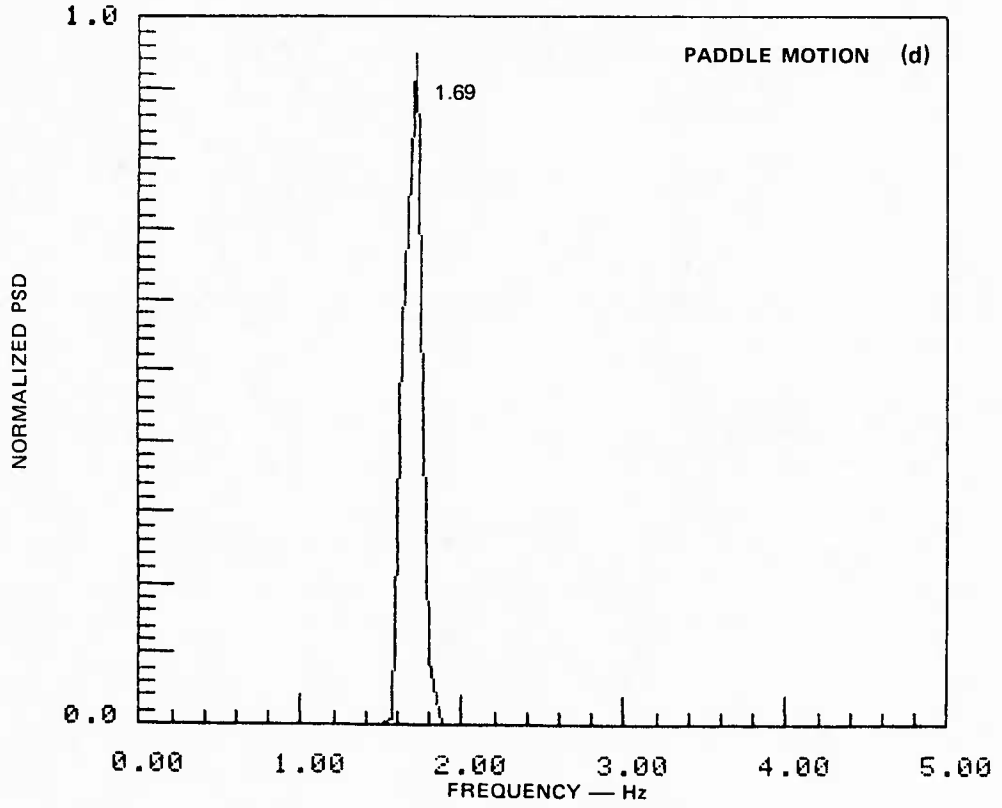

FIGURE A-5 (Concluded)

detrended time series, and a direct FFT was computed for each of the segments using a 50% overlap. The rms wave height computed based on the spectra is indicated in Table A-1. The computer program compared the power and the wave height computed for both the input time series and the spectrum, to verify that energy was conserved between the time series and the spectrum and that Parseval's rule was satisfied. The Nyquist frequency for these spectra is 20 Hz, and the frequency resolution is 0.078 Hz.

The corresponding run-up time series computed from the photographic record for Run 1 is shown in Figure A-6. These time series plots have been calibrated, are 20 cm full-scale, and are 18.3 s (256 points) long. The mean of the time series shows a positive offset due to the wave set-up effect. The run-up data were calibrated with respect to a still-water-level shoreline datum, and thus the wave set-up produces the observed positive bias. Wave set-up and its effect on the laboratory run-up measurements is discussed in Appendix B.

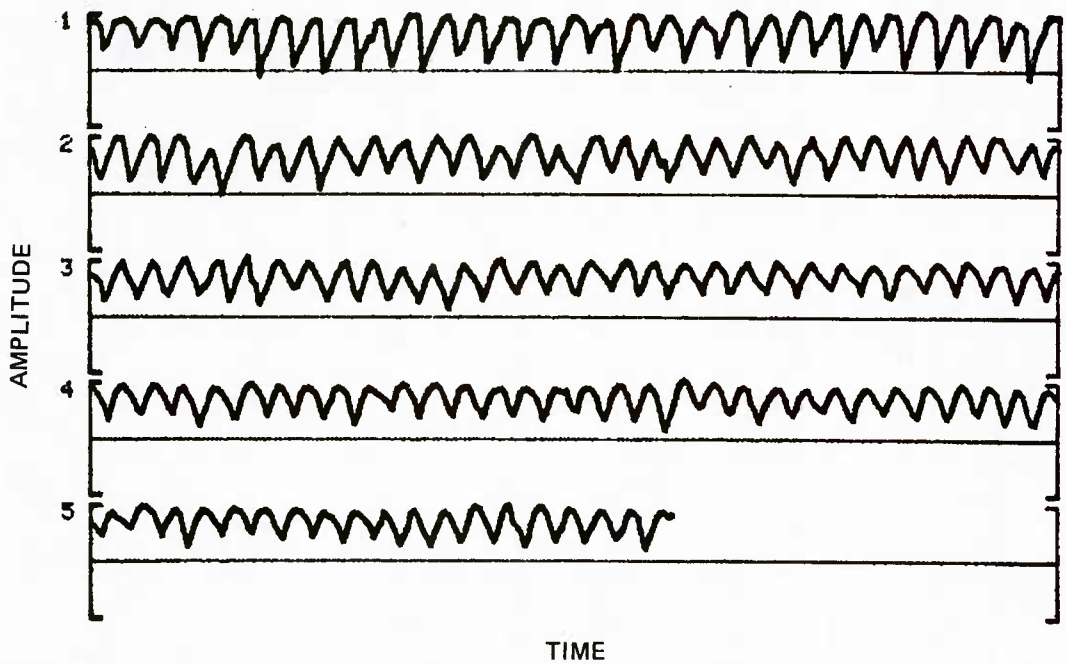

FIGURE A-6 RUN-UP TIME SERIES MEASURED DURING WAVE BASIN EXPERIMENTAL RUN 1. Plots are 20 cm full scale. Each segment is 18.3 s long.

Figure A-7 shows the run-up spectrum computed for the laboratory Run 1 data set. This spectrum was computed for 128-point, debiased, detrended, calibrated time series segments. A normalized Hanning window was applied to the time series, and a 50% overlap was used to produce the spectrum in Figure A-7 with 29 equivalent degrees of freedom. The frequency resolution of the wave spectra is 0.078 Hz, and the resolution of the run-up spectrum is 0.11 Hz. Within the resolution limits of the individual spectra, the peak frequency of the run-up spectrum is the same as the peak frequency of the corresponding incident-wave spectra (Figure A-5). Thus, here is a perfect example of a simple monochromatic wave train producing a corresponding monochromatic run-up of the same frequency on the beach face. No low-frequency energy was observed in the run-up measured in Run 1.

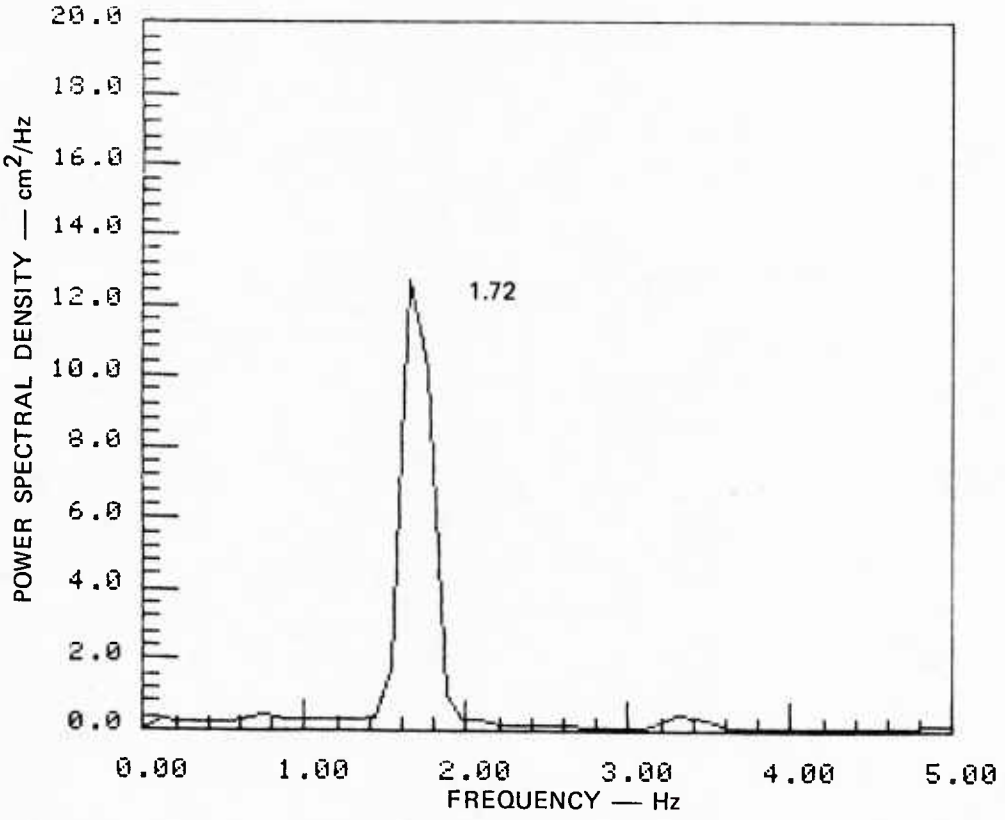

FIGURE A-7 RUN-UP POWER SPECTRUM MEASURED FOR WAVE BASIN EXPERIMENTAL RUN 1

b. Experimental Run 2

The same analysis procedures described for the Run 1 data were applied to the Run 2 data set. During experimental Run 2, however, the rheostat on the wave paddle control unit was oscillated by hand to simulate a multiple-frequency incident-wave field.

Figure A-8 shows the time series for the incident waves recorded at wave gages 1 to 3 and for the wave paddle motion. The incident-wave plots are calibrated, and each 12.8-s segment is plotted 8 cm full-scale. Figure A-9 shows the incident-wave spectra computed for the Run 2 laboratory data. The same spectral processing methods were used for both Run 1 and Run 2 incident waves and run-up. The Run 2 wave spectra have 21 equivalent degrees of freedom. The spectral peak frequency is indicated on each plot, and the rms wave heights measured at gage stations 1 to 3 [Figure A-9(a-c)] are shown in Table A-1.

The rheostat on the wave paddle control unit sets the speed of the motor and thus the frequency of the wave maker paddle motion. The amplitude, or stroke, of the paddle motion is preset before the experiment and cannot be adjusted dynamically while the paddle is operating. During the course of experimental Run 2, the rheostat knob was oscillated alternately clockwise and counterclockwise by hand at a nearly constant rate of approximately 2 Hz. The 2-Hz repetition rate can be verified in the time series shown in Figure A-8. The rheostat oscillation produced the effect of alternately slowing and then speeding the rotational motion of the paddle motor and consequently the horizontal motion of the wave maker paddle. The mechanical transfer mechanism for conversion of the motor's rotational motion to the wave paddle horizontal motion requires the paddle to traverse its full stroke in each cycle as preset prior to the experiment.

The effect of this manual rheostat oscillation is clearly evident in the incident-wave time series for Run 2 shown in Figure A-8(a-c) but is not so evident in the time series of the wave paddle horizontal motion shown in Figure A-8(d). However, a slight modulation of the paddle motion time series is evident upon very close examination, indicating

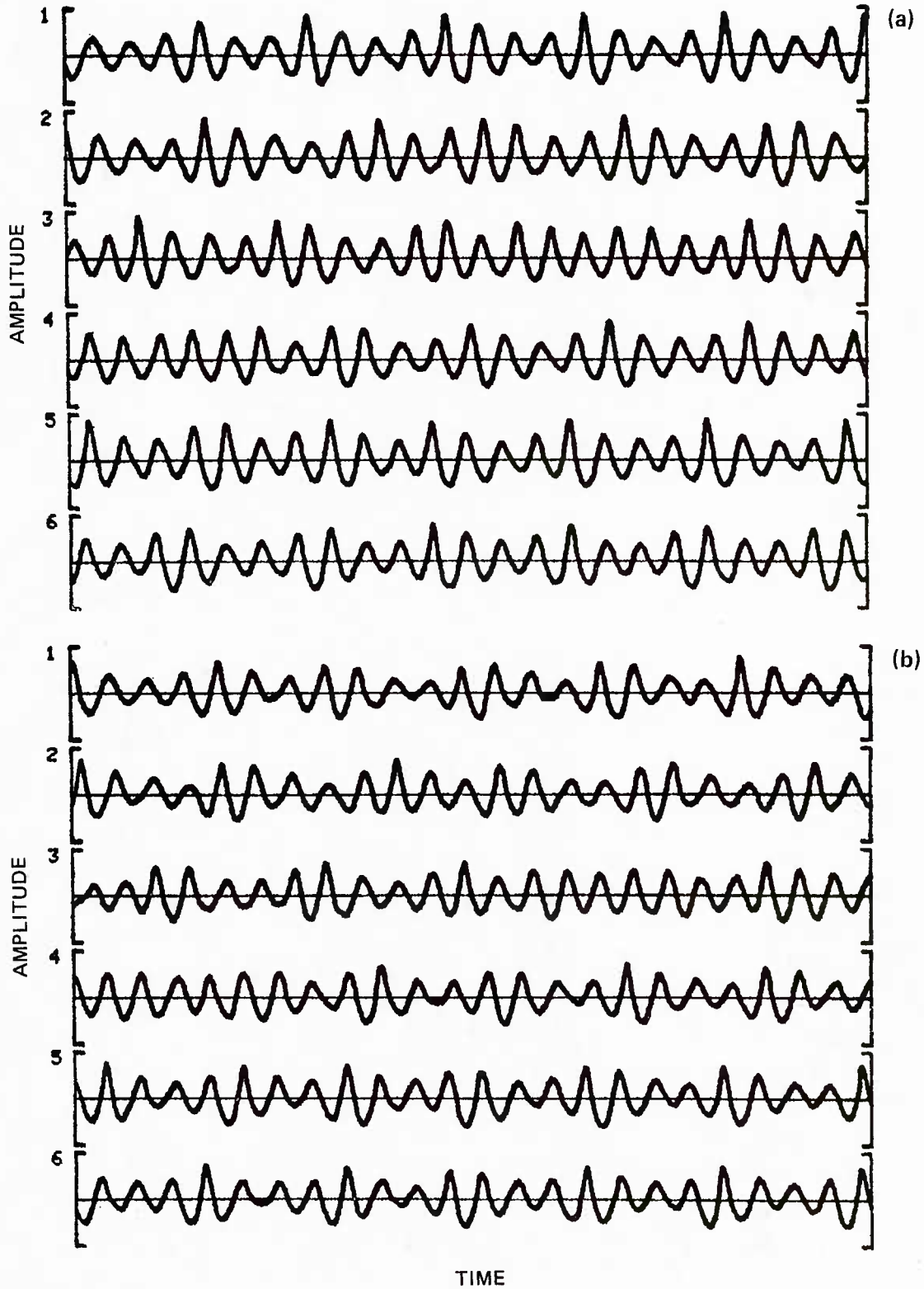

FIGURE A-8 TIME SERIES FOR (a-c) INCIDENT WAVES AND (d) PADDLE MOTION MEASURED DURING WAVE BASIN EXPERIMENTAL RUN 2. Plots (a-c) are 8 cm full scale. Each segment is 12.8 s long.

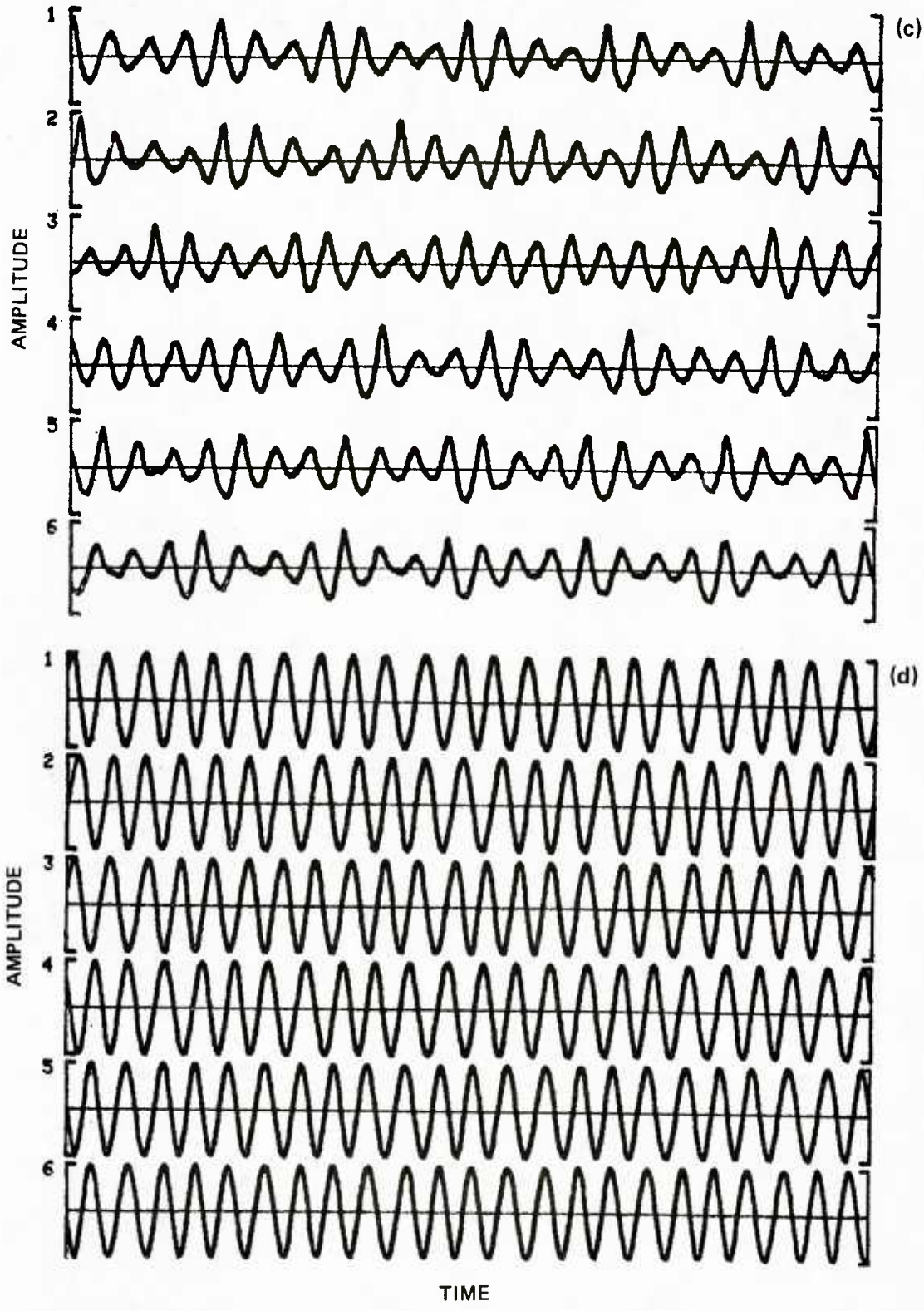

FIGURE A-8 (Concluded)

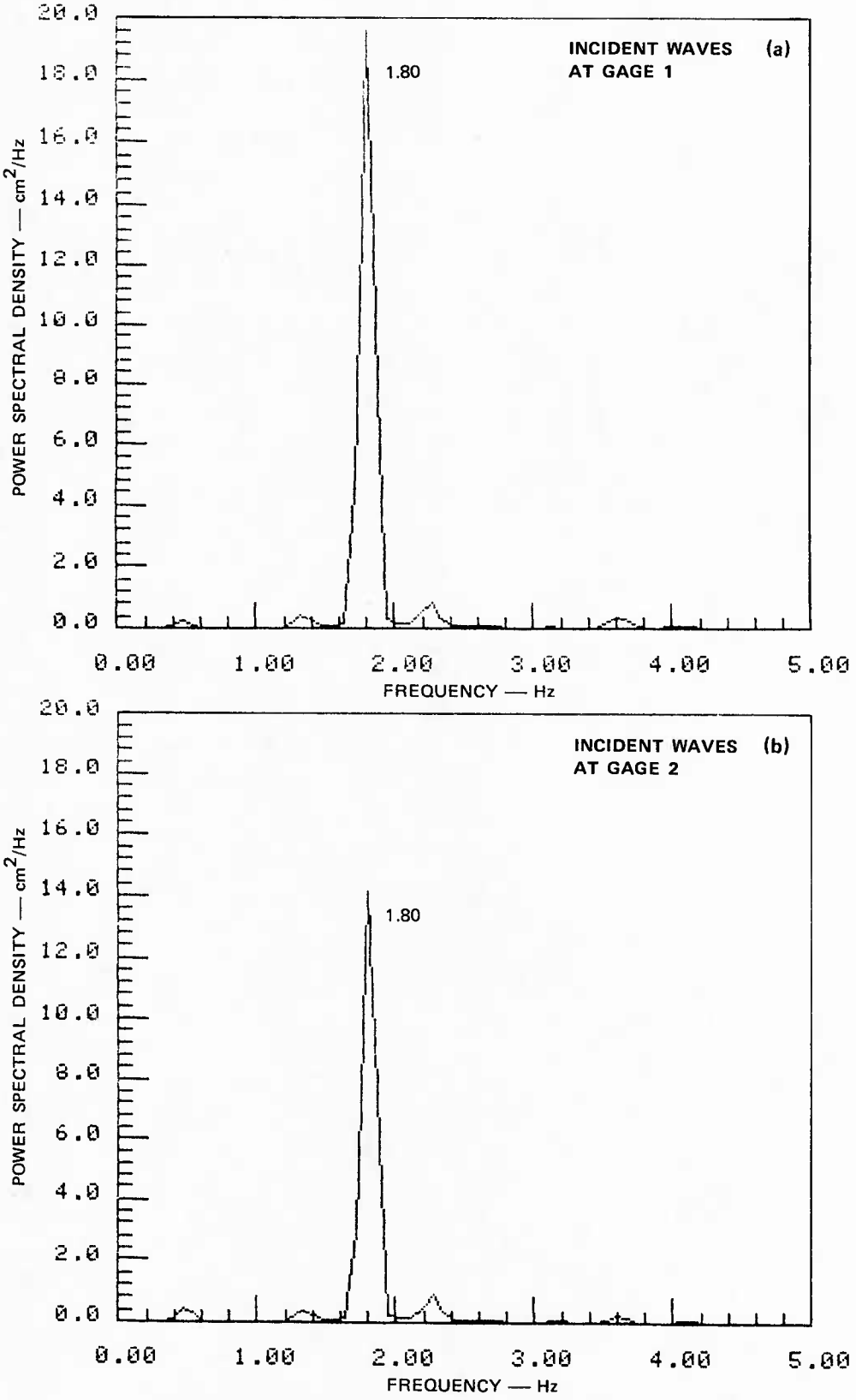

FIGURE A-9 INCIDENT-WAVE AND PADDLE MOTION SPECTRA MEASURED FOR WAVE BASIN EXPERIMENTAL RUN 2

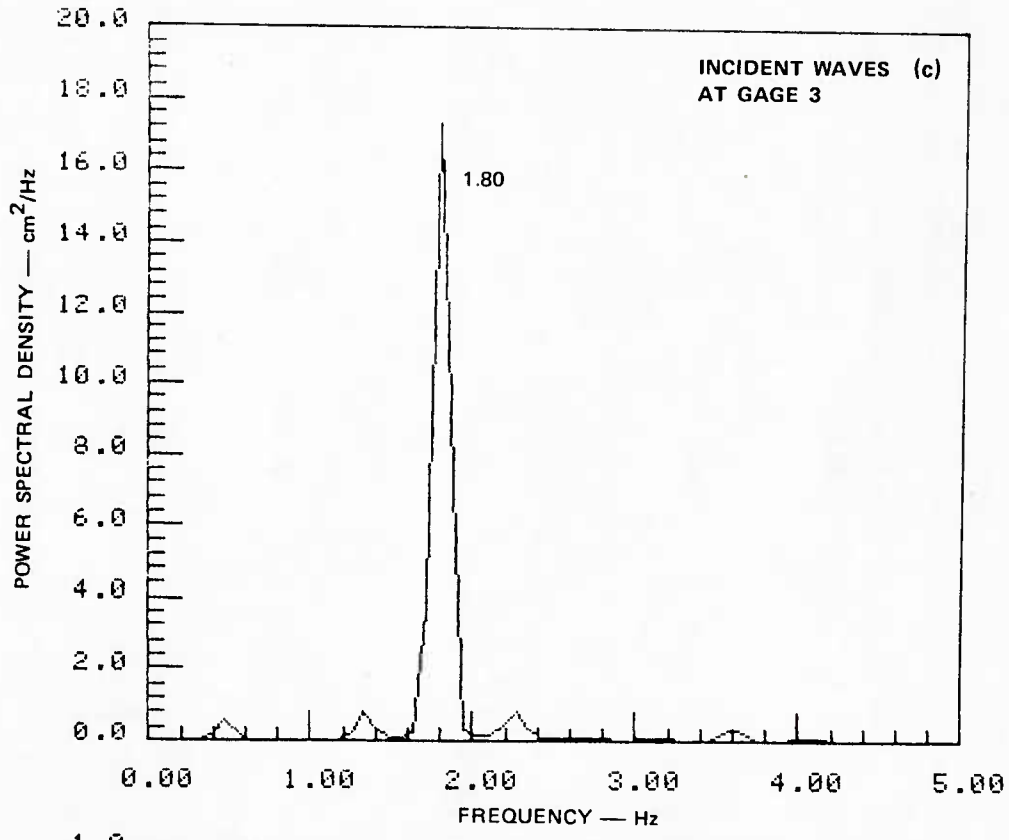

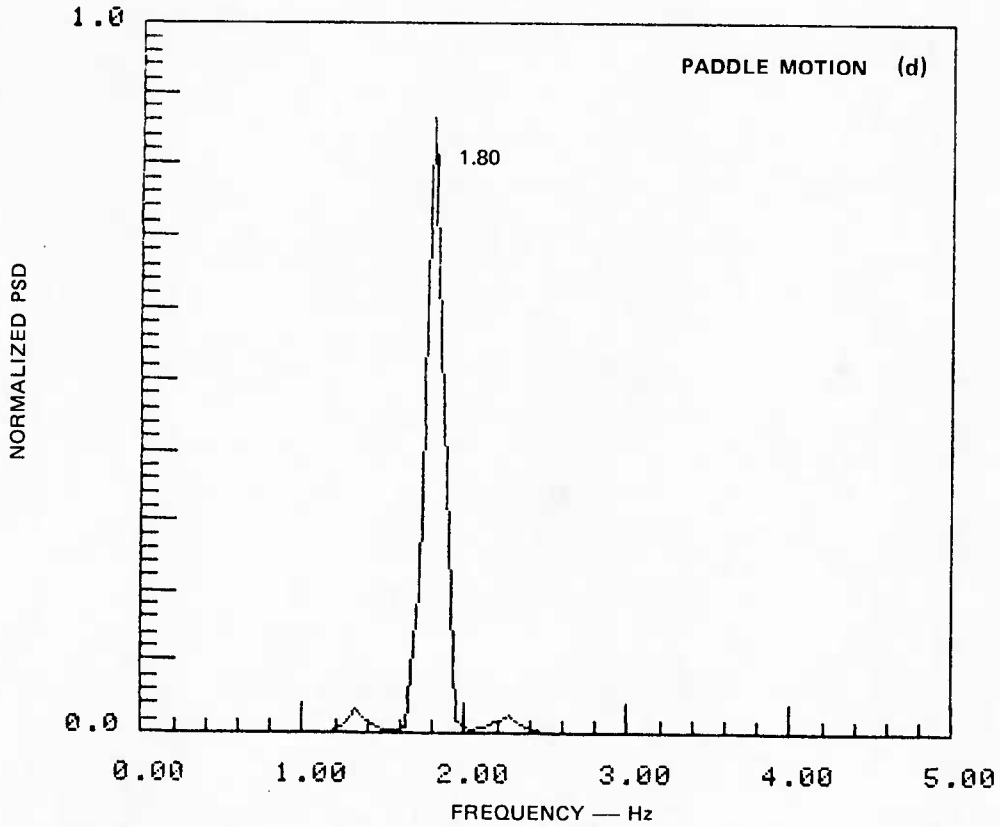

FIGURE A-9 (Concluded)

that although the amplitude of the paddle motion remained constant, a slight compression and expansion of the wavelength of the motion (i.e., a slight increase and decrease in the frequency of motion) occurred.

The LVDT used to measure the wave paddle horizontal motion was quite sensitive and measured the paddle motion accurately to approximately 1.6-V output/1 cm of paddle displacement. The fact that this manually induced modulation of the paddle motion frequency was not strongly represented in the paddle motion or incident-wave spectra (Figure A-9) is interesting but not entirely unexpected. The modulation effects in the spectra are manifested in the small sidebands surrounding the principal spectral peak. The spectral contributions of these sidebands are 14 to 16 dB ($dB = 10 \log P_{max}/P_{min}$) down in power from the predominant spectral peak; thus they contribute very little to the total wave spectral energy and, as will be shown, very little to the run-up spectrum.

Several different modes of spectral processing were applied to the paddle motion time series to verify that the relatively small spectral contribution of these sidebands (i.e., the spectral contribution due to the rheostat oscillation) was not an artifact of the spectral analysis. To test the possible effect of spectral window length, the FFT window was maximized at 2048 points per segment, which represented about 51.2 s of data. The 51.2-s FFT window thus included about 26 cycles of the modulation effect. The enlarged FFT window enhanced the spectral resolution, but the power in the sidebands remained unchanged. Other spectral windows were tried, as were different combinations of debiasing, detrending, and windowing. A completely different FFT algorithm was also applied to verify that all processing of these time series data was correct and completely reproducible. In all cases, Parseval's Rule was satisfied, and the power in the calibrated raw time series data agreed to within about 1% of the power computed from the spectrum. The sidebands are real and are not due to spectral leakage or other artifacts of the spectral analysis.

The corresponding run-up time series for Run 2 is shown in Figure A-10. The individual calibrated time series segments are continuous in time

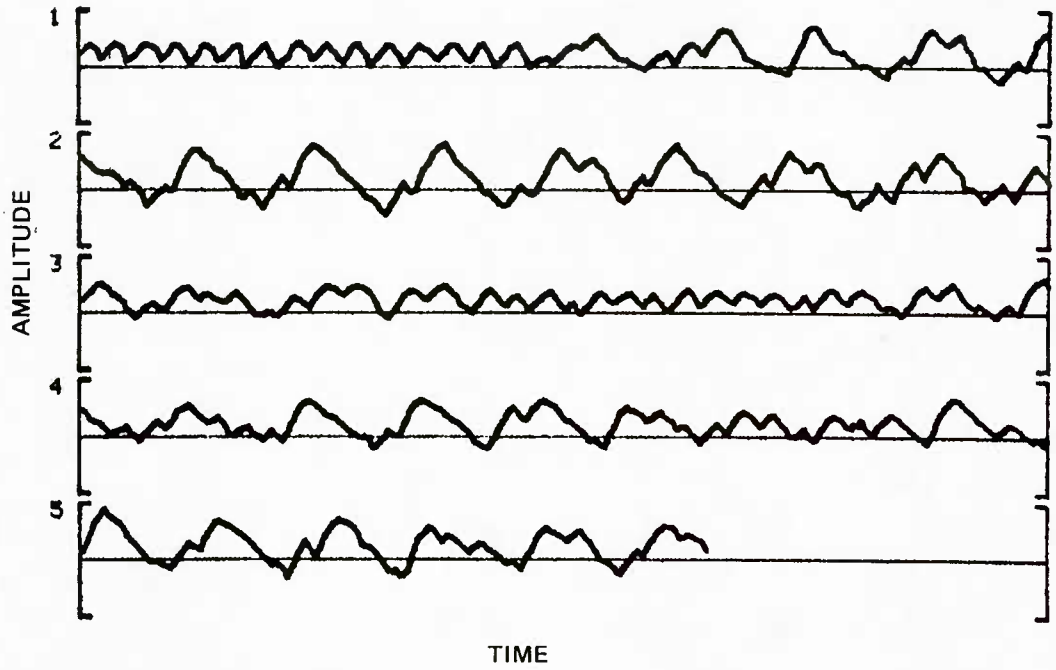

FIGURE A-10 RUN-UP TIME SERIES MEASURED DURING WAVE BASIN EXPERIMENTAL RUN 2. Plots are 50 cm full scale. Each segment is 18.3 s long.

and are plotted 50 cm full-scale. Each plotted segment is 256 points long and represents about 18.3 s. Time series segment 1 in the figure shows the run-up amplitudes on the beach face being influenced by the manual manipulation of the rheostat. Time series segment 3 in the figure shows an unexplained period of higher-frequency, lower-amplitude run-up excursions. Whether this is a real transient phenomenon or simply another manifestation of rheostat manipulation is unclear.

The run-up power spectrum computed from these Run 2 data is shown in Figure A-11. This spectrum was computed using 128-point FFTs with 50% overlap, resulting in 29 equivalent degrees of freedom. The frequency resolution is 0.11 Hz, and the Nyquist frequency is 7 Hz. It is striking to note that only a very small percentage of the run-up spectral energy is evident at the 1.80-Hz peak frequency of the incident waves. Instead, the run-up spectral peak frequency is 0.44 Hz, which is lower than the predominant incident-wave peak frequency by a factor of approximately four. A cursory inspection of the incident-wave time series alone would

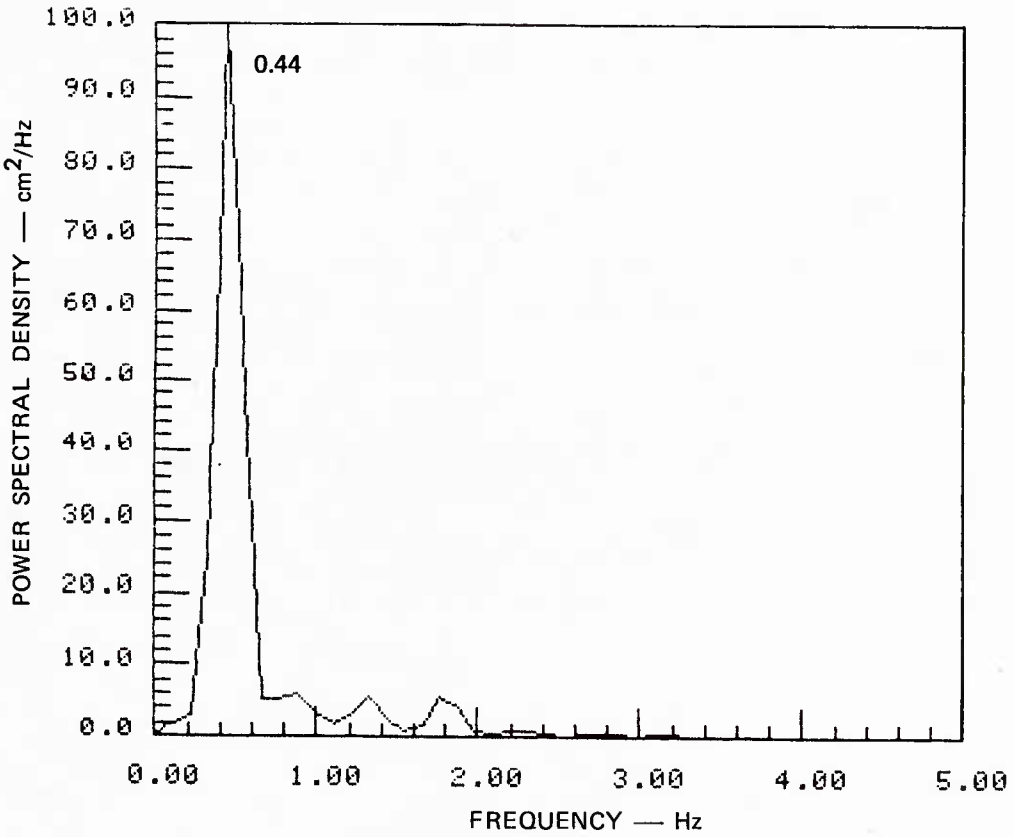

FIGURE A-11 RUN-UP SPECTRUM MEASURED FOR WAVE BASIN EXPERIMENTAL RUN 2

lead one to expect a strong peak in the run-up spectrum around 0.45 Hz. Based on the measured incident-wave spectra, however, one might have expected to observe more energy in the run-up spectrum at 1.80 Hz than was actually measured. This is an important result. The Run 2 data demonstrate the need to exercise care when estimating the expected characteristics of wave run-up based on offshore incident-wave statistics. Apparently, only the longer waves generated by oscillating the rheostat with approximately a 2-s cycle affect the run-up by cancelling or overriding the run-up caused by the smaller waves. This effect is not unusual, but its dominance in this particular instance is surprising. The 0.44-Hz peak in the run-up spectrum does not match any of the frequencies expected for basin seiching modes 1 to 4 as described by Wiegel (1964) and should be due only to the run-up produced by the incident waves generated by

the wave paddle. The wave basin stilled immediately when the wave generator was stopped, and no 0.4-Hz residual seiching motions were observed.

4. Laboratory Conclusions

Run 2 of the three laboratory experiments showed low-frequency run-up on the beach. The other two experiments demonstrated monochromatic waves generating monochromatic run-up at the incident-wave frequency. While the Run 2 experiment showed the run-up spectral peak as the second subharmonic of the incident-wave frequency, the data suggest that this was due to the run-up of the longer waves overriding the shorter-wave run-up. Although this particular laboratory experiment did not demonstrate the swash resonance phenomenon, it did illustrate the mechanism of low- and high-frequency incident-wave forcing of low-frequency wave run-up on a beach. Additionally, the Run 2 experiment showed the extent to which long waves can dominate the run-up on a beach, demonstrating the reason it might be more effective to study swash dynamics on beaches exposed only to narrow-band, nearly single-component wave fields.

Appendix B

WAVE SET-UP EFFECTS ON THE LABORATORY RUN-UP MEASUREMENTS

Wave set-up, and correspondingly, wave set-down, are positive and negative changes in the mean water level (MWL) caused by the presence of the incident surface waves. As shown in Figure B-1, the net result is a depression of the MWL just seaward of the break point of the incident waves and a superelevation of the MWL shoreward of the break point. The wave set-up is a maximum at the shoreline, and the run-up amplitude fluctuations are superimposed on this displaced MWL. These changes in the mean fluid surface elevation may be explained in terms of the conservation of momentum flux associated with the shoaling and breaking of the incident waves. Longuet-Higgins and Stewart (1963) and (1964), Bowen et al. (1968), Battjes (1974), and more recently Guza and Thornton (1981) present in detail the theoretical background for wave set-up. The principal details of these studies as applicable to the run-up measurements described in this report are summarized in the following, and estimates of the wave set-up during the laboratory experiments are made.

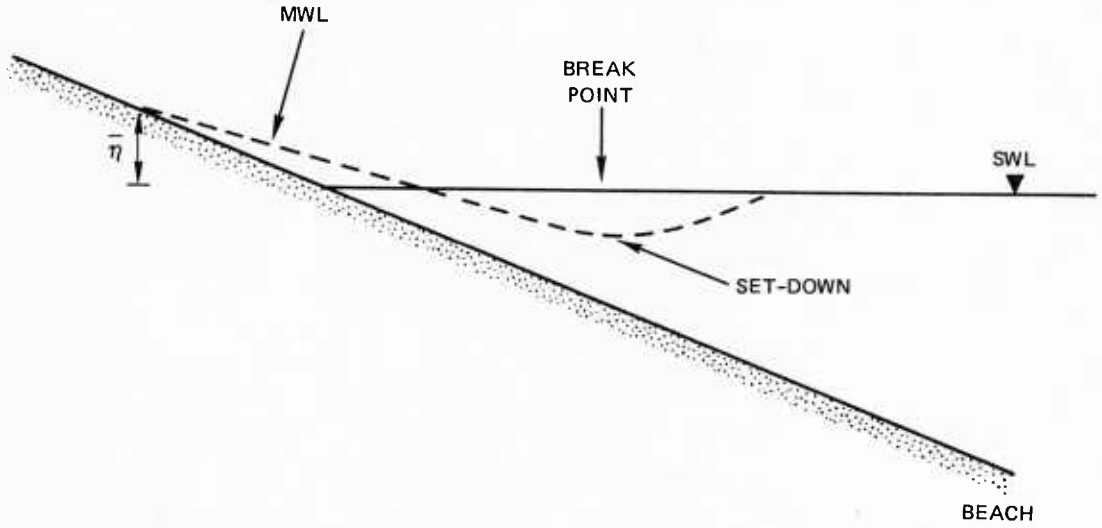

FIGURE B-1 WAVE SET-UP EFFECT DISPLACES MEAN WATER LEVEL (MWL) RELATIVE TO STILL WATER LEVEL (SWL). The maximum set-up, $\overline{\eta}$, occurs at the shoreline.

Longuet-Higgins and Stewart (1964) describe the excess flow of momentum due to the presence of the waves as radiation stress. This has also been termed "wave thrust." For applications of this theory to estimation of wave set-up and the resultant effects on the run-up, we are primarily interested in the x component of the radiation stress, S_{xx}. From linear progressive wave theory, the velocity potential is given by:

$$\phi = \frac{a\sigma}{k} \frac{\cosh k(z+h)}{\sinh kh} \cos(kx + \sigma t) \tag{B-1}$$

where z is the surface elevation, $k = 2\pi/L$ (L is wavelength), $\sigma = 2\pi/T$ (T is the wave period), h is the still water depth, and a is the wave amplitude. The corresponding x and z components of ϕ are:

$$u = \frac{\partial \phi}{\partial x} = a\sigma \frac{\cosh k(z+h)}{\sinh kh} \cos(kx - \sigma t)$$

$$w = \frac{\partial \phi}{\partial z} = a\sigma \frac{\sinh k(z+h)}{\sinh kh} \sin(kx - \sigma t) \tag{B-2}$$

where x is the horizontal coordinate perpendicular to the shoreline, and z is the vertical coordinate with origin at the MWL. The flux of horizontal momentum across a unit area of vertical plane in an undisturbed fluid layer of uniform depth is:

$$\int_{-h}^{0} p_o \, dz = 0 \tag{B-3}$$

where $p_o = -\rho gz$ is the hydrostatic pressure. If a wave is superimposed on the fluid surface, the instantaneous flux of horizontal momentum is $p_w + \rho u^2$, where p_w is the instantaneous pressure due to the waves, and ρu^2 represents a physical flux of momentum, or the dynamic pressure. The total flux of momentum across the vertical plane is then:

$$\int_{-h}^{\eta} (p_w + \rho u^2)\, dz \quad . \tag{B-4}$$

The x component of the radiation stress, S_{xx}, is the time-averaged value of Eq. (B-4):

$$S_{xx} = \frac{1}{T} \int_0^T \int_{-h}^{\eta} (p_w + \rho u^2)\, dz\, dt \tag{B-5}$$

where $p_w = p - p_o$, and p is the total pressure. Eq. (B-5) may be rewritten:

$$S_{xx} = \frac{1}{T}\left[\int_0^T \int_{-h}^{\eta} \rho u^2 dz + \int_{-h}^{0} (p-p_o) dz + \int_0^{\eta} p dz \right] dt \quad . \tag{B-6}$$

Longuet-Higgins and Stewart (1964) show that the first term in Eq. (B-6) is simply the Reynolds stress, ρu^2, integrated from the bottom to the free surface. The second term in Eq. (B-6) is the change in mean pressure within the fluid due to the presence of the waves. Using Eq. (B-2) they show that the first and second terms in Eq. (B-6) reduce to $\rho g a^2 kh / \sinh(2kh)$. Component 3 of Eq. (B-6) is equal to the potential energy density of the waves, i.e., one-half of the total energy; $E/2 = 1/4\ \rho g a^2$. The x component of the radiation stress is then:

$$S_{xx} = E\left[\frac{2kh}{\sinh\ 2kh} + 1/2 \right] \tag{B-7}$$

where in shallow water $S_{xx} = 1.5\ E$.

Bowen et al. (1968) used Eq. (B-7) and, through momentum balance, argue that:

$$\frac{d\ S_{xx}}{dx} + \rho g\ (\overline{\eta} + h)\ \frac{d\overline{\eta}}{dx} = 0 \quad , \tag{B-8}$$

where the difference between the SWL in the absence of waves and the mean sea level when waves are present is given by:

$$\bar{\eta} = \frac{-H^2 k}{8 \sinh (2kh)} \quad . \tag{B-9}$$

Bowen shows that Eq. (B-9) can be expressed as:

$$\frac{d\bar{\eta}}{dx} = -K \frac{dh}{dx} \quad , \tag{B-10}$$

which relates the set-up gradient to the beach slope and the ratio of the wave height to water depth at the break point. In Eq. (B-10) the still water depth is given by $h = x \tan\beta$ for beach slope β and:

$$K = \frac{1}{1 + (8/3\gamma^2)} \quad , \tag{B-11}$$

where

$$\gamma = \frac{H}{\bar{\eta} + h} \quad . \tag{B-12}$$

Battjes (1974) shows that these simple monochromatic theories can be approximated by:

$$\bar{\eta}_{max} = 0.3 H_b \gamma \tag{B-13}$$

where γ is given in Eq. (B-12), H_b is the breaker height, and $\bar{\eta}_{max}$ is the maximum set-up that occurs at the shoreline.

Eq. (B-13) was used to estimate the set-up expected for the laboratory wave basin run-up in experimental Run 1. The time series plots for the laboratory run-up measurements presented in Figures A-6 and A-10 show a positive offset with respect to the SWL datum. The calibration transfer function for the laboratory run-up measurements was derived by using the stationary shoreline, still-water condition as the zero reference datum. During the experiment, the incident waves produced a wave set-up in the wave basin that displaced the mean shoreline by a positive

distance in the onshore direction. The run-up amplitude fluctuations on the beach face oscillate about this new, dynamically displaced mean shoreline. It is difficult to measure exactly the amount of set-up generated during these experiments. As shown in the field experiments, the run-up and backwash are not truly symmetric about the mean shoreline. Generally, the upslope displacement of the shoreline during the run-up excursion is greater than the downslope displacement of the shoreline during the backwash phase of the swash cycle. The set-up may be roughly estimated to first order, however, by computing the mean shoreline position from the run-up time series, i.e., the mean run-up amplitude, and comparing this to the location of the SWL shoreline location measured before the experiment was started.

For the run-up shown in Figure A-6, the maximum run-up excursion was approximately 10.7 cm, the minimum was -1.5 cm, and the mean run-up computed over the entire time series was 7.0 cm relative to the SWL shoreline position before the wave paddle was started. To first order, Eq. (B-12) may be approximated by $\gamma = H_b/h$. The location of wave-breaking on the laboratory beach was identified in the photographic time series taken to record the run-up on the beach face. The depth of breaking, h, was estimated from the location of the breaker zone on the beach. The ratio of breaker height to depth of wave breaking, γ, as estimated from the laboratory data was approximately 1.0, this value showing good agreement with Guza and Thornton (1981). The wave height at breaking was estimated from the incident-wave time series measured in the laboratory, and the maximum set-up at the shoreline, $\overline{\eta}_{max}$, estimated using Eq. (B-13) was approximately 8.6 cm. This shows reasonable order-of-magnitude agreement with the mean run-up of 7.0 cm measured in the laboratory for Run 1.

Appendix C

RUN-UP MODEL SIMULATIONS

The field observations of offshore incident waves and swash on the beach revealed the typical sequence of a wave plunging near the shoreline and the resulting bore moving shoreward. The bore was subsequently converted to a rarefaction wave, or wave of depression, moving up the beach face as run-up. This cycle was usually repeated before the swash cycle from the previous wave was completed. Thus, two or more waves were generating run-up on the beach face simultaneously, with one run-up layer moving over the top of the previous run-up layer.

A rectilinear motion run-up model was developed to demonstrate low-frequency run-up generation on the beach face by swash resonance in the absence of low-frequency forcing by the incident or reflected wave field. The run-up was modeled as multiple layers on the beach permitted to travel up and down the beach face at any time, as shown schematically in Figure C-1. Although mass conservation was not considered explicitly in the model, momentum mixing was approximated by averaging the velocity between adjacent layers. The lowest layer on the beach, adjacent to the beach face, was averaged with the zero velocity of the stationary beach surface. The successive layers above the layer adjacent to the beach face would experience less drag if overriding another layer also moving up the beach slope. Conversely, if a layer moving up the beach slope were to override a backwash layer moving down the slope, it would be expected to experience additional drag due to the associated negative velocity gradient. Computation of layer velocity and displacement were averaged over each time step during the simulation, working from the beach surface upward through the layers.

The model was developed with the following constraints:

- The beach slope is uniform and constant.
- The beach is impervious and percolation effects are not considered.

- The run-up is initiated after the wave breaks with initial velocity, C, calculated from solitary wave theory, i.e., $C = \sqrt{gH}$, where H is the depth of the water column and g is the gravitational acceleration.
- Deceleration of the run-up is caused by gravity and the velocity gradient with the underlying backwash.
- Frictional effects between the beach and the run-up and between different run-up layers are ignored.
- Deceleration of the backwash to zero occurs at a specified horizontal distance from the mean still water line.
- The waves and run-up are normal to the shoreline.
- There is no collision of the backwash and run-up.
- Mass effects between layers are neglected.

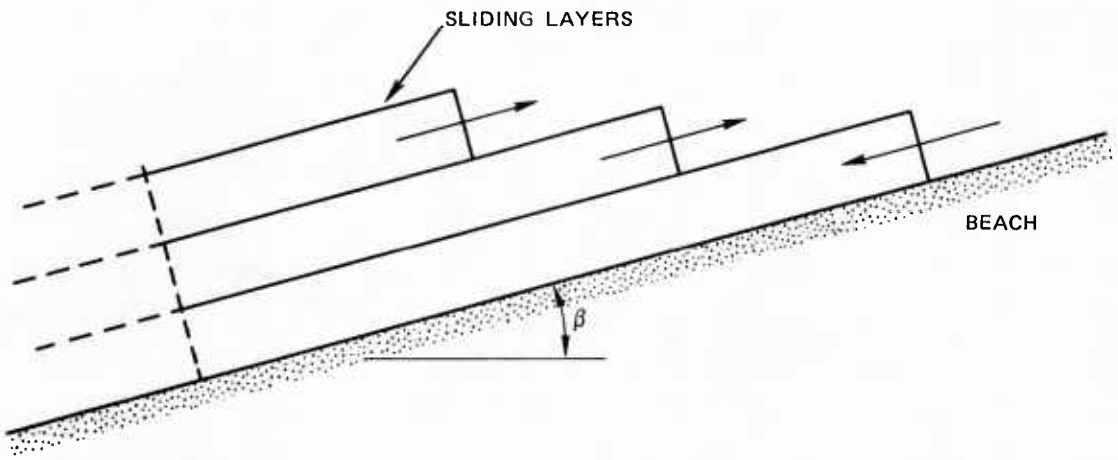

FIGURE C-1 SCHEMATIC SHOWING RUN-UP MODEL SLIDING LAYERS

The equation describing the position in time of the leading edge of a given run-up layer on the beach face is:

$$x(t) = Ct - 1/2\ gt^2 \tan\beta \qquad \text{(C-1)}$$

where C is the initial velocity, β is the beach slope, t is time, and g is the acceleration of gravity. The velocity of a layer $V(t) = dx(t)/dt$ is:

$$V(t) = C - gt \tan\beta \quad . \qquad \text{(C-2)}$$

Eq. (C-1) and (C-2) are used to compute the position and velocity of the leading edge of the run-up on the beach face at each time step in the simulations. V(t) was computed at times t and t + delta t for each adjacent layer, and the subsequent velocities and displacements were then averaged across the time step and between layers as described above.

The initial upslope motion of a new run-up layer is controlled by the frequency and height of the model input incident waves. The number of layers on the beach face at any time is controlled by the frequency of the incident waves. A new layer is initiated each time a wave is incident at the shoreline. The model has been run using two different forcing modes. In the first case, the actual measured incident-wave time series was used to drive the model and to control the initiation of the upslope layer motion. A new layer was started each time a wave crest was encountered in the measured time series. The second case used internal simulation of the incident-wave time series. The principal incident-wave heights and frequencies were inputs to the model. As time ran continuously in the model simulation, a new layer was introduced as controlled by the frequencies (periods in seconds) and heights of the principal waves. For example, if two incident-wave frequencies of 0.1 and 0.2 Hz (periods of 10 s and 5 s, respectively) were input to the simulation, then every 5 s and every 10 s new layer(s) were initiated; i.e., every 5 s one new layer was added, and every 10 s two new layers were added. The initial upslope velocity of each layer, C, was based on the height of the wave used as an estimate of its corresponding bore height. The spectral peak frequencies of the actual measured incident-wave spectra were used to drive the model.

A number of different incident-wave forcing functions have been considered: (1) single, monochromatic waves of constant amplitude; (2) two or more wave trains of different frequencies and amplitudes; (3) the incident-wave time series measured at the Alameda Beach; (4) several incident-wave conditions extracted from the open literature; and (5) the predominant incident-wave frequencies and heights estimated from the Coyote Point data. These forcing functions controlled the input

frequency and initial velocity for the model run-up layers. The model generates a time series describing the motion of the leading edge of the run-up. The run-up power spectrum is then computed from this simulated time series of the run-up and may be compared to the measured run-up spectrum computed from the measured field or laboratory data.

The first four cases described here illustrate comparisons between the model-simulated run-up and the run-up measured at the Alameda Beach. A 6° beach slope was used for the first four model runs. Four distinct model cases based on the frequencies and wave heights summarized in Table C-1 were considered.

Table C-1

INPUT FORCING CONDITIONS USED TO DRIVE THE RUN-UP MODEL

Case	Model Incident-Wave Forcing Condition			
	No. of Components	Height (cm)	Frequency (Hz)	Period (s)
1	1	12.5	0.59	1.69
2	1	19.5	0.44	2.27
3	2	12.5 19.5	0.59 0.44	1.69 2.27
4	Multiple	Measured time series input		

First, a uniform wave train with a wave height of 12.5 cm and frequency of 0.59 Hz was used to drive the run-up model. The resulting power spectrum for the modeled run-up shown in Figure C-2(a) reveals run-up energy concentrated at the incident-wave frequency as well as at multiple lower frequencies. Similar results were obtained from the model for incident waves of 0.44-Hz frequency and height of 19.5 cm, as shown in Figure C-2(b). In this instance, however, in addition to the peak in the run-up spectrum observed at the incident-wave frequency, the energy at lower frequencies is greater than the low-frequency energy shown in

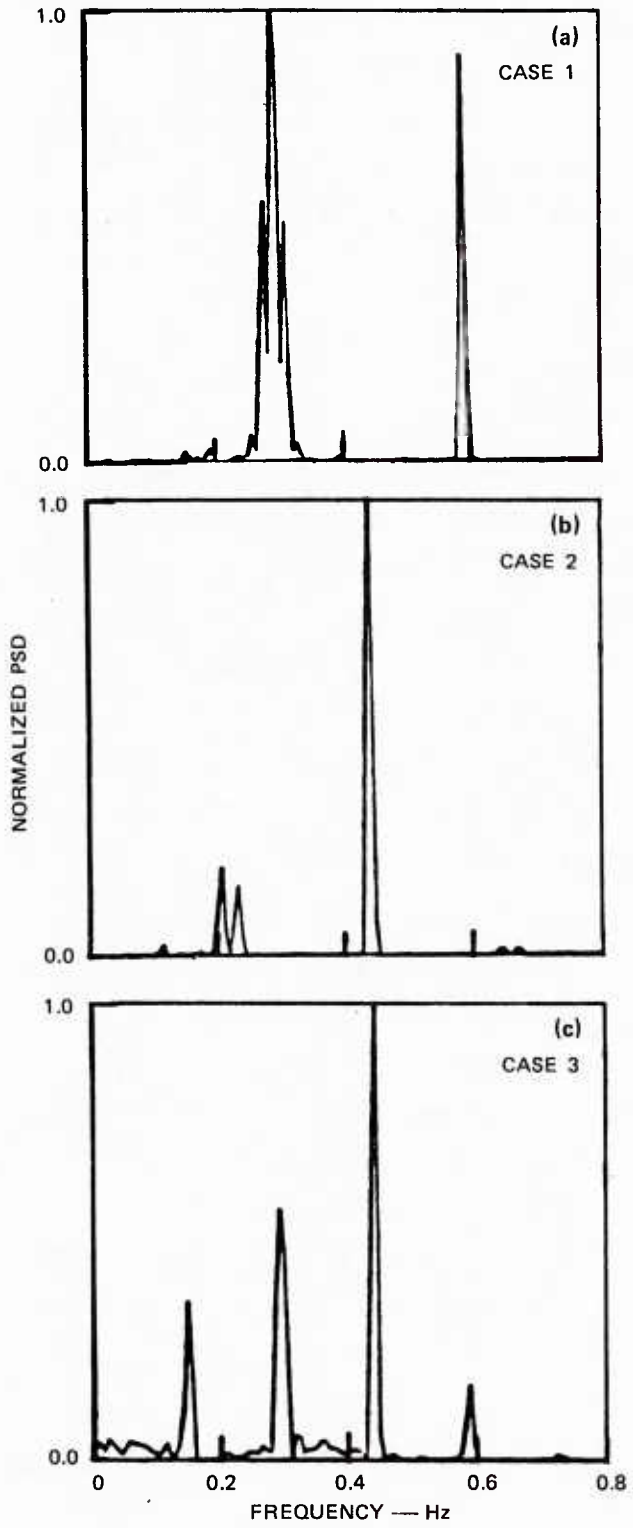

FIGURE C-2 SIMULATED RUN-UP SPECTRA FOR THREE DIFFERENT TYPES OF FORCING FUNCTIONS

the run-up spectrum for the 0.59-Hz incident-wave forcing conditions. The third case, shown in Figure C-2(c), illustates the simulated run-up spectrum computed by combining the two wave trains of cases 1 and 2. Significant run-up spectral energy is observed at the incident-wave frequencies of 0.44 Hz and 0.59 Hz and at two lower frequencies of 0.15 Hz and 0.29 Hz.

In these three cases, discrete wave frequencies and heights were used as the model forcing functions. The time series actually measured in the field was used to drive the model simulation for case 4, and the results are shown in Figure C-3. The model spectrum shows low-frequency energy in the run-up spectrum similar to that observed in the Alameda Beach data. The predominant run-up spectral peak is located at about 0.37 Hz, and low-frequency energy is observed at approximately 0.21 and 0.24 Hz as indicated on the plot. Additional low-frequency energy surrounds the 0.21- and 0.24-Hz peaks, including a peak of 0.08 Hz. No high-frequency run-up spectral energy is observed in the simulated spectrum. Recall that the peaks in the Alameda run-up spectrum shown in Figure 15 were located at 0.08, 0.25, and 0.37 Hz.

The run-up model was run for each of the incident-wave conditions used in the laboratory, using the laboratory beach slope. In each case, the model predicted that the first subharmonic should be observed in the run-up spectrum. Clearly, this was not the case. Recall that sidebands were observed surrounding the peak incident-wave frequency in laboratory experimental Run 2. These contributions to the incident-wave field were included as independent input frequencies in an additional test of the model. These did not alter the result. The first subharmonic still remained the predominant peak in the simulated run-up spectrum.

A limited number of papers in the open literature report results of laboratory and field run-up studies showing both incident-wave conditions and the resulting run-up. Figure C-4 shows the swash profile spectrum and the incident-wave spectrum measured by Sonu et al. (1974), as well as the simulated run-up spectrum generated by using the run-up model. Sonu's data were recorded at a dissipative, nearly flat (1:45)

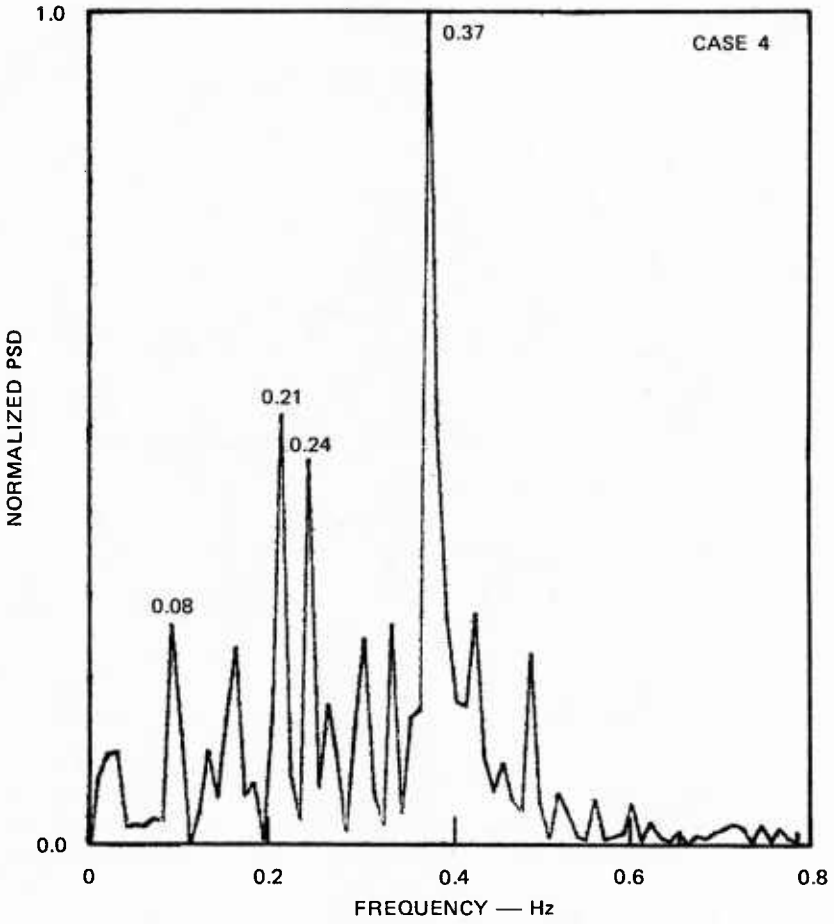

FIGURE C-3 SIMULATED RUN-UP SPECTRUM COMPUTED USING THE MODEL AND THE MEASURED INCIDENT-WAVE TIME SERIES AS MODEL FORCING FUNCTION

Florida beach. For an additional test of the run-up model, Sonu's incident-wave conditions were input as the model forcing function. The peak frequencies in Sonu's incident-wave spectra are approximately 0.22 and 0.11 Hz. The incident-wave heights were approximated at these frequencies by integrating Sonu's wave spectrum. The two wave frequencies and heights of 0.11 Hz, 16 cm, and 0.22 Hz, 11 cm, respectively, were input as the forcing conditions for the run-up model simulation, and Sonu's beach slope was used. Figure C-4(c) shows the resulting simulated run-up spectrum computed by using the model; spectral peaks are observed at 0.04, 0.07, and 0.11 Hz. The predominant peaks in Sonu's run-up spectrum, shown in Figure C-4(a), are also located at 0.04, 0.07, and 0.11 Hz.

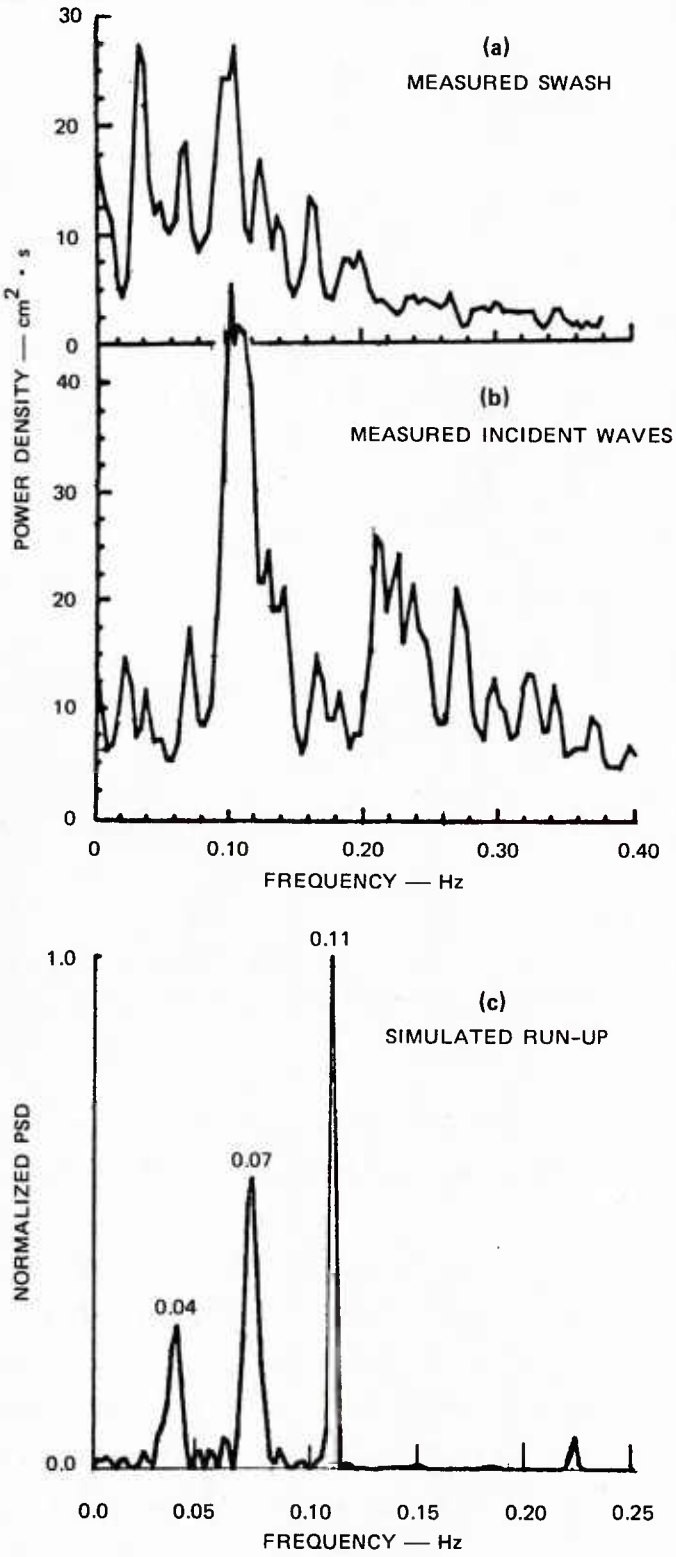

FIGURE C-4 SWASH AND INCIDENT-WAVE SPECTRA MEASURED BY SONU et al. (1974) AND THE SIMULATED RUN-UP SPECTRUM COMPUTED USING RUN-UP MODEL AND SONU'S INCIDENT-WAVE PARAMETERS

In the most recent test of the model, the Coyote Point incident-wave conditions and beach slope were used as input parameters. Figure C-5 shows (a) the Coyote Point run-up spectrum measured at transect 1 and (b) the simulated run-up spectrum computed using the run-up model and the same methods described earlier. The two incident-wave peak frequencies of 0.38 and 0.49 Hz measured from the field data were input to the run-up model. The run-up spectrum computed from the field data shows dominant spectral peaks at 0.06, 0.14, 0.25, and 0.33 Hz, and a small peak at 0.49 Hz. The simulated run-up spectrum computed by using the model (50 equivalent degrees of freedom) shows peaks at 0.12, 0.23, 0.38, and 0.50 Hz. As observed in the previous cases, the simulated run-up spectrum compares reasonably well with the measured spectrum with respect to the frequency distribution of the spectral energy. This model spectrum was computed using only the two primary frequency components from the measured incident-wave spectrum.

These simulations show that by using only the beach slope, gravitational forces, and the approximate incident-wave conditions, low-frequency energy is observed in the model-simulated run-up as it is in the field. When the hydrodynamic interaction on the beach is more fully understood, a more complete model can be developed.

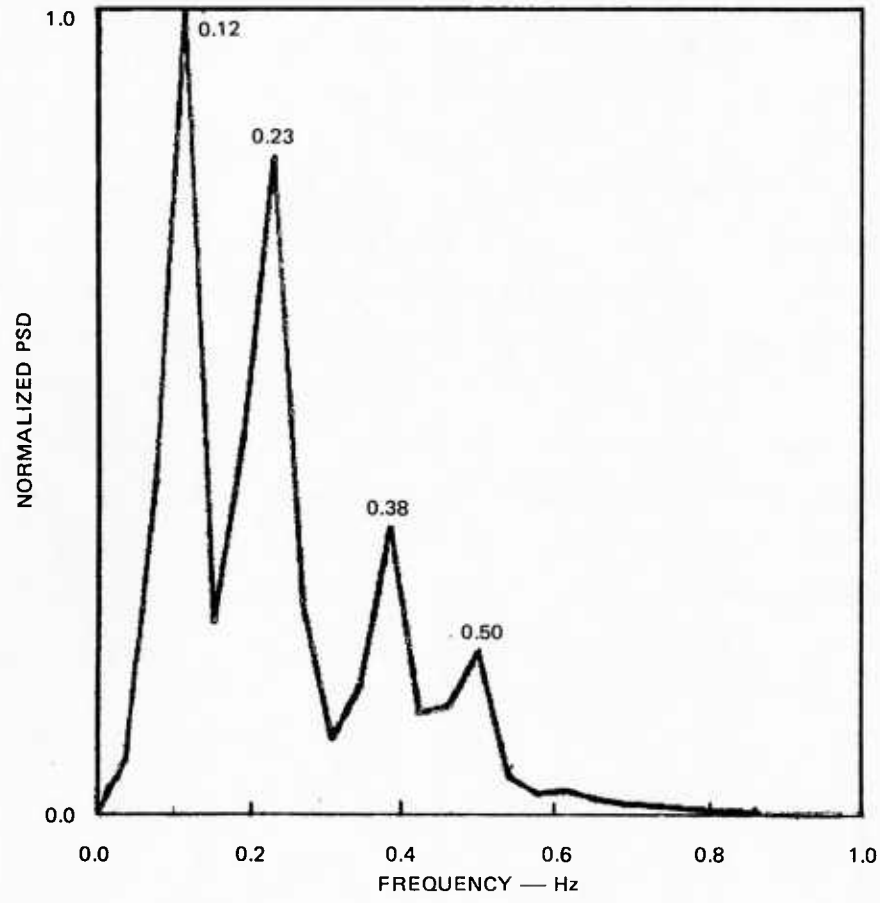

FIGURE C-5 SIMULATED RUN-UP SPECTRUM GENERATED USING RUN-UP MODEL AND APPROXIMATE COYOTE POINT INCIDENT-WAVE PARAMETERS AND BEACH SLOPE

Appendix D

REFLECTIVITY PARAMETER ϵ

The reflectivity of a beach influences the breaking characteristics of the incident waves, the degree of inshore resonance, and often the amplitude of the run-up on the beach. This observation is based on numerous laboratory, field, and theoretical studies of shoaling waves, standing waves, edge waves, and beach morphology. The reflectivity of a beach can be characterized by the reflectivity or surf scaling parameter, ε :

$$\varepsilon = \frac{a_i \omega^2}{g \tan^2 \beta} \quad , \qquad \text{(D-1)}$$

where a_i is the incident-wave amplitude near the break point, $\omega = 2\pi f$ is the incident-wave radian frequency, g is the acceleration due to gravity, and β = the beach slope. This parameter, or variations on it, have been used for some time to characterize surf zone phenomena. Patrick and Wiegel (1955) used a similar parameter to characterize different breaker types; Guza and Bowen (1975), Guza and Inman (1975), and Guza and Thornton (1982) have used it as a scaling parameter in standing wave and edge wave studies. Table D-1 shows typical delimiting values for ε and the associated characteristic phenomena. The Alameda and Coyote Point beaches showed respective ε values of 6 and 19, both clearly in the dissipative regime.

For cases in which $\varepsilon < 1$, the incident waves will be nearly completely reflected with negligible dissipation. Dissipation increases slightly for $1 < \varepsilon < 2.0\text{-}2.5$, but reflection is still quite strong. For this reflective regime, Guza and Bowen (1975) describe conditions of low dissipation, moderate resonance, and surging breakers. Generally, the ratio of the run-up height to the incident-wave height is maximized for

Table D-1

BEACH REFLECTIVITY PARAMETERIZED USING THE SCALING VARIABLE ϵ

ϵ	Reflective Condition	Characteristic Phenomena
<1	Complete reflection	Clapotis
<2 - 2.5	Strong reflection Low dissipation	Surging breakers Standing waves Edge waves Beach cusps
>2.5	High dissipation Low reflectivity	Plunging breakers Edge waves suppressed
>33	Very high dissipation	Spilling breakers

these values of ε, and wave set-up (Appendix B) is minimized. Reflective conditions favor the growth and maintenance of low-mode, resonant, synchronous ($T_{\text{edge waves}} = T_{\text{incident waves}}$) or subharmonic ($T_e = 2T_{iw}$) edge waves. Low steepness, long waves, and steep beach slopes promote low values of ε.

As values of ε increase, so does viscous dissipation of incident-wave energy. Reflectivity decreases with increasing ε, and, for $\varepsilon > 2.5$, waves cease to surge up and down the beach and begin to plunge, with an associated increase in eddy viscosity [Guza and Inman (1975)]. The plunging waves tend to suppress synchronous and subharmonic resonance, and edge waves disappear.

Most beaches do not permit total dissipation, and even under generally dissipative conditions, some minor reflection may occur. The total spectrum of amplitude oscillations in the surf zone is generally a summation of numerous progressive and standing wave components. The amplitude of the reflected component decreases with increasing ε and may become negligible for high ε values. It is possible under dissipative conditions, however, for low-frequency, infragravity edge waves (T_e = 30 - 150 s)

to appear. The effect of such edge waves on the run-up spectrum is generally detectable as a very-low-frequency modulation (f = 0.007 - 0.03 Hz).

Both the Alameda and Coyote Point beaches were low-energy dissipative systems. High-energy dissipative beaches may be fronted by wide surf zones and multiple offshore bars and breaker zones. The Alameda and Coyote Point beaches were subject only to locally generated wind waves and only one breaker zone was present, located within a few meters of the shoreline. The nearshore topography was simple for these two beaches, and since these analyses focus on the swash activity on the beach face, it was unnecessary to distinguish between inshore and nearshore values of ε.

Huntley et al. (1977) proposed a form for the run-up spectrum based on a spectral variation, $\hat{\varepsilon}$, of the surf scaling parameter ε. It is useful at this point to identify the relationship between ε and $\hat{\varepsilon}$, since the parameter $\hat{\varepsilon}$ is used in Huntley's description of saturated run-up spectra.

Carrier & Greenspan (1958) used the fully nonlinear shallow water equations to determine the maximum standing wave amplitude on an impermeable beach. They determined that a standing wave solution is possible if:

$$\varepsilon = \frac{a\omega^2}{g \tan^2\beta} \leq 1 \quad , \qquad \text{(D-2)}$$

where a is the standing wave amplitude offshore, ω is the radian wave frequency, g is the gravitational acceleration, and β is the beach slope. Munk and Wimbush (1969) obtained the same result using linear theory. Guza and Bowen (1976) made measurements of run-up for monochromatic waves on a laboratory beach of slope 0.04 to 0.12 for low values of ε. They argued that the surf zone can be represented as the sum of a standing wave and an incident progressive-wave component that decays shoreward of the breakpoint. For conditions in which the motion at the shoreline is determined primarily by the standing-wave component, then ε should approach a constant value, ε_c:

$$\varepsilon = \frac{a\omega^2}{g \tan^2\beta} = \varepsilon_c = \text{constant} \approx 1 \quad . \qquad \text{(D-3)}$$

Hence, if the incident-wave field consists of several narrow-band components, the energy spectrum of the vertical wave run-up may be represented by:

$$F(\omega)\alpha\ a^2 = \frac{\varepsilon_c g \tan^2\beta}{\omega^4} \quad , \qquad \text{(D-4)}$$

if these wave components are linearly independent at the lowest order.

Huntley presented run-up spectra measured at four natural beaches that showed an equilibrium region with an f^{-4} frequency dependence, where f is the frequency. This f^{-4} region of the spectrum was defined over the predominant incident wind-wave band of the spectrum of the incident waves. The f^{-4} saturation frequency band appeared to correspond to the frequency band of the breaking incident wind waves.

Huntley attempted to relate these observations of run-up caused by a spectrum of incident waves to the run-up produced by laboratory monochromatic incident waves. Based on the field data, they assumed a run-up energy spectrum of the form:

$$E(f) = \alpha f^{-4} \quad , \qquad \text{(D-5)}$$

and by using Eq. (D-4), they argued that:

$$\alpha = \left[\frac{\hat{\varepsilon}_c g \beta^2}{(2\pi)^2}\right]^2 \qquad \text{(D-6)}$$

where $\hat{\varepsilon}_c$ is in units/$Hz^{1/2}$. In Eq. (D-6), it is necessary to relate $\hat{\varepsilon}_c$ to the monochromatic parameter, ε .

The parameter $\hat{\varepsilon}_c$ is a spectral analog to ε. The form of the run-up spectrum suggested in Eq. (D-5) implies that the acceleration spectrum

is white (i.e., has a constant amplitude). This conclusion is obtained by computing the Fourier Transform of the second derivative of the run-up amplitude displacement time series. The form of E(f) given in Eq. (D-5) is only valid over a finite bandwidth, Δf. The magnitude of the acceleration spectrum is $(\hat{\varepsilon}_c\ g\ \beta^2)^2$, and the rms acceleration is $\hat{\varepsilon}_c\ g\ \beta^2(\Delta f)^{1/2}$. Generally, the mean square value between frequencies f_1 and f_2 is given by:

$$\psi_x^2 = 2 \int_{f_1}^{f_2} S_x(f)\, df \quad , \tag{D-7}$$

where $S_x(f)$ is the the PSD of x(t) [Otnes and Enochson (1978)]. Hence, the mean acceleration amplitude is $(2\Delta f)^{1/2}\ \hat{\varepsilon}_c g\beta^2$.

From Eq. (D-3) the critical run-up acceleration amplitude is $a\omega^2 = \hat{\varepsilon}_c g\beta^2$ and $(2\Delta f)^{1/2}\ \hat{\varepsilon}_c$ is a spectral analog of ε_c. It is interesting to note that Munk and Wimbush (1969) argued that for monochromatic waves, the downslope acceleration of the runup, $a\omega^2/\beta$, could not exceed the downslope acceleration due to gravity, g , and this suggested $\varepsilon_c = 1$. The larger values of ε_c reported by Guza and Bowen (1976) then indicate the amount by which the sinusoidal vertical run-up accelerations exceeded the Munk and Wimbush $g\beta^2$ limit. Huntley points out that in a similar fashion, $(2\Delta f)^{1/2}\varepsilon_c$ represents the factor by which the mean amplitude of the vertical acceleration in a spectrum exceeds $g\beta^2$.

Huntley indicates that $\hat{\varepsilon}_c(\Delta f)^{1/2} \cong 1$ over the frequency bandwidth of the f^{-4} run-up elevation spectrum. Huntley suggests that the run-up spectrum assumes the universal form:

$$E(f) = \left[\frac{\hat{\varepsilon} g\beta^2}{(2\pi f)^2}\right]^2 \quad , \tag{D-8}$$

where $\hat{\varepsilon}(\Delta f)^{1/2}$ is a universal constant of about 1. The parameter is a spectral analog to the more generalized surf zone scaling parameter ε. The variable $\hat{\varepsilon}$ was derived in an attempt to relate monochromatic wave run-up to the spectrum of run-up generated on a natural beach due to a spectrum of incident waves.

Appendix E

RC FILTER USED TO CONDITION THE LABORATORY ANALOG DATA

Prior to conversion of the laboratory wave and paddle motion time series data from analog to digital units, the analog time series were reviewed on an oscilloscope. The data were found to contain an unacceptable level of high-frequency electronic noise caused by the floating ground problem in the data acquisition system (Appendix A). Although later downsampling of the data would provide some degree of low-pass filtering, a simple RC filter was designed to remove this electronic noise in-line during the analog-to-digital conversion. This negated the requirement for more sophisticated digital filtering during the subsequent post-experiment data processing.

Figure E-1 shows a schematic of the four-channel RC filter designed for these data. Since the maximum incident-wave frequency was less than 2 Hz, the filter was designed with a break frequency of approximately 10 Hz, with about 35 dB of attenuation. This break frequency was selected to eliminate the undesirable higher frequencies and yet permit resolution of any second or third harmonics of the principal incident-wave frequency.

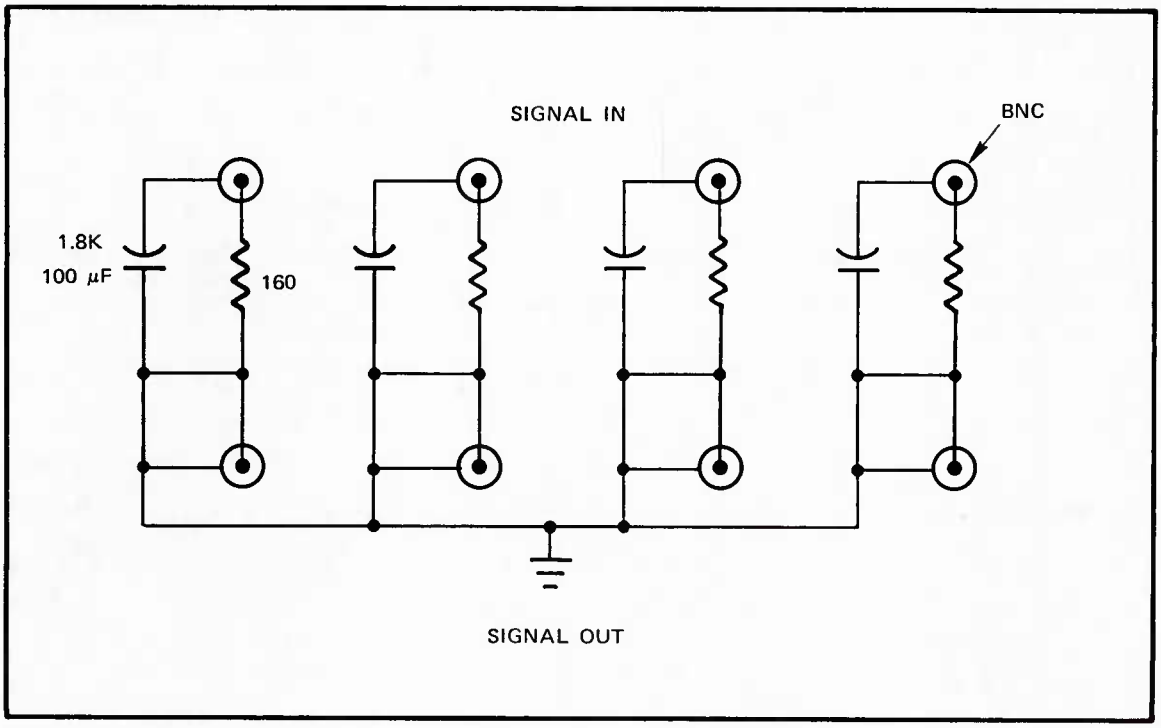

FIGURE E-1 RC FILTER USED TO CONDITION ANALOG DATA DURING ANALOG-TO-DIGITAL CONVERSION. Elements are the same for each channel.

Appendix F

ELECTRIC CLOCK FOR FIELD DATA TIME SERIES CALIBRATION

Prior experience with recording time series data photographically demonstrated the need for time calibration in the photographic record. A special battery-powered clock was built for the Coyote Point field experiment and is shown in Figure 4. The schematic for this clock is shown in Figure F-1. The circuitry is simple, and the performance of the clock was excellent. Two 9-V transistor batteries provide the power, and the user-adjustable rotation rate of the single sweep hand is held constant by the operation of the clock circuit.

The face and sweep hand are cut from sheet aluminum. The clock face is 1 ft in diameter and marked in 10 evenly spaced increments. For this experiment, the revolution rate of the sweep hand was set to 10 s/revolution, thus passing one index on the clock face every second.

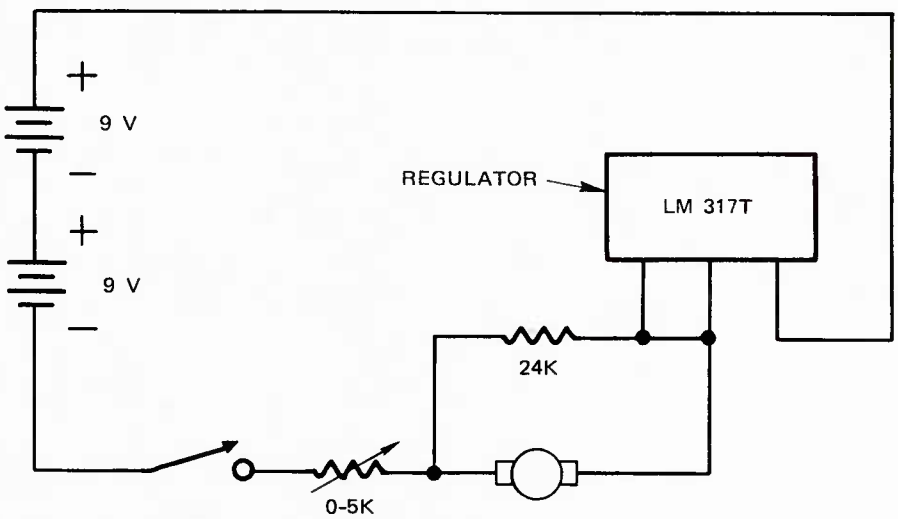

FIGURE F-1 SCHEMATIC SHOWING CIRCUITRY OF THE BATTERY-POWERED ELECTRIC CLOCK USED IN THE COYOTE POINT FIELD EXPERIMENT

Appendix G

BRIDGE WITH ISOLATION TRANSFORMER FOR RESISTANCE-TYPE WAVE PROBES

Three primary types of sensors can be used to measure wave heights in laboratory water wave modeling basins: resistance- or capacitance-type probes and subsurface pressure transducers. Resistance-type wave probes were used in the UCB laboratory experiments. Unlike the capacitance and pressure transducer wave height sensors, the resistance-type wave probe is susceptible to cross-coupling, or cross-talk, with adjacent resistance probes when intergage spacing is small. When standard Wheatstone bridges without isolation transformers were used, this electronic interference was found to be severe in the wave basin used in these experiments. Initially, a series of laboratory tests was conducted to quantify the degree of cross-talk. Existing isolation transformer bridge circuits were adapted for use with the Daytronic strain gage transducers, and further tests were conducted in the wave basin to verify that interprobe cross-talk had been reduced to acceptable levels. A schematic of the bridges used in these laboratory experiments is shown in Figure G-1. The isolation transformers allowed wave probes to be placed to within less than 1 cm from one another with no detectable interference. Using standard bridges without the transformers resulted in unacceptable levels of cross-talk between adjacent probes with separation of the order of 40 cm or less.

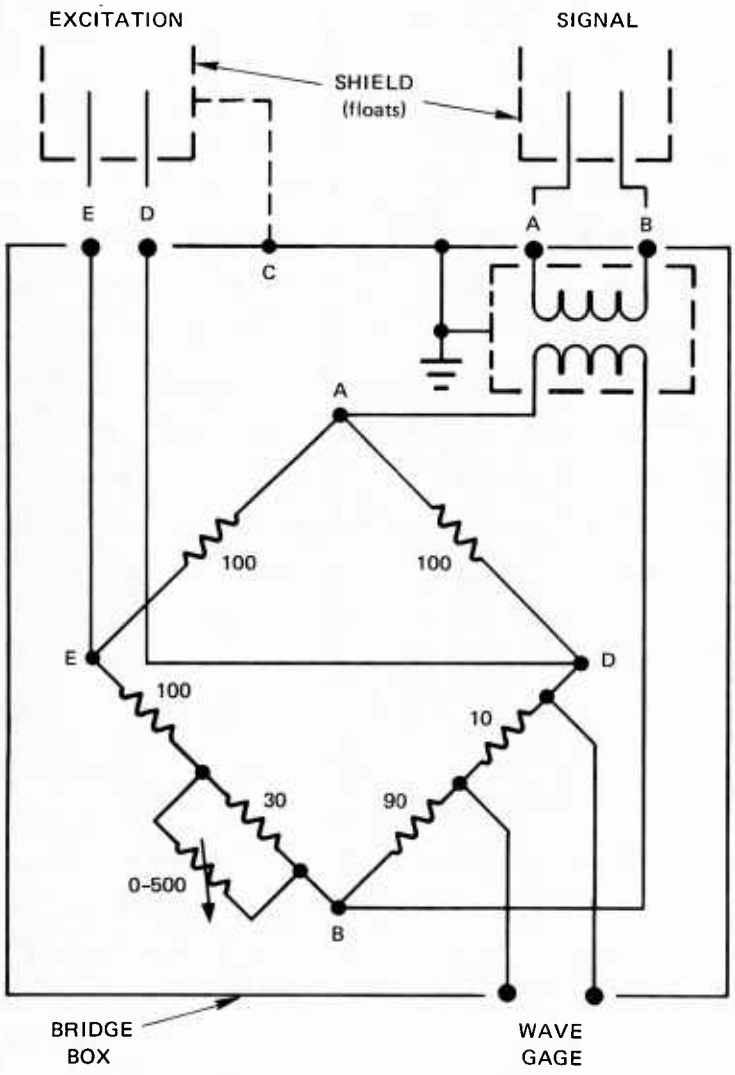

FIGURE G-1 SCHEMATIC SHOWING WHEATSTONE BRIDGE USED WITH RESISTANCE-TYPE WAVE PROBES FOR LABORATORY EXPERIMENTS. Audio transformer is a UTC No. A-18.

BIBLIOGRAPHY

Ahrens, J., "Prediction of Irregular Wave Run-Up," Coastal Engineering Technical Aid No. 77-2, U.S. Army, Coastal Engineering Res. Center, Fort Belvoir, VA, (July 1977).

American Society of Photogrammetry, Manual of Photogrammetry, 3rd Ed., Washington, DC, (1966).

Battjes, J.A., "Run-Up Distributions of Waves Breaking on Slopes," J. Waterways, Harbors and Coastal Engineering Div., ASCE, No. WW1, pp 91-114, (February 1971).

Battjes, J.A., "Computation of Set-Up, Longshore Currents, Run-Up and Overtopping Due to Wind-Generated Waves," Rept. No. 74-2, Dept. Civil Eng., Delft Univ of Tech., The Netherlands, (1974).

Bendat, J.S. and A.G. Piersol, Random Data: Analysis and Measurement Procedures, (Wiley - Interscience, New York, NY, 1971).

Benjamin, J.R. and C.A. Cornell, Probability, Statistics and Decision for Civil Engineers, (McGraw-Hill, Inc., New York, NY, 1970).

Bowen, A.J., "Rip Currents - Theoretical Investigations," J. Geophys. Res., Vol. 74, No. 23, pp 5467-5478, (1969).

Bowen, A.J. and D.L. Inman, "Rip Currents - Laboratory and Field Observations," J. Geophys. Res., Vol. 74, No. 23, pp 5479-5490, (1969).

Bowen, A.J. and D.L. Inman, "Edge Waves and Crescentic Bars," J. Geophys. Res., Vol. 76, No. 36, pp 8662-8671, (December 1971).

Bowen, A.J., D.L. Inman and V.P. Simmons, "Wave 'Set-Down' and Set-Up," J. Geophys. Res., Vol. 73, pp 2569-2577, (1968).

Bradshaw, M., "Bores and Swash on Natural Beaches," Report, Coastal Studies Unit, Dept. of Geography, Univ. of Sydney, Sydney, N.S.W. (1982).

Carrier, G.F. and H.P. Greenspan, "Water Waves of Finite Amplitude on a Sloping Beach," J. Fluid Mech., Vol. 4, Part 1, pp 97-109, (May 1958).

Carstens, T., A. Torum, A. Traetteberg, "The Stability of Rubble Mound Breakwaters Against Irregular Waves," Proc. Tenth Coastal Engineering Conf., ASCE, Tokyo, Japan, pp 958-971, (1966).

Cote, L.J., J.O. Davis, W. Marks, R.J. McGough, E. Mehr, W.J. Pierson, Jr., J.F. Ropek, G. Stephenson and R.C. Vetter, "The Directional Spectrum of a Wind-Generated Sea as Determined from Data Obtained by the Stereo Wave Observation Project," Meteorol. Papers, Vol. 2, No. 6, NYU College of Eng., New York, NY, (1960)

Emery, K.O. and J.F. Gale, "Swash and Swash Mark," Trans. American Geophys. Union, Vol. 32, No. 1, pp 31-36, (February 1951).

Freeman, J.C. and B. LeMehaute, "Wave Breakers on a Beach and Surges on a Dry Bed," J. Hydraulics Div., ASCE, No. HY2, pp 187-216, (March 1964).

Friedrichs, K.O. "Water Waves on a Shallow Sloping Beach," Comm. on Pure Appl. Math., Vol. 1, pp 109-134, (1948).

Granthem, K.N., "Wave Run-Up on Sloping Structures," Trans. American Geophys. Union, Vol. 34, No. 5, pp 720-724, (October 1953).

Guza, R.T. and A.J. Bowen, "The Resonant Instabilities of Long Waves Obliquely Incident on a Beach," J. Geophys. Res., Vol. 80, pp 4529-4534, (1975).

Guza, R.T. and A.J. Bowen, "Resonant Interactions for Waves Breaking on a Beach," Proc. Fifteenth Coastal Engineering Conf., ASCE, Honolulu, HI, pp 560-579, (July 11-17, 1976).

Guza, R.T. and D.L. Inman, "Edge Waves and Beach Cusps," J. Geophys. Res., Vol. 80, No. 21, pp 2997-3012, (1975).

Guza, R.T. and E.B. Thornton, "Wave Set-Up on a Natural Beach," J. Geophys. Res., Vol. 86, pp 4133-4137, (1981).

Guza, R.T. and E.B. Thornton, "Swash Oscillations on a Natural Beach," J. Geophys. Res., Vol. 87, No. C1, pp 483-491, (January 1982).

Hibberd, S. and D.H. Peregrine, "Surf and Run-Up on a Beach: A Uniform Bore," J. Fluid Mech., Vol. 95, Part 2, pp 323-345, (1979).

Ho, D.V. and R.E. Meyer, "Climb of a Bore on a Beach - Part 1, Uniform Beach Slope," J. Fluid Mech., Vol. 14, Part 2, pp 305-318, (1962).

Ho, D.V., R.E. Meyer and M.C. Shen, "Long Surf," J. Marine Res., Vol. 21, pp 219-232, (1963).

Hudson, R.Y., "Laboratory Investigation of Rubble-Mound Breakwaters," J. Waterways Harbors Div., ASCE, Vol. 85, No. WW3, pp 93-121, (September 1959).

Hunt, I.A., Jr., "Design of Seawalls and Breakwaters," J. Waterways and Harbors Div., Proc. ASCE, No. WW3, pp 123-152, (September 1959).

Huntley, D.A. and A.J. Bowen, "Comparison of the Hydrodynamics of Steep and Shallow Beaches," in Nearshore Sediment Dynamics and Sedimentation, J. Hails and A. Carr, eds., pp 69-109, (John Wiley & Sons, New York, NY, 1975a).

Huntley, D.A. and A.J. Bowen, "Field Observations of Edge Waves and Their Effect on Beach Material," J. Geol. Soc. Lond., Vol. 131, pp 69-81, (1975b).

Huntley, D.A., R.T. Guza, and A.J. Bowen, "A Universal Form for Shoreline Run-Up Spectra?," J. Geophys. Res., Vol. 82, No. 18, pp 2577-2581, (June 1977).

Keller, H.B., D.A. Levine and G.B. Whitham, "Motion of a Bore Over a Sloping Beach," J. Fluid Mech., Vol. 7, Part 2, pp 302-316, (February 1960).

LeMehaute, B., "On Non-Saturated Breakers and the Wave Run-Up," Proc. Eighth Coastal Engineering Conf., ASCE,, Mexico City, Mexico, pp 77-92, (November 1962).

Longuet-Higgins, M.S. and R.W. Stewart, "A Note on Wave Set-Up," J. Marine Res., Vol. 21, pp 4-10, (1963).

Longuet-Higgins, M.S. and R.W. Stewart, "Radiation Stresses in Water Waves; A Physical Discussion, with Applications," Deep Sea Res., Vol. 11, pp 529-562, (1964).

Maresca, J.W., Jr., "Bluffline Recession, Beach Change and Nearshore Change Related to Storm Passages Along Southeastern Lake Michigan," Ph.D. Dissertation, Univ. of Michigan, Ann Arbor, MI, (1975).

Maresca, J.W., Jr. and E. Seibel, "Terrestrial Photogrammetric Measurements of Breaking Waves and Longshore Currents in the Nearshore Zone," Proc. Fifteenth Coastal Engineering Conf., ASCE, Honolulu, HI, pp 681-900, (September 1976).

Pincus, H.J., "Some Applications of Terrestrial Photogrammetry to the Study of Shorelines," Photogrammetric Eng., Vol. 25, No. 3, pp 75-82, (March 1959).

Meyer, R.E. and A.D. Taylor, "Run-Up on Beaches," in Waves on Beaches and Resulting Sediment Transport, R.E. Meyer, ed., pp 357-411, (Academic Press, Inc., New York, NY, 1972).

Miller, R.L. "Experimental Determination of Run-Up of Undular and Fully Developed Bores," J. Geophys. Res., Vol. 73, No. 14, pp 4497-4510, (July 1968).

Munk, W.H. and M. Wimbush, "A Rule of Thumb for Wave Breaking Over Sloping Beaches," Oceanology, Vol. 9, pp 56-59, (1969).

Otnes, R.K. and L. Enochson, Applied Time Series Analysis, Volume 1: Basic Techniques, (Wiley-Interscience, New York, NY, 1978).

Patrick, D.A. and R.L. Wiegel, "Amphibian Tractors in the Surf," Proc. First Conf. on Ships and Waves, The Engineering Foundation Council on Wave Research and the American Society of Naval Architects and Marine Engineers, pp 397-422, (1955).

Savage, R.P., "Wave Run-Up on Roughened and Permeable Slopes," Trans. ASCE, Paper No. 3003, Vol. 124, pp 852-870, (1959).

Saville, T., Jr., "Wave Run-Up on Shore Structures," Trans. ASCE, Vol. 123, pp 139-150, (1958).

Saville, T., Jr., "An Approximation of the Wave Run-Up Frequency Distribution," Proc. Eighth Coastal Engineering Conf., ASCE, Mexico City, Mexico, pp 48-59, (November 1962).

Sawaragi, T., K. Iwata and A. Morino, "Wave Run-Up Height on Gentle Slopes," Coastal Engineering in Japan, Vol. 20, pp 83-94, (1977).

Seibel, E., C.T. Carlson and J.W. Maresca, Jr., "Lake and Shore Ice Conditions on Southeastern Lake Michigan in the Vicinity of the Donald C. Cook Nuclear Plant: Winter 1973-1974," Part XXII, Special Report No. 55, Great Lakes Res. Div., Univ. of Mich., Ann Arbor, MI, (1975).

Seibel, E., C.T. Carlson and J.W. Maresca, Jr., "The Interrelationship Between Nearshore Ice Ridges, Breaking Waves and Offshore Bars Along Southeastern Lake Michigan," International Assoc., Great Lakes Res., Vol. 2, No. 2, pp 384-392, (1976).

Shen, M.C. and R.E. Meyer, "Climb of a Bore on a Beach - Part 3, Run-Up," J. Fluid Mech., Vol. 16, Part 1, pp 113-125, (1963).

Sonu, C.J., "Tethered Balloon for Study of Coastal Dynamics," Proc. Symp. Earth Observation Balloons, pp 91-102, (1969).

Sonu, C.J., N. Pettigrew and R.G. Fredericks, "Measurement of Swash Profile and Orbital Motion on the Beach," Proc. International Symposium on Ocean Wave Measurement and Analysis, ASCE, New Orleans, LA, pp 621-638, (September 9-11, 1974).

Stafford, D.D., R.O. Bruno, and H.M. Goldstein, "An Annotated Bibliography of Aerial Remote Sensing in Coastal Engineering," MP 2-73, Coastal Engineering Res. Center, Fort Belvoir, VA, (1973).

Stoker, J.J., "Surface Waves in Water of Variable Depth," Quart. Appl. Math., Vol. 5, pp 1-54, (1947).

Suhayda, J.N., "Standing Waves on Beaches," J. Geophys. Res., Vol. 79, No. 21, pp 3065-3071, (July 1974).

Sutherland, A.J., J.N. Sharma and O.H. Shemdin, "Wave Run-Up on a Simulated Beach," Proc. Fifteenth Coastal Engineering Conf., ASCE, Honolulu, HI, pp 752-766, (July 11-17, 1976).

Thornton, E.B., "Energetics of Breaking Waves Within the Surf Zone," J. Geophys. Res., Vol. 84, No. C8, pp 4931-4938, (August 1979).

van Oorschot, J.H. and K. d'Angremond, "The Effect of Wave Energy Spectra on Wave Run-Up," Proc. Eleventh Coastal Engineering Conf., ASCE, London, England, pp 888-900, (September 1968).

Waddell, E., "Dynamics of Swash and Implication to Beach Response," Tech. Report No. 139, Coastal Studies Institute, Louisiana State Univ., Baton Rouge, LA, (1973).

Webber, N.B. and G.N. Bullock, "A Model Study of the Distribution of Run-Up of Wind-Generated Waves on Sloping Sea Walls," Proc. Eleventh Coastal Engineering Conf., ASCE, London, England, pp 870-887, (September 1968).

Welch, P.D., "The Use of Fast Fourier Transform for Estimation of Power Spectra: A Method Based on Time Averaging Over Short Modified Peridograms," IEEE Trans. Audio and Electroacoust., Vol. AU-15, pp 70-73, (June 1967).

Wiegel, R.L., Oceanographical Engineering, (Prentice-Hall International, Inc., 1964).

Wolf, P.R., Elements of Photogrammetry, (McGraw-Hill, Inc., 1974).

Wright, L.D., J. Chappell, B.G. Thom, M.P. Bradshaw and P. Cowell, "Morphodynamics of Reflective and Dissipative Beach and Inshore Systems: Southeastern Australia," Marine Geology, Vol. 32, pp 105-140, (1979).

Wright, L.D., B.G. Thom, P. Cowell, M. Bradshaw and J. Chappell, "Field Observations of Resonant Surf and Current Spectra on a Reflective Beach and Relationships to Cusps," Research Reports, Search, Vol. 8, No. 9, pp 321-322, (September 1977).

DISTRIBUTION LIST

ORGANIZATION	COPIES
DEPARTMENT OF DEFENSE	
Defense Mapping Agency ATTN: Library 6500 Brooks Lane Washington, DC 20315	1
Defense Technical Information Center Cameron Station Alexandria, VA 22314	12
DEPARTMENT OF THE NAVY	
Office of the Chief of Naval Operations ATTN: OP-952 OP-37 Pentagon Washington, DC 20350	1 1
Chief of Naval Research ATTN: Code 414L, Mr. R. Gracen Joiner Code 420 800 N. Quincy Street Arlington, VA 22217	1 1
Office of Naval Research Branch Office ATTN: Capt. M. A. Howard, USN Box 39 FPO New York, NY 09510	1
Office of Naval Research Liaison Office, Far East ATTN: Dr. Nicholas A. Bond APO San Francisco, CA 96503	1
Commander Naval Electronic Systems Command ATTN: Library National Center No. 1 Washington, DC 20360	1
Headquarters Naval Facilities Engineering Command ATTN: Library, 12S07 Hoffman Bldg. 2 200 Stovall St. Alexandria, VA 22332	1
Headquarters Naval Sea Systems Command ATTN: Library, 1S05 National Center No. 3 Arlington, VA 22202	1
Navy Department Library Bldg. 44, Naval Station Washington Navy Yard Annex Washington, DC 20003	1
Oceanographer of the Navy U.S. Naval Observatory ATTN: Library Massachusetts Ave at 34th St., N.W. Washington, DC 20007	1
Commander Naval Air Development Center ATTN: Library Warminster, PA 18974	1
Commander Naval Civil Engineering Laboratory ATTN: Library Port Hueneme, CA 93043	1
Commander Naval Ocean R&D Activity ATTN: Library NSTL Station, MS 39529	1
Commander Naval Ocean Systems Command ATTN: Library San Diego, CA 92152	1
Commander Naval Oceanographic Office ATTN: Library NSTL Station, MS 39529	1
Superintendent Naval Postgraduate School ATTN: Library Monterey, CA 93940	1
Director Naval Research Laboratory ATTN: Code 4300, Environmental Sciences Division Code 5120, Applied Ocean Acoustics Code 2600, Technical Information Division Washington, DC 20375	1 1 2
Commander David W. Taylor Ship Research & Development Center ATTN: Library Bethesda, MD 20034	1
Commander Naval Surface Weapons Center Dahlgren Laboratory ATTN: Library Dahlgren, VA 22448	1
Commander Naval Surface Weapons Center White Oak Laboratory ATTN: Library Silver Spring, MD 20910	1
Commander Naval Underwater Systems Center New London, CT 06320	1
Commander-in-Chief, Pacific ATTN: J55, Research & Analysis Division, Mr. R. F. Linsenmeyer Box 15 Camp H. M. Smith, HI 96861	1
DEPARTMENT OF THE AIR FORCE	
Headquarters Air Force Geophysics Laboratory (AFSC) ATTN: Library Hanscom AFB, MA 01731	1

DISTRIBUTION LIST

ORGANIZATION	COPIES
Headquarters Air Force Office of Scientific Research (AFSC) ATTN: Directorate of Physical & Geophysical Sciences	1
Library	1
Bolling AFB, DC 20332	
DEPARTMENT OF THE ARMY	
Office of the Chief of Engineers ATTN: DAEN-CWE	2
DAEN-RDZ-A	2
Library	1
Pulaski Building 20 Massachusetts Ave., N.W. Washington, DC 20001	
Coastal Engineering Research Center Department of the Army Ft. Belvoir, VA 22060	1
Coastal Engineering Research Center Department of the Army P.O. Box 631 Vicksburg, MS 39180	1
U.S. Army Corps of Engineers 211 Main San Francisco, CA 94105	1
U.S. Army Corps of Engineers P.O. Box 919 Charleston, SC 29402	1
U.S. Army Corps of Engineers P.O. Box 4970 Jacksonville, FL 32201	1
U.S. Army Corps of Engineers P.O. Box 889 Savannah, GA 31402	1
U.S. Army Corps of Engineers P.O. Box 1890 Wilmington, NC 28402	1
Mobility Equipment R&D Command ATTN: Marine and Bridge Laboratory Fort Belvoir, VA 22060	1
Waterways Experiment Station U.S. Army Corps of Engineers ATTN: Library P.O. Box 631 Vicksburg, MS 39180	1
OTHER	
Professor Norman H. Brooks W. M. Keck Laboratory of Hydraulics and Water Resources California Institute of Technology Pasadena, CA 91125	1
Coastal Engineering Archives 433 Weil Hall University of Florida Gainesville, FL 32611	1
Professor Kiyoshi Horikawa Coastal Engineering Laboratory University of Tokyo Bukyo-ku Tokyo, Japan	1
Director Disaster Prevention Research Institute Kyoto University Sakyo-ku Kyoto, Japan	1
Dr. Egbert Prins, Director Waterloopkundig Laboratorium Raam 61 Delft, The Netherlands	1
Mr. J. Valemboi Electricite de France Centre de Recherches et d'Essais de Chatou 6, Quai Wateir Boite Postale No. 24 78 Chatou (S.-&-O.) France	1
Engineering Societies Library 345 East 47th Street New York, NY 10017	1
Engineering Technical Reports M.I.T. Room 10-408 Cambridge, MA 02139	1
Institute of Oceanographic Sciences ATTN: D. W. Privett, Librarian Brook Road Wormley, Godalming Surrey GU8 5UB England	1
Director Scripps Institution of Oceanography La Jolla, CA 92037	1
Chairman Department of Oceanography and Meteorology Texas A&M University College Station, TX 77843	1
U.S. Geological Survey Library 345 Middlefield Road Menlo Park, CA 94025	1
Library Woods Hole Oceanographic Institution Woods Hole, MA 02543	1
Professor John B. Herbich, Head Coastal and Ocean Engineering Division Texas A&M University College Station, TX 77843	1
Sydney University Library Serials Department University of Sydney Sydney, New South Wales 2006 Australia	1
Professor Orrin H. Pilkey Department of Geology Duke University Durham, NC 27706	1

DISTRIBUTION LIST

ORGANIZATION	COPIES
Dr. Joseph W. Maresca, Jr. Vista Research, Inc. 3600 West Bayshore Rd. P.O. Box 51820 Palo Alto, CA 94303	1
Dr. Erwin Seibel Department of Geosciences San Francisco State University 1600 Holloway Ave. San Francisco, CA 94132	1
Professor Robert L. Wiegel Department of Hydraulic and Coastal Engineering 412 O'Brien Hall University of California Berkeley, CA 94720	1